Analysis and Characterization of Slab-Coupled Optical Waveguide Amplifiers and Lasers

by
William Loh

S.B., University of Michigan (2007)

Submitted to the Department of Electrical Engineering and Computer Science
in Partial Fulfillment of the Requirements for the Degree of
Master of Engineering in Electrical Engineering and Computer Science

At the

Massachusetts Institute of Technology

September 2009

Author_____
Department of Electrical Engineering and Computer Science

Certified by_____
Paul W. Juodawlkis
Assistant Group Leader, Group 83, MIT Lincoln Laboratory
Thesis Supervisor

Certified by_____
Rajeev J. Ram
Associate Director, Professor of Electrical Engineering
Thesis Co-Supervisor

Accepted by_____
Terry P. Orlando
Chairman, Department Committee on Graduate Theses

Analysis and Characterization of Slab-Coupled Optical Waveguide Amplifiers and Lasers

by

William Loh

Submitted to the
Department of Electrical Engineering and Computer Science

September 3, 2009

In Partial Fulfillment of the Requirements for the Degree of
Master of Engineering in Electrical Engineering and Computer Science

Abstract

Semiconductor optical devices are important in the photonics industry due to their significant advantages in size, weight, and power consumption (SWAP) and to their capability for photonic integration. However, these devices traditionally suffer from low fiber coupling efficiency and have been limited to relatively low power applications. This thesis explores the potential of the slab-coupled optical waveguide (SCOW) semiconductor gain medium for use in high power optical amplifiers and external cavity lasers. The thesis begins by introducing the SCOW concept and describing the benefits of utilizing a low optical confinement design for high power operation. Detailed analysis and measurements of the output power, gain, and noise properties of slab-coupled optical waveguide amplifiers (SCOWAs) and slab-coupled optical waveguide external cavity lasers (SCOWECLs) are also presented. It will be shown that these devices not only exhibit Watt class output power with high coupling efficiency (> 90 %) but also demonstrate the capability for low noise operation.

Thesis Supervisor: Dr. Paul W. Juodawlkis
Title: Assistant Group Leader Group 83
Thesis Supervisor: Rajeev J. Ram
Title: Associate Director, MIT Research Laboratory of Electronics

Acknowledgements

The completion of a thesis is truly a challenging endeavor, one that cannot possibly be accomplished without the support of many people. First, I am grateful to my advisor, Dr. Paul Juodawlkis. Thank you for your encouragement and warm support throughout the completion of this work. Your extensive knowledge on semiconductor devices and overwhelming enthusiasm in the field was truly inspirational. Through our fruitful discussions, I have learned far more in the course of two years than I would have ever hoped to learn. I am also grateful to my co-advisor, Professor Rajeev Ram. Thank you for the stimulating discussions we had during and after group meetings. Your active encouragement in student learning and your willingness to share knowledge has helped me overcome numerous challenges. Thank you to Fred O'Donnell and Jason Plant. Your help and involvement in my project was what made all of this work possible. Thank you to Jonathan Klamkin. I enjoyed and learned a lot from many of the active discussions we shared. I would also like to express my gratitude to many of the students in Rajeev's laboratory. Thank you to Jason Orcutt and Harry Lee. Your advice and support helped tremendously in guiding me through the past two years. Thank you to Kevin Lee, Reja Amatya, Parthi Santhanam, Evelyn Kapusta, and Shireen Goh. Your kindness in regarding me as a member of the group made me feel always welcome at the laboratory. Finally, I would like to express my gratitude to my loving family. Thank you to Hai-Yu Loh, Cindy Loh, and Jonathan Loh. Your encouragement throughout my life is what made all of this possible.

Content

List of Figures

List of Tables

Chapter 1

Introduction

Currently, many applications in optical communications employ fiber lasers and doped fiber amplifiers due to their many favorable characteristics for signal transmission and regeneration. Erbium doped fiber amplifiers (EDFAs), in particular, are prevalent in the C-band operation regime (1530–1570 nm) where signal transmission at 1550 nm allows for low attenuation through optical fiber. Here, EDFAs can be optimized to offer the advantages of low noise amplification [1, 2], high gain [1, 2], large saturation output powers [2, 3], and polarization insensitive amplification within the amplifier passband. However, EDFAs suffer from their intrinsically narrow gain bandwidth (~32 nm) in which they can effectively amplify signals [4]. Furthermore, doped fiber lasers and amplifiers have relatively small gain per unit length. This leads to doped fibers of very long lengths (~10-60 m for C-band EDFAs) in order to achieve significant gain. As such, fiber lasers and amplifiers typically are inefficient in terms of size, weight, and power (SWAP). Another disadvantage of these active fiber devices is their reliance on additional components for system functionality. Fiber lasers and amplifiers, for example, require the use of laser pump sources and WDM multiplexers. These extra components increase the complexity of fiber based systems.

Lasers and amplifiers based on the semiconductor gain media, on the other hand, can allow for gain-bandwidths in excess of 100 nm [5]. This allows one SOA to potentially amplify multiple signals spread across a wide distribution range. Active semiconductor devices also have the large advantages in SWAP [6] with typical devices having chip sizes of 500 X 200 X 1000 μm. This allows for compact semiconductor based lasers and amplifiers to be realized at low cost. Furthermore, semiconductor technology allows the potential of photonic integration. With photonic integration, discrete semiconductor components can be joined together to realize the functionality of an entire system on a single chip [7]. In addition to benefits in SWAP, this

allows for elimination of coupling losses, reduction in the number of packaging stages, and simplification in temperature stabilization [8].

Despite their many advantages, semiconductor devices typically exhibit poor coupling efficiency to optical fibers. This is a severe limitation as long distance communication necessitates the use of optical fibers for low attenuation optical signal transmission. In addition, fiber based amplifiers and lasers at the 1550 nm wavelength regime have typically outperformed their semiconductor based counterparts in terms of output power. Currently, fiber based modules at 1550 nm easily reach single mode output powers > 1 W [3, 9], whereas conventional semiconductor components struggle to reach output powers of >100 mW. Much of this limitation in high power 1550 nm semiconductor devices can be attributed to high intrinsic losses, high optical confinement factor (Γ), and the presence of two photon absorption in the waveguiding medium [10]. Semiconductor lasers and amplifiers also experience coupling between gain and phase characterized by the linewidth enhancement factor. The linewidth enhancement factor severely broadens the linewidth of typical semiconductor based lasers [11]. Both the concepts of two photon absorption and linewidth enhancement factor will be discussed in a later section.

In this thesis, we explore the slab-coupled optical waveguide (SCOW) gain medium [12-15] as an alternative to active fiber technology. The SCOW structure is based on a semiconductor multiple quantum well (MQW) active region that is electrically pumped. SCOW devices are designed to simultaneously achieve high fiber coupling efficiency and high power while still retaining the benefits of size and weight as well as the option of component integration. Here we describe the use of SCOW technology for high power SOAs and low-noise single-frequency lasers.

1.1 Slab-Coupled Optical Waveguide (SCOW) Overview

The Slab-Coupled Optical Waveguide (SCOW) gain medium is based on Marcatilli's analysis of slab-coupled waveguides where he noted that arbitrarily large multimode waveguides can be made to be single mode if all higher order transverse modes except the fundamental mode are coupled to a lossy slab waveguide [16]. Walpole and Donnelly first applied this concept to a semiconductor gain medium by implementing a multimode ridge waveguide structure where all

higher order modes radiate away into the slab waveguide [17]. A multiple quantum well active region is also employed to simultaneously amplify the fundamental propagating mode. The structure of the device is carefully designed so as to achieve small overlap between the optical mode and the quantum wells. This implementation allows for large ridge widths (~6 μm) and waveguide thicknesses (> 5 μm). The larger dimensions combined with the SCOW low index contrast design enables mode sizes on the order of 5.5 X 7.5 μm. Large modes are advantageous to device operation in that they allow for easy coupling to fibers. Large modes also help to distribute the device power over a larger cross sectional area, thereby decreasing the incident optical intensity. This allows for higher output powers before catastrophic optical damage is reached. In addition, the impact of optical nonlinearities such as two photon absorption (TPA) will be less severe due to the overall reduction in intensity.

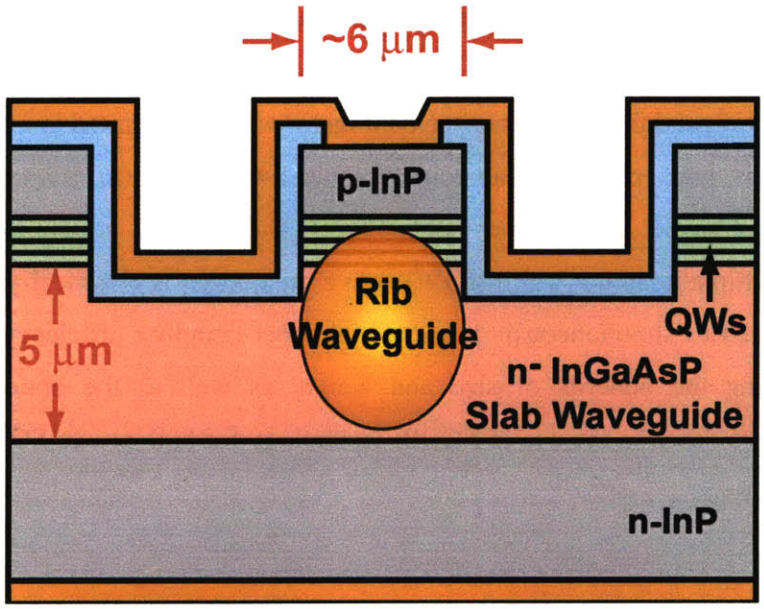

Figure 1-1: Slab-Coupled Optical Waveguide Cross Section.

The realization of low optical confinement is of central importance for obtaining higher output powers. This is true because the quantum wells saturate based on peak intensity. The SCOW gain medium is designed in order to restrict the fundamental mode within the bounds of the waveguide so that only a small fraction of the total field couples with the active region. This is

accomplished through effective tailoring of the index contrast and has the added advantage of minimizing the modal overlap with the p-InP cladding layer. As a result, high internal losses that would occur from intervalence band absorption are largely prevented in the SCOW design. Typical devices have internal losses on the order of 0.5-1 cm^{-1}. A cross section of the slab-coupled optical waveguide gain medium is shown in Fig. 1-1.

1.2 Slab-Coupled Optical Waveguide Amplifier (SCOWA)

The simplest device that uses a semiconductor gain medium is a semiconductor optical amplifier (SOA). In this section, we describe characteristics and performance metrics of semiconductor optical amplifiers with focus on the Slab-Coupled Optical Waveguide Amplifier (SCOWA). We begin by discussing the general operation of the SCOWA. Then, we quantify the gain and saturation output power performance of the device. We also discuss the SCOWA's gain-bandwidth characteristics, and we finally conclude with an analysis of its polarization dependence.

1.2.1 SCOWA Operational Principles

When an SOA is appropriately pumped, light coupled into the waveguide is amplified coherently so as to produce a higher intensity signal at the output. This coupling can be achieved by means of free space optics or with the aid of lensed fibers. However, the best fiber coupling losses reported from SOAs are usually ~3 dB [18-20], and this coupling can range to be even larger than 10 dB. The large coupling loss is due to the high mismatch between the fiber mode and the SOA mode with typical SOA mode sizes on the order of 1 μm in each dimension. In SCOWAs, however, the large optical mode size allows for highly efficient and repeatable coupling (~90%) to standard single mode fibers (SMF). The poor coupling of SOAs is particularly detrimental due to the fact that coupling loss occurs on both the input and output within a single pass of the amplifier. This severely limits the gain of the amplifier. Furthermore, coupling losses reduce the achievable signal to noise ratio and thus degrade the SOA noise figure. Therefore, the large

coupling losses that deteriorate conventional SOA performance are overcome in the slab-coupled optical waveguide design.

After the light is coupled into the input, the light propagates along the waveguide until it is coupled out. The spontaneous emission emitted by the semiconductor active medium also experiences gain, and this amplified spontaneous emission (ASE) mixes with the signal light at the output of the optical amplifier. Even though the majority of the light power is located within the passive waveguiding structure, a small fraction of the mode overlaps with the quantum well active material. It is this small fraction that experiences gain and that is responsible for amplification of the signal. The power within the mode that overlaps with the active region normalized to the total power of the mode is referred to as the transverse optical confinement factor, Γ. For typical quantum well SOAs, Γ is ~3-5% [21]. However, the SCOWA technology employs a low mode overlap design with confinement factors 0.3-0.5%. This reduction in confinement factor is critical in the SCOW design and allows for the realization of high output powers, as will be seen shortly.

1.2.2 SCOWA Gain

The small signal gain of the SCOWA is determined by the material gain, the internal losses, the confinement factor Γ, and the device length. The modal gain is given by the gain of the material (g) multiplied by Γ. The loss is taken into account by subtracting the internal loss (α_i) from the modal gain. The result,

$$\Gamma g - \alpha_i \tag{1.1}$$

is the net gain coefficient per unit length within the device. Taking into account the length of the amplifier, we find the single pass small-signal gain of the SCOWA to be

$$G_0 = e^{(\Gamma g - \alpha_i)L}. \tag{1.2}$$

The maximum gain of typical SOAs can vary significantly depending on the type of SOA (bulk, quantum-well, or quantum dot) and the specific function of the SOA. However, one can usually expect the fiber-to-fiber gain of typical semiconductor optical amplifiers to be in the 10-30 dB

range [22-24]. For comparison, the gain of a typical SCOWA is ~15 dB but can be engineered across a wide range by varying the modal overlap with the active material. The relatively low gain of a SCOWA is a result of a trade-off for high saturation output powers as we will see in the next section.

1.2.3 SCOWA Saturation Output Power

The saturation output power ($P_{out,sat}$) is defined as the SOA amplified signal power when the gain decreases to 50% of the small signal gain G_0. The gain depletes because the established population inversion decreases when a large signal is present. The population inversion condition requires the presence of excited electrons in the upper state and holes in the ground state. Each stimulated emission event consumes one electron-hole pair reducing the number of carriers available for further stimulated transitions. At higher power levels, the high rates of stimulated events begin to starve the number of available carriers. As a result, the gain of the device begins to deplete.

The saturation output power is an important parameter in SOAs for the purposes of characterizing the total achievable output power. The saturation power has the approximate analytical form of [25]

$$P_{out,sat} = \left(\frac{G_0 \ln 2}{G_0 - 2}\right)\left(\frac{wd}{\Gamma}\right)\left(\frac{h\nu}{a\tau}\right) \tag{1.3}$$

where G_0 is the small signal gain, w is the active width, d is the active thickness, Γ is the transverse confinement factor, h is Planck's constant, ν is the optical frequency, a is the differential gain, and τ is the carrier lifetime. This equation assumes negligible internal loss, which is invalid for SOAs in general. Despite this fact, we can still gain intuition into the physics behind this expression by noting that the saturation output power is inversely proportional to the confinement factor. This occurs because the quantum wells saturate due to peak intensity. If the confinement factor can be designed to be low such that most of the power is located within the waveguide, the stimulated emission rate within the quantum wells can be reduced. This helps to prevent the depletion of carriers within the active region, especially at the input side of the

device. The SCOWA amplifiers use this concept in order to optimize for high saturation output power. The disadvantage of having a low confinement factor is that the gain per unit length will be low. A long device must then be employed to achieve reasonable gain as seen from Eq. (1.2).

In the saturation output power expression, we also see that the saturation power is inversely proportional to the differential gain. This is reasonable based on the defining equation for the material gain coefficient given by

$$g = a(N - N_{tr}) \tag{1.4}$$

where N is the carrier density and N_{tr} is the transparency carrier density, and a is the differential gain. A large differential gain means that the gain changes rapidly with a change in the carrier concentration. Thus, a small depletion in the carrier concentration will cause a greater drop in the gain when the differential gain is larger.

1.2.4 SCOWA Gain Bandwidth

In addition to the gain and the saturation output power, the gain bandwidth is another important parameter characterizing an SOA. The gain bandwidth refers to the wavelength range where the small signal gain falls to half its maximum value across the gain spectrum. This parameter is important for amplifiers that are used to amplify signals across a wide distribution of wavelength ranges. To achieve a high gain bandwidth, the gain must be made flat across a large wavelength range. For semiconductor based amplifiers, this means that the density of states must be relatively constant across wavelength [25]. Because of this, quantum well and quantum dot SOAs typically demonstrate gain bandwidths in excess of 100 nm [5, 26, 27].

1.2.5 SCOWA Polarization Dependence

Polarization dependence is another figure of merit for SOAs and is used to describe the preference of the amplifier to amplify a particular polarization state of light versus another (i.e. TE or in-plane polarized as compared to TM or perpendicularly polarized). The polarization dependent gain of an SOA becomes important when the polarization state of the light that

reaches the amplifier is unknown. In these cases, a polarization insensitive amplifier must be used to guarantee sufficient amplification of the input optical signal. Typical quantum well SOAs are polarization sensitive and emit in the TE mode due to the intrinsic preferences of the light hole and heavy hole transitions toward particular polarizations. The conduction to heavy hole transition results in purely TE mode gain. The conduction to light hole transition, however, contributes $\frac{3}{4}$ to TM gain and $\frac{1}{4}$ to TE gain [28]. By straining the quantum wells, the light hole and heavy hole levels separate in opposite directions based on the type of strain applied (compressive or tensile). SCOWAs, which use compressively strained quantum wells, have almost a 20 dB gain difference in favor of the TE mode polarization. The application of tensile strain in wells can be used to compensate for the predominant TE mode gain by shifting the heavy and light hole positions until both TE and TM mode transition probabilities are balanced. However, other device properties change with strain, and it becomes an optimization problem to simultaneously achieve low polarization sensitivity while maintaining other performance metrics.

1.3 Optical Amplifier Noise Figure

In addition to the performance metrics given in section 1.2, the noise figure is a commonly used figure of merit that describes the noise performance of an optical link when an optical amplifier is introduced into the system. It is defined as the degradation in signal to noise ratio resulting from the introduction of the amplifier. In this section, we detail the derivations of the optical amplifier noise figure and discuss the implications of the obtained results.

1.3.1 Noise Figure Definition

The optical amplifier noise figure is defined by

$$NF = 10\log_{10}\left(\frac{SNR_{in}}{SNR_{out}}\right) \tag{1.5}$$

where the expression in brackets is termed the noise factor

$$Noise\ Factor = \frac{SNR_{in}}{SNR_{out}}. \tag{1.6}$$

It is important to note that the noise figure given here is defined in terms of electrical signal to noise ratios. Typically optical signal to noise ratios are not used because optical signals are always eventually received and processed electrically in a communication link. Thus, electrical noise figures become the critical targets to meet for link design.

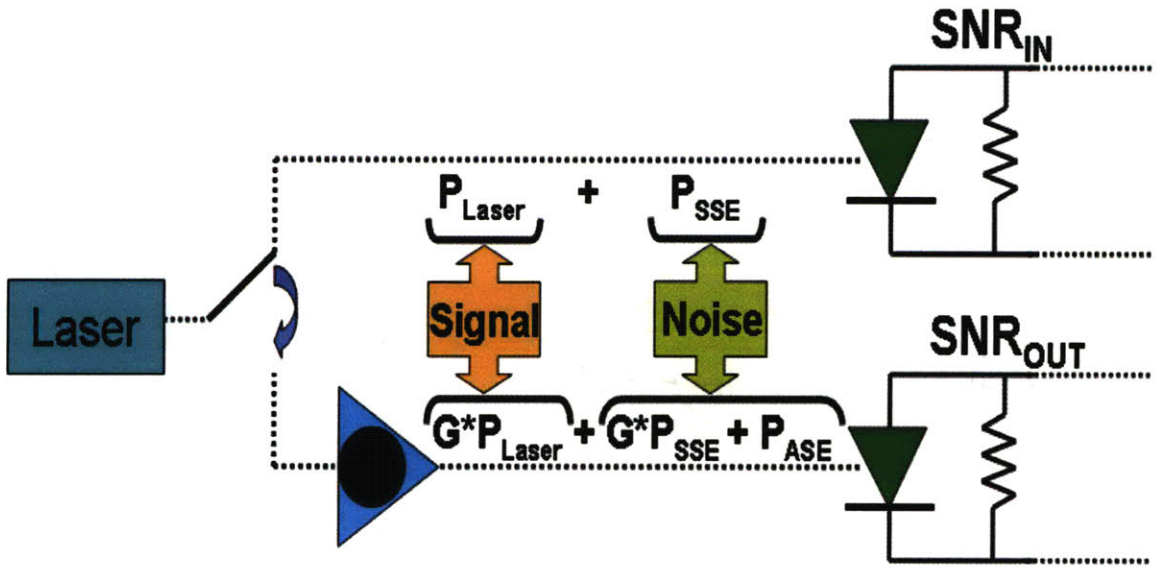

Figure 1-2: Noise Figure Schematic.

Fig. 1-2 gives a pictorial illustration of the noise figure concept. Noise figure can be understood by imagining two identical transmitter-receiver systems except with one system containing the amplifier whose noise figure is being characterized. The SNR_{in} is defined as the signal to noise ratio of the transmitted signal when the optical amplifier is not present in the system, and the SNR_{out} is defined as the signal to noise ratio measured when the amplifier is introduced. The division of these two gives the noise factor referenced to a given input noise level. In general, the noise factor will depend on the input signal to noise level. Therefore, the convention is to reference the noise figure to a shot noise limited input [29].

1.3.2 Noise Figure Theory

From the definition of the noise figure (NF) for an optical amplifier, we can now establish an expression to relate the noise figure to directly measurable quantities. The SNRs can be expressed in terms of a ratio of their corresponding signal powers and noise powers. These powers are converted to current sources through division by the load impedance.

$$SNR_{in} = \frac{\langle i_{in} \rangle^2}{\langle \Delta^2 i_{n,in} \rangle} \tag{1.7}$$

$$SNR_{out} = \frac{\langle i_{out} \rangle^2}{\langle \Delta^2 i_{n,out} \rangle} \tag{1.8}$$

Here, $\langle i_{out} \rangle^2$ and $\langle i_{in} \rangle^2$ represent the square of the average signal currents output by the photodiode when the amplifier is inserted and removed from the system respectively. Furthermore, $\langle \Delta^2 i_{n,out} \rangle$ and $\langle \Delta^2 i_{n,in} \rangle$ represent the mean square of the noise currents again measured when the amplifier is inserted and removed.

By convention, the input noise is referenced to shot noise. The shot noise spectral density is given by

$$S_{shot} = 2q\langle i_{in} \rangle . \tag{1.9}$$

We can integrate this expression over the electrical bandwidth B_e to obtain the mean square of the shot noise current. Assuming that the spectral density is constant over B_e, this becomes a simple multiplication by the electrical bandwidth, and we have

$$\langle \Delta^2 i_{n,in} \rangle = 2q\langle i_{in} \rangle B_e \tag{1.10}$$

Furthermore, we know that $\langle i_{in} \rangle$ can be related to the optical signal input on the photodiode through the responsivity $\Re$. This allows us to write

$$\langle i_{in} \rangle^2 = \Re^2 P_o^2 . \tag{1.11}$$

With these two relations, we find SNR_{in} to be

$$SNR_{in} = \frac{\Re^2 P_o^2}{2q\langle i_{in} \rangle B_e} = \frac{\Re^2 P_o^2}{2q\Re P_o B_e} = \frac{\Re P_o}{2qB_e} = \frac{\eta_d P_o}{2h\upsilon B_e} \tag{1.12}$$

where we have used Eq. (1.11) in conjunction with the definition of $\Re$

$$\Re = \frac{\eta_d q}{h\upsilon} \tag{1.13}$$

to simplify the result. Here, η_d is the photodiode quantum efficiency, q is the unit of electric charge, h is Planck's constant, and υ is the optical frequency.

SNR_{out} can be found from a similar process. The quantity $\langle i_{out} \rangle^2$ is easily related to $\langle i_{in} \rangle^2$ through the amplifier gain (G), since the amplifier output power is only a scaled version of the input power. From this, we find that

$$\langle i_{out} \rangle^2 = G^2 \langle i_{in} \rangle^2 = \Re^2 G^2 P_o^2 \tag{1.14}$$

$\langle \Delta^2 i_{n,out} \rangle$ will in general have contributions from multiple sources of intensity noise (e.g. signal-spontaneous beat noise, spontaneous-spontaneous beat noise, shot noise, pump noise, etc). For amplified signal levels, the signal-spontaneous beat noise is usually the dominant noise source. At very low power levels, however, the shot noise contribution may start to become significant. For these reasons, it is common practice to include both the signal-spontaneous beat noise and the shot noise in the expression for noise figure [29].

The signal-spontaneous beat noise current spectral density is given by

$$S_{sig-sp} = 4\Re^2 \rho_{ASE} G P_o \tag{1.15}$$

where we have implicitly assumed the signal to be $G*P_o$ and have also used ρ_{ASE} to denote the ASE power spectral density. It is important to note that ρ_{ASE} is the ASE in the same polarization state as the transmitted signal since only the light in the same polarization state can beat together

[30]. Since the $S_{sig\text{-}sp}$ takes on the shape of the spontaneous emission spectral density, which is constant over a small bandwidth B_e, we are justified in multiplying $S_{sig\text{-}sp}$ by the electrical bandwidth to obtain the mean square signal-spontaneous current noise. This results in

$$i^2_{n,sig\text{-}spon} = 4\Re^2 \rho_{ASE} G P_o B_e \tag{1.16}$$

The shot noise spectral density multiplied by the electrical bandwidth is similarly found to be

$$i^2_{n,shot} = 2qGP_o \Re B_e \tag{1.17}$$

Using these expressions, we find SNR_{out} to be

$$SNR_{out} = \frac{\Re^2 G^2 P_o^2}{4\Re^2 \rho_{ASE} G P_o B_e + 2q\Re G P_o B_e} = \frac{GP_o}{4\rho_{ASE} B_e + 2q\Re^{-1} B_e} \tag{1.18}$$

We can now evaluate the noise figure by dividing the two signal-to-noise ratios. We find that the noise factor is

$$\begin{aligned} Noise\ Factor = \frac{SNR_{in}}{SNR_{out}} &= \frac{\dfrac{\eta_d P_o}{2h\upsilon B_e}}{\dfrac{GP_o}{4\rho_{ASE} B_e + 2q\Re^{-1} B_e}} = \frac{\eta_d (4\rho_{ASE} B_e + 2q\Re^{-1} B_e)}{G(2h\upsilon B_e)} \\ &= \frac{2\eta_d \rho_{ASE} + h\upsilon}{Gh\upsilon} = \frac{2\eta_d \rho_{ASE}}{Gh\upsilon} + \frac{1}{G} \end{aligned} \tag{1.19}$$

From the equation, it is apparent that the noise figure depends on the quantum efficiency of the photodiode. A nonideal quantum efficiency that is less than unity will actually decrease the noise figure. Physically, a nonideal quantum efficiency attenuates both the shot noise and the signal-spontaneous beat noise. However, the signal-spontaneous beat noise depends on the square of η and so decreases faster than the shot noise. In the end, their ratio results in an improvement in the noise figure with increasing attenuation. A calibration is needed during testing to correct for nonideal photodiodes. Assuming the nonideal quantum efficiency correction is performed during measurement, we have

$$Noise\ Factor = \frac{2\rho_{ASE}}{Gh\upsilon} + \frac{1}{G} \tag{1.20}$$

1.3.3 Alternative Noise Figure Expression

In order to achieve an expression that can be directly related to the amplifier parameters, we begin by trying to represent the ASE spectral density in terms of the intrinsic properties of the amplifier. To do this, we first begin with the traveling wave rate equation for the photon density propagating along the z direction.

$$\frac{dN_p}{dz} = (\Gamma g(N) - \alpha)N_p + (\Gamma g(N) - \alpha)\frac{n_{sp}}{V_p} \tag{1.21}$$

where N_p is the photon density, Γ is the confinement factor, g(N) is the carrier density dependent gain, α is the internal loss, n_{sp} is the population inversion factor, and V_p is the photon volume. It is easy to verify that the solution to this equation is

$$N_p(z) = N_{p,in}e^{(\Gamma g - \alpha)z} + \frac{n_{sp}}{V_p}(e^{(\Gamma g - \alpha)z} - 1) \tag{1.22}$$

where we have used the boundary condition that $N_p(0) = N_{P,in}$. After passage through the amplifier, the photon density will be

$$N_p(L) = N_{p,in}G + \frac{n_{sp}}{V_p}(G - 1) \tag{1.23}$$

where we have used Eq. 1.2 to simplify the expression. The second term represents the ASE photon density after passage through the SOA, and we can now multiply by the photon energy, the photon volume, and the optical bandwidth to obtain the ASE power.

$$P_{ASE} = h\upsilon n_{sp}(G - 1)\Delta\upsilon_{opt} \tag{1.24}$$

The last multiplication by the optical bandwidth is a result of approximating the ASE power spectral density as white over $\Delta\upsilon > \Delta\upsilon_{opt}$. It is implicitly assumed that the ASE spectrum abruptly cuts off for frequencies outside of $\Delta\upsilon_{opt}$.

To find the power spectral density of the ASE, we now divide by the optical bandwidth and obtain

$$\rho_{ASE} = h\upsilon n_{sp}(G-1) \tag{1.25}$$

Substituting this into our expression for the noise factor, we find

$$Noise\ Factor = \frac{2h\upsilon n_{sp}(G-1)}{Gh\upsilon} + \frac{1}{G} = \frac{2n_{sp}(G-1)}{G} + \frac{1}{G}. \tag{1.26}$$

Although Eq. (1.26) appears complete, a deeper analysis reveals that the equation is missing a few corrections. For instance, the equation does not account for coupling losses. Coupling losses cause both the signal and ASE output of the amplifier to appear lower. However, because only the ASE suffers from output coupling losses while the gain suffers from coupling losses at both the input and output, it is expected that the two factors should not completely cancel. Furthermore, the equation does not account for internal loss within the amplifier. This can be shown by checking some of the boundary cases for the gain in the noise factor expression. When the gain is 1, we expect the material gain to exactly balance out the waveguide losses. From Eq. (1.26), we observe that the signal spontaneous beat noise term cancels to 0. However, intuitively, we expect that neither the ASE nor the signal level would be exactly 0 when the gain is 1. The equation for the noise factor with both corrections accounted for is given below as [31-33]

$$Noise\ Factor = \frac{1}{\eta_{in}} \frac{2n_{sp}(G_{amp}-1)}{G_{amp}} \frac{\Gamma g}{\Gamma g - \alpha} + \frac{1}{G_{amp}\eta_{in}\eta_{out}}. \tag{1.27}$$

1.3.4 Analysis of the Noise Figure Equation

From Eq. (1.27), it can be seen that the noise figure approaches a limit of 3 dB if the amplifier is fully inverted, if the coupling efficiencies are ideal, and if the gain is much higher than the loss. Physically, this limit is due to the fact that ASE is always created in the same polarization state as the gain when there is gain in the amplifier. With the maximum inversion level possible, the ratio of stimulated emission to spontaneous emission is at its maximum. However, the spontaneous emission present still mixes with the signal to produce beat noise at the receiver end of the link. The implication of this 3 dB noise figure limit is that every additional optical amplifier that is added into the system will degrade the system noise performance by at least 3 dB. In reality, the effect of each added amplifier is not as detrimental as this analysis makes it seem since the analysis assumes a shot noise limited input signal. The amplified signal will, in general, have noise contribution much higher than the shot noise limit. If this noise is large enough, the added noise from the amplifiers in the later stages will have negligible effect on the total system SNR.

Eq. (1.27) makes it clear that the SCOWA design offers many advantages in noise figure performance. The high coupling efficiencies achieved by SCOWA amplifiers allows for almost no degradation in the noise figure from input coupling. By itself, this can allow for over a > 3 dB improvement in SCOWA noise figures when compared to conventional SOAs. The SCOWA internal losses are also nearly zero. These low losses are enough to drive the factor $\frac{\Gamma g}{\Gamma g - \alpha_i}$ in Eq. (1.27) to nearly unity despite the low modal gain (due to low optical confinement) of the SCOWA. The low coupling and internal losses ensure that the signal remains at a level much higher than the noise floor.

Finally, the inversion factors achieved by SCOWA devices are nearly ideal, even at high power levels. This is true because the SCOWA gain is distributed over a 1 cm long device where the modal overlap with the quantum wells is weak. It is therefore much harder to deplete the population inversion of the quantum wells, and n_{sp} is nearly unity for SCOWA devices over a large range of operation conditions. Conventional SOAs can also achieve low inversion factors at low optical power, but n_{sp} quickly degrades once higher powers are reached.

1.4 Slab-Coupled Optical Waveguide External Cavity Laser (SCOWECL)

The slab-coupled optical waveguide external cavity laser (SCOWECL) consists of a SCOWA gain medium coupled with a frequency selective external cavity. This allows the laser to achieve resonance through feedback provided by the mirrors. A laser operates by selectively amplifying one or a small subset of the longitudinal modes within its spontaneous emission spectrum. This selection is realized by filtering out the longitudinal modes within the cavity such that only a few modes achieve net round trip gain. The filtering effect is usually achieved through the wavelength selectivity of the reflection but can also be achieved through other wavelength sensitive elements. In addition to mode filtering, mode competition processes also act to suppress the nonlasing modes of the cavity. When enough current is supplied such that the round-trip gain of the mode becomes equal to the round-trip loss, the mode reaches the lasing threshold. Any further increase in pump current then directly feeds the lasing mode and further increases the power within the mode. As a result, almost all of the laser power is distributed into a single mode or a small subset of modes, which allows for an almost purely single frequency output. The Relative Intensity Noise (RIN) and spectral linewidth are two common metrics used to evaluate the performance of a laser. We will discuss the theory and measurements of the RIN and linewidth of lasers employing the SCOW gain medium in the upcoming sections of this thesis.

1.4.1 SCOWECL Relative Intensity Noise (RIN)

The relative intensity noise (RIN) of a laser is defined as

$$RIN = \frac{(\Delta P)^2}{(\overline{P})^2} \tag{1.28}$$

where $(\Delta P)^2$ is the mean square intensity-noise spectral density of the optical signal, and $\overline{P}$ is the average optical power [34]. The RIN is a function of frequency and is a measure of the intensity noise power of the laser at the corresponding frequency. The intensity fluctuations are picked up

once the optical signal is detected by a photodiode and processed on an electrical spectrum analyzer. Generally, these fluctuations can be due to pump source noise, quantum noise, or vibrations of resonator mirrors [35, 36]. In these cases, it is the actual fluctuation of the laser output power that gives rise to the induced intensity noise.

In addition to these, intensity noise can arise as a result of the detection process. The electronic detection of a photocurrent signal from a laser results in a self-convolution of the optical spectrum. As a result, beating occurs between the various components of the optical signal. The presence of multiple modes creates beat notes at the harmonics of the mode spacing frequency. The spontaneous emission of the laser also beats with each of the lasing modes to create a noise floor across a broad range of frequencies. The spontaneous emission can even beat with itself to generate a contribution to the intensity noise resembling a downward ramp function peaked at 0 Hz. Finally, shot noise resulting from the uncertainty in photon and electron arrival as well as thermal noise due to the thermal agitation of charged carriers in conductors along the electrical signal path both present additional contributions to the RIN. The combination of all of these noise sources gives rise to the relative intensity noise spectrum.

Relaxation oscillation peaks are present in the spectra of measured laser RIN due to the resonance interaction between photons and electrons. A perturbation on the photon density in the lasing cavity causes a small deviation of the stimulated emission rate away from its steady state value. This induces a change on the population inversion of the system, which ultimately acts to counteract the perturbation on the stimulated emission rate. This cycle is characteristic of a negative feedback system and results in stable oscillations back to steady state operation under the presence of small fluctuations. The relaxation oscillations occur at a characteristic frequency, which results in a peak in the relative intensity noise spectrum. For typical semiconductor lasers, the RIN peak is in the range of 1-10 GHz and is often at least several GHz wide. However, it will be shown later that the RIN peak of a SCOWECL is beneath the noise level for measurable values of the shot noise floor. This relaxation resonance suppression is one of the many advantages of employing a SCOW based laser design.

From the Eq. (1.28), we see that laser RIN is expected to be closely related to amplifier noise figure since both expressions can be interpreted in terms of signal-to-noise ratios. Therefore, we expect the SCOW gain medium characteristics that contribute to a low noise figure amplifier to also contribute to a low RIN laser. This is seen through the population

inversion factor, where it was previously mentioned that SCOW amplifiers are expected to have low n_{sp} at high powers due to its high resilience to gain depletion. Since n_{sp} is related to ASE noise, this allows for low RIN SCOWECL lasers at output powers approaching 1 W. Furthermore, the low internal losses of the SCOW gain medium also indirectly benefit the laser's relative intensity noise. Low internal losses allow the threshold condition to be achieved at lower current densities. This then yields a higher output signal and a correspondingly higher SNR for the same bias point. Note that this analysis assumes the noise power to be signal independent, which is generally not true for beat noise. To estimate RIN for signal dependent noise powers, the increase of the signal level must be compared against the relative increase of the noise.

1.4.2 SCOWECL Linewidth

In contrast to RIN, the linewidth of a laser is due to phase noise rather than intensity fluctuations. The laser linewidth is given by the full width at half maximum of the electric field power spectral density. The quantum-limited linewidth arises due to the random phase acquired by photons generated through spontaneous emission events. The spontaneously emitted photons mix in with the optical field, and the mismatch in phase decreases the established coherence. A change in the phase causes a shift in the instantaneous frequency, which results in a finite lasing linewidth.

Fig. 1-3 illustrates the rotation in phase of the optical field due to the addition of a spontaneously emitted photon. The optical field has a collective ampltiude $\sqrt{I}$ and phase Φ and is denoted by the phasor $\sqrt{I}e^{j\Phi}$. Here, I is the intensity of the optical field. The spontaneous photon has amplitude 1 with phase θ_i and can be similarly written as $e^{j(\Phi+\theta_i)}$. After the photon is added to the system, the combined field has amplitude $\sqrt{I+\Delta I}$ and is rotated from its previous phase by $\Delta\Phi$. It is easy to show that the phase change is given by

$$\Delta\Phi = \frac{1}{\sqrt{I}}\sin(\theta_i) \tag{1.29}$$

for small changes in $\Delta\Phi$.

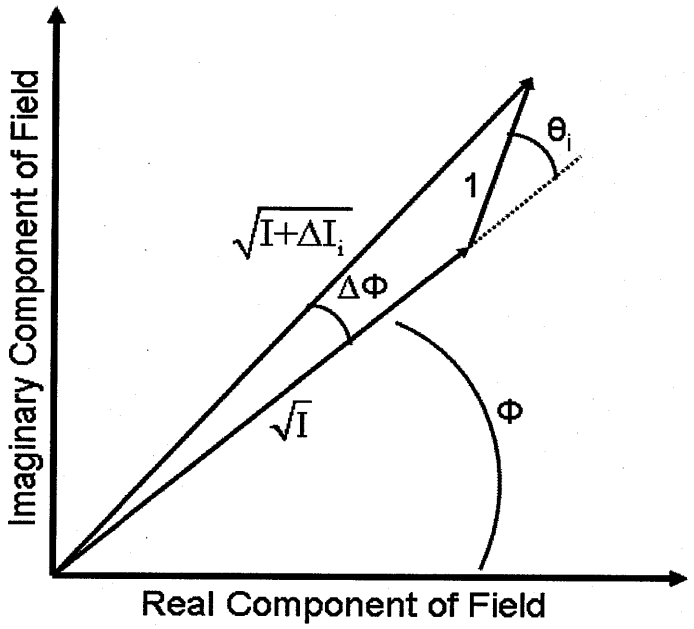

Figure 1-3: Phase change of optical field resulting from a spontaneous emission event.

When a spontaneous emission event occurs, the laser undergoes relaxation oscillations to try to restore steady state operation. Through this process, the carrier density will shift to establish equilibrium. As seen by Eq. (1.4), carrier density fluctuations cause gain fluctuations, which are then coupled to refractive index fluctuations through the Kramer's Kronig relations. It can be shown that the phase change associated with this process is given by

$$\Delta\Phi' = -\frac{\alpha_H}{2I} - \frac{\alpha_H}{\sqrt{I}}\cos(\theta_i) \tag{1.30}$$

where α_H is the linewidth enhancement factor defined as [11]

$$\alpha_H = \frac{dn/dN}{dg/dN}. \tag{1.31}$$

Here, N is the carrier density, n is the refractive index, and g is the gain. The laser linewidth is related to the total phase change, and the result can be derived to be

$$\Delta\upsilon = \frac{R_{sp}}{4\pi I}\left(1+\alpha_H{}^2\right). \tag{1.32}$$

Finally, writing this expression in terms of the intrinsic parameters of an external cavity laser comprising both active and passive cavity sections [37]

$$\Delta\upsilon = \frac{\left(\Gamma v_g g_{th}\right)^2 \eta_0}{4\pi P_0} n_{sp} h\upsilon \left(1+\alpha_H{}^2\right)\left(\frac{n_{ga}L_a}{n_{ga}L_a + n_{gp}L_p}\right)^2 \tag{1.33}$$

where v_g is the group velocity in the active region, Γ is the confinement factor, g_{th} is the threshold gain, P_0 is the single-facet power, η_0 is the single-facet efficiency, n_{sp} is the population inversion factor, n_{ga} is the active material group index, n_{gp} is the passive material group index, L_a is the active cavity length, and L_p is the passive cavity length.

From this expression, we see again that the SCOW gain medium offers significant benefits compared to conventional lasers in regards to obtaining a narrow linewidth. The threshold gains of the SCOWECL devices are much lower than in conventional lasers because the internal losses are much smaller. From Eq. (1.33), we see that the corresponding linewidth should also be lower. In addition, the SCOW medium allows for much higher powers before saturation is reached. Again, this is seen to produce a corresponding reduction in the linewidth. Finally, the near ideal population inversion factor exhibited by the SCOW gain medium is also favorable for obtaining a narrow linewidth as observed in Eq. (1.33). A more physical argument for the narrower laser linewidth of SCOWECLs can be formulated in terms of the laser cavity's quality (Q) factor. The Q factor is defined as

$$Q = \frac{\nu_0}{\Delta\upsilon} = 2\pi \frac{\text{Energy Stored}}{\text{Energy Dissipated}}. \tag{1.34}$$

Here, ν_0 is the lasing frequency and $\Delta\upsilon$ is the linewidth. We see that with more energy dissipated in the losses of the cavity, the cavity Q decreases and the linewidth increases.

1.5 Slab-Coupled Optical Waveguide Device Applications

In sections 1.3-1.4, we have shown that the unique properties of the SCOW gain medium are favorable and directly applicable to the realization of high-power low-noise semiconductor optical amplifiers and lasers. In the upcoming sections, emphasis will now be placed on system

level applications for SCOW-based devices. We first detail the application space for SCOWA amplifiers by comparing SCOWA amplifiers to the current state of the art technology. We then examine the uses of SCOWL and SCOWECL lasers focusing on systems whose functionality can significantly benefit from high power lasers. Finally, we introduce the Slab-Coupled Optical Waveguide Photodiode (SCOW-PD) concept and describe the applications where it can be utilized.

1.5.1 Slab-Coupled Optical Waveguide Amplifier Applications

Optical amplifiers are used in optical communication systems where the signal level must be amplified in order to preserve the SNR or to keep the signal within detection limits. From a systems perspective, optical amplifiers are classified into three different categories: booster amplifiers, in-line amplifiers, and pre-amplifiers. Booster amplifiers are used to directly amplify the output of an optical source in order to boost signal levels prior to transmission. Because the laser polarization state is known, the optical amplifier can be polarization dependent as long as the polarization state of maximum gain is in the same state as that of the laser signal. Booster amplifiers require high saturation output powers in order to transmit as large of a signal as possible. The gain and noise figure requirements are less stringent as the signal emitted by the laser source will likely already be high. However, a high-gain low-noise figure booster amplifier is still useful. Since noise figure and RIN are both directly related to spontaneous emission noise, a low noise figure amplifier can be directed integrated with a low RIN laser in the same material system for photonic system applications.

The SCOWA device exemplifies all characteristics needed for a booster amplifier. Its ultra-high saturation output power, high coupling efficiency, and low noise figure make it ideal for amplifying the power of transmitted signals. This is especially apparent in wavelength division multiplexing (WDM) applications where the SCOWA's high saturation output powers are expected to suppress crosstalk between channels. A high coupling efficiency is also important for efficient power transfer between the SCOWA and optical fiber. The amplifier's low noise figure provides the added benefit of low noise amplification. Traditionally, low noise figures are critical only in-line and pre-amplifier applications but not for booster amplifier applications where the signal levels are high. However, because of the common properties shared

between noise figure, relative intensity noise, and linewidth, the same material used to fabricate a low noise amplifier can also be used in designing low noise lasers. In integrated laser-amplifier applications, low noise, high power, narrow linewidth systems can be realized. In addition, if the SCOWA can be designed to be polarization insensitive, options for in-line amplifier operation become available. In these amplifiers, the noise figure is critically important. Finally, because the gain bandwidth of a SCOWA is > 100 nm, one SCOWA amplifier can potentially amplify a large number of input channels. This is in direct contrast to EDFAs which have a gain bandwidth of ~35 nm.

Inline amplifiers are used for signal regeneration in order to counteract propagation losses that attenuate the signal. These amplifiers require high gain and low noise figure since the signal levels will be low due to losses. Polarization insensitivity is essential as the conventional telecomm fibers do not preserve polarization. Thus, inline amplifiers need to be able to amplify all polarizations equally as the signal polarization upon reaching the amplifier is unknown. High saturation output power is useful in these amplifiers in order to drive the signal level higher upon exit. Currently, due to the polarization sensitivity of the SCOWAs, they cannot be used as inline amplifiers. However, through proper design, it is conceivable that a polarization insensitive SCOWA can be demonstrated.

Pre-amplifiers are used to boost the signal prior to detection in order to increase the sensitivity of the receiving detector. Similar to inline amplifiers, pre-amplifiers are required to be polarization insensitive. Furthermore, these amplifiers need high gain and low noise figure in order to compensate for low signal levels at the input. High saturation output powers, however, are not important as receivers typically do not handle high power levels. SCOWA amplifiers are unsuitable to serve as pre-amplifiers since they are intrinsically polarization sensitive and have noise figures which are still too noisy for pre-amplifier applications. Furthermore, many of the advantages of using a SCOWA (high output power) are only of secondary concern in pre-amplifiers. Thus, even if a polarization insensitive SCOWA could be fabricated, it will likely not find usage as a pre-amplifier.

1.5.2 Slab-Coupled Optical Waveguide Laser Applications

High power lasers find use in many applications where attenuation would otherwise cause a signal to fall below an acceptable minimum. Typical low-noise semiconductor lasers output a few mW of power and require external amplification to reach signal levels practical for most applications. This amplification process introduces noise and reduces system efficiency, so it is desirable to bypass the amplifier by using a higher power source. One application for high power mode locked lasers is in photonic analog-to-digital converters where they are utilized to sample a microwave input signal. The sampling process is performed using a modulator with the laser pulses as the input and the microwave signal as the driver for the modulator. Here, high powers compensate for losses encountered during signal propagation such that detection sensitivity is high when the modulated optical signal is eventually detected. SCOWLs are excellent candidates as mode locked laser sources as a colliding pulse mode locked SCOWL has been recently demonstrated exhibiting 8.54 GHz repetition rate, < 20 ps detector limited pulse duration, and 170 mW average output power out of each facet [38].

In addition to mode locked SCOWLs, external-cavity laser configurations using the SCOW gain medium have also been realized. These external-cavity lasers use a fiber Bragg grating as the wavelength selective element to achieve narrow linewidth, high power, and low RIN performance in a single frequency source. The measurements of these slab-coupled optical waveguide external-cavity lasers (SCOWECLs) will be detailed in Chapter 3. The measured SCOWECL characteristics make them excellent sources for analog photonic links. In an analog photonic link, data that is picked up by a remote receiver antenna is relayed back to the central office via a fiber-optic network. This is accomplished remotely by modulation of the received information onto a laser signal sent from the central office. Because the noise properties of an optical link are largely influenced by the properties of the laser, the laser must meet strict standards in order to achieve optimum link performance. In particular, an ideal optical link laser will have high output power, low RIN, and narrow linewidth. Narrow linewidth, in particular, is essential for phase-modulated laser signals as the phase noise of the laser must be very low to allow for accurate signal demodulation. The SCOWECL is ideal for this application as it is expected to perform exceptionally in all three of these metrics based on our earlier discussion.

1.5.3 Slab-Coupled Optical Waveguide Photodiode Applications

Although our primary focus in this thesis will be on the SCOWA and SCOWECL devices, it is nevertheless useful to mention other devices that have been fabricated using the SCOW device concept. One example of such a device is the slab-coupled optical waveguide photodiode (SCOW-PD). Conventional photodiodes saturate very easily as most of the light is absorbed over a relatively small area. The photo-generated carriers screen the electric field applied, which eventually leads to saturation when the applied field over the absorption layer becomes negated. The SCOW-PD attempts to raise this saturation current by distributing the light absorption across a large area. The light absorption per unit length is reduced by weakening the overlap of the optical mode with the absorbing material. By distributing the absorption of light along the 1 cm device length, the SCOW-PD prevents an accumulation of carriers at any given point. This results in a reduction in field screening and an overall reduction in the effects of saturation. A traveling-wave geometry is employed to increase the 3 dB bandwidth of the photodiode. A SCOW-PD has been recently demonstrated with 300 mA saturation current and 1 GHz bandwidth. This photodiode can be utilized in transmit links where a high power photodiode is needed to convert an RF signal into a large photocurrent to drive a transmit antenna.

1.6 Thesis Overview

This thesis focuses on the application of the novel slab-coupled optical waveguide gain medium to semiconductor active devices. This design allows for high output powers to be achieved while simultaneously maintaining low-intensity-noise operation. Such characteristics are favorable for semiconductor-based optical amplifiers and lasers for high-power and high signal-to-noise ratio transmission at the 1550-nm telecommunications wavelength.

The organization of the rest of the thesis is as follows. Chapter 2 describes gain and noise figure measurements performed on a packaged SCOWA Chapter 3 details the design and characterization of an external cavity laser employing a SCOW gain medium (SCOWECL) coupled to a fiber passive cavity. Chapter 4 presents the conclusions and future work for the research presented in this thesis.

Chapter 2

Slab-Coupled Optical Waveguide Amplifier Characterization

Considerable research is being performed on semiconductor optical amplifiers today due to their small size, low weight, high power efficiency, and their potential for photonic integration. Among them, the Slab-Coupled Optical Waveguide Amplifiers (SCOWAs) show much promise as they exhibit excellent performance characteristics under high power levels with low coupling and internal losses. In this chapter, we present the experimental setup and characteristics of SCOWAs. The current-voltage (IV) of the SCOWAs are analyzed, and their turn-on voltage and series resistances are extrapolated. Gain saturation results are presented in order to demonstrate the output power capabilities of SCOWA devices. From the I-V and gain saturation data, the efficiencies of these amplifiers can then be estimated. In general, the efficiency is a function of both the bias current and input signal operating regime. These measurements were all performed on a packaged SCOWA device demonstrating a world record saturation output power of 29 dBm [14]. A discussion of the results follows the presentation of the measurement data.

An important figure of merit describing the noise performance of optical amplifiers is the noise figure. The theoretical framework for noise figure has been previously developed in Chapter 1. Here, we present the theory for the optical and electrical methods for measuring noise figure. In addition, we present noise figure measurement results of the packaged SCOWA using both methods and compare their agreement across multiple current and wavelength ranges. Because several parameters need to be measured precisely to interpret noise figure data, special emphasis is placed on the correct calibration of the setup for both optical and electrical

measurement techniques. Using the results, we can predict the population inversion factor of the device across the current and wavelength ranges used in our measurements. We employ a theoretical model of the population inversion factor as a basis for comparison of the results. Our measured results will show the advantages of the SCOWA over conventional semiconductor based approaches to optical amplification.

2.1 Packaged SCOWA Device Measurements

In this section, we detail our testing of a packaged SCOWA device. The semiconductor device is 1 cm long and mounted p-junction down on a Cu-W submount. The SCOWA is angled at 5° and AR coated to prevent reflections at the facets. Lensed fibers are used to couple light into and out of the packaged device. We will discuss measurements of the SCOWA I-V characteristics, gain saturation, electrical-to-optical conversion efficiency, gain spectra, and polarization sensitivity in the following sections [39].

2.1.1 Current-Voltage Characteristics

We measured the I-V characteristics of a packaged slab-coupled optical waveguide amplifier using the 4-point probe technique. The amplifier was cooled to 16° C with a thermoelectric cooler (TEC) and was not seeded by any input signal. The current source used was a Keithley 2440. The 4-point probe was employed in order to bypass the voltage drop in the wires of the probe leads when the voltage is measured. In this method, two of the probes are used to bias the device. The remaining two probes are positioned close to the device contacts, and the voltage is measured without passing significant current. The results of the measured I-V characteristics are shown in Fig. 2-1.

In a diode, the diode resistance decreases as the forward bias increases across its contacts. Thus, a linear fit to the I-V curve at high bias currents measures the series resistance of the diode assuming the diode resistance is negligible. Furthermore, the extrapolation of the linear fit to zero current gives the effective turn on voltage for the diode. From the measured data, we find the series resistance to be 0.08737 Ω and the turn on voltage to be 0.8912 V. The series

resistance includes the resistance from the contacts of the device. A low series resistance is important for high efficiency operation as will be discussed shortly.

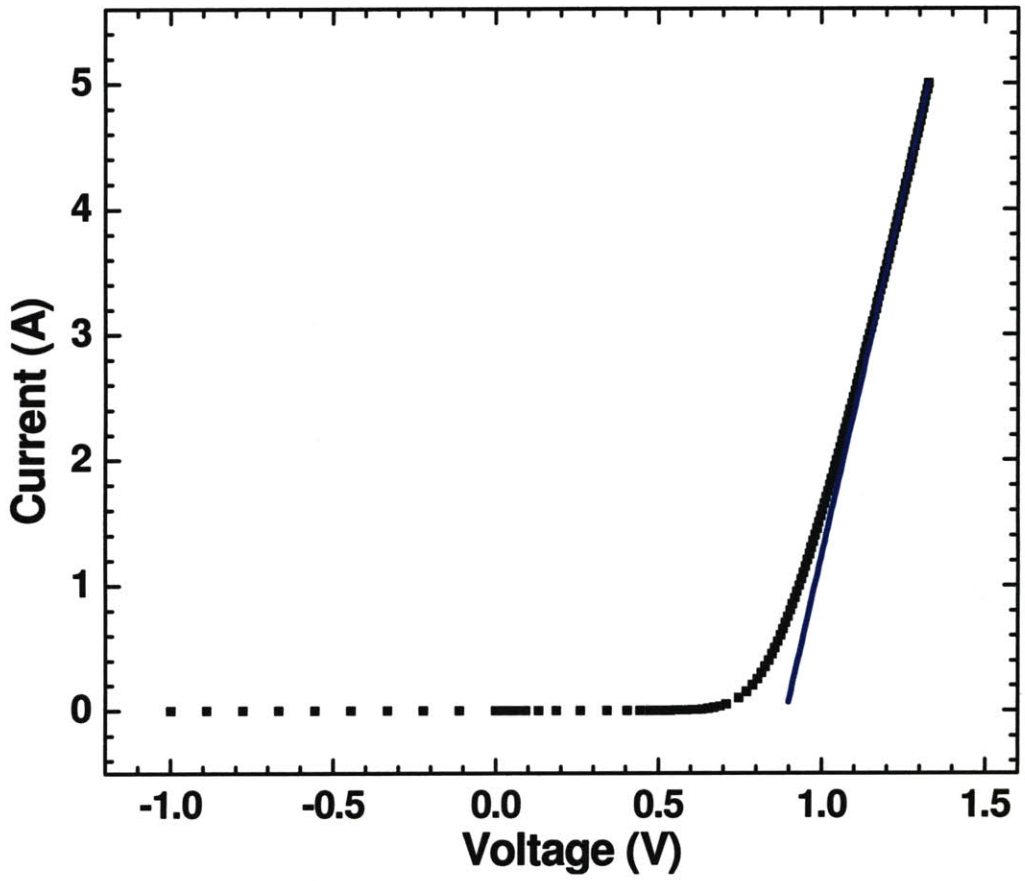

Figure 2-1: Packaged SCOWA current versus voltage showing measured characteristics (solid squares) and best fit line (solid line). Operating conditions: λ = 1550 nm, T = 16 °. Best fit line: V = 0.08737*I + 0.8912 (V).

2.1.2 SCOWA Gain Spectra

The SCOWA gain as a function of the wavelength describes the potential of the SOA for amplifying signals across a range of wavelengths. In our measurements, we have also characterized the gain spectra as a function of current, thus allowing us to measure the small signal gain and gain-bandwidth as the bias is varied. The setup used for measuring the gain

spectra characteristics is shown in Fig. 2-2. The components used are a tunable laser source, a

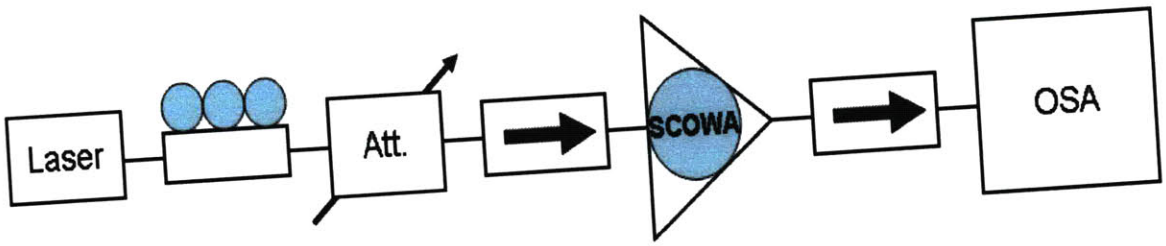

Figure 2-2: Gain Spectra measurement setup for SCOWA

polarization controller, a variable attenuator, two optical isolators, the SCOWA device, and an optical spectrum analyzer. The gain spectra were measured by sending the output of a tunable laser source into the SCOWA and measuring the amplified signal on an OSA. Afterwards, the amplifier is taken out of the system, and a similar measurement is made. A comparison of the measurements with and without the amplifier present yields the gain of the SCOWA.

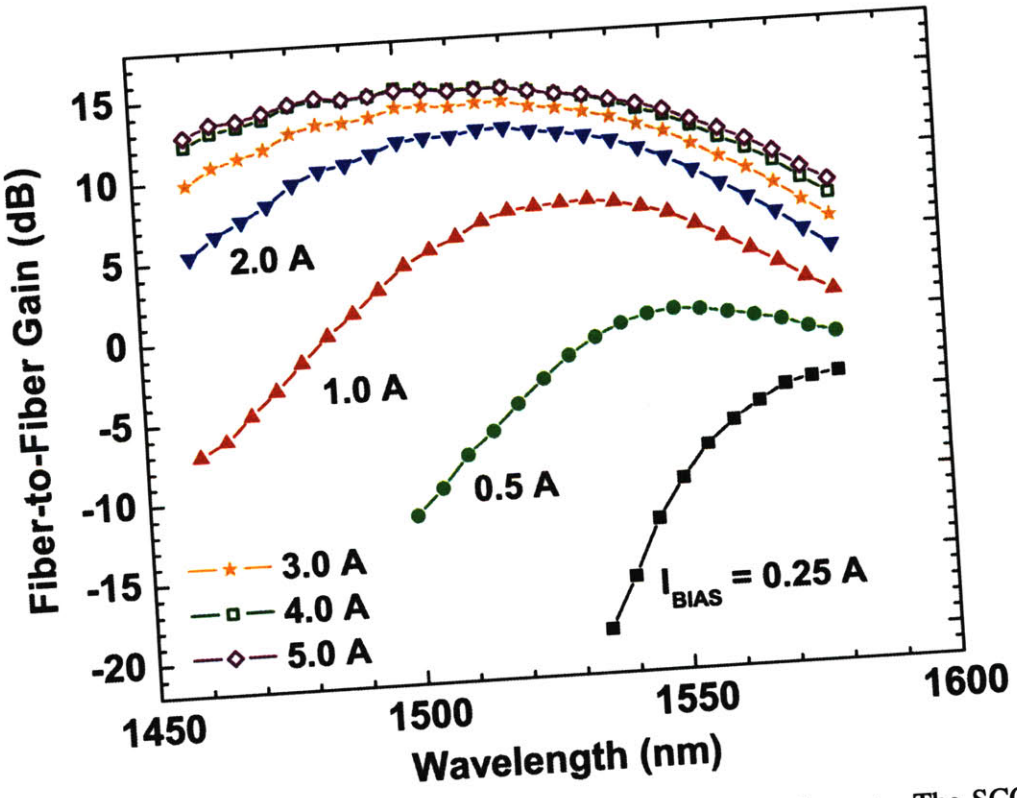

Figure 2-3: Packaged SCOWA Gain Spectrum for Various Bias Currents. The SCOWA was operated at T = 16 °C.

Fig. 2-3 shows the results of the gain spectra measurement. From the results, we see that the gain peak shifts toward shorter wavelengths with increasing bias due to the band-filling effect [40, 41]. We also see that both the small signal gain and gain-bandwidth increase as bias current is increased as expected. At 5 A operating current, the peak gain of the device is ~ 15 dB, and the gain-bandwidth is greater than 100 nm (<1460 nm to 1560 nm). Here the tuning range on the short wavelength side of the tunable wavelength source limits us from obtaining a more accurate estimate of the bandwidth. The gain spectra measurement of the packaged SCOWA will be important for characterizing the noise figure of the amplifier, as will be discussed in the following sections.

2.1.3 SCOWA Gain Saturation Measurement

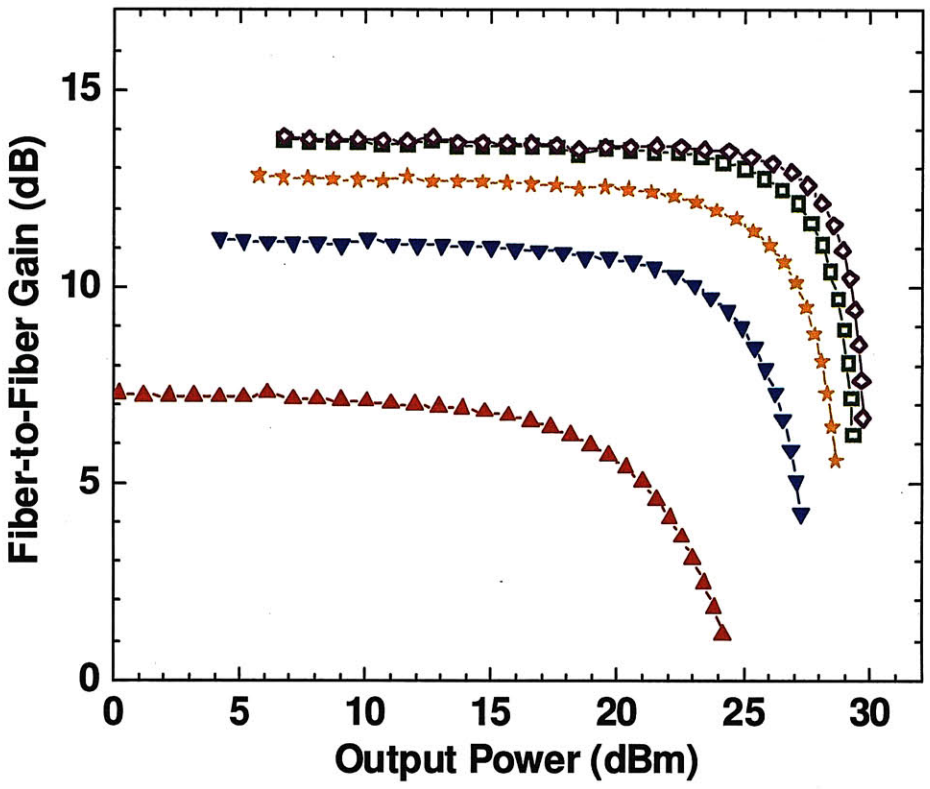

Figure 2-4: Packaged SCOWA Gain Saturation at 1 A (upright triangles), 2 A (inverted triangles), 3 A (stars), 4 A (open squares), and 5 A (open diamonds) bias currents. The SCOWA was operated at λ = 1540 nm, T = 16 °C.

The gain saturation characteristic of an optical amplifier can be measured by varying the power of an input laser signal and simultaneously measuring the output of the amplifier. The laser used was an Agilent tunable laser model 8164A, and the output was measured with an ILX power meter. To determine the gain of the amplifier, we divide the output power by the laser input power. Because the stimulated emission eventually begins to deplete the electron-hole population available for recombination, the gain saturates as the input laser power grows. Thus, the gain will eventually decrease as the input power is increased. The gain saturation measurement at $\lambda = 1540$ nm for the packaged SCOWA was performed by Jason Plant and the results are illustrated in Fig. 2-4 as a function of bias current [39].

From Fig. 2-4, we see that the packaged SCOWA exhibits a 29 dBm saturation output power at 13.8 dB small signal gain when biased at 5 A current levels. Also, based on the figure, we can note some general trends. First, we see that the gain increases with current bias since the population inversion increases as the device is driven harder. We furthermore find that the saturation power increases as the bias current is increased. This is expected since the differential gain of the amplifier decreases with increasing bias. This result from the upper state becoming populated enough so that the inversion level becomes nearly resilient to carrier density changes. Finally, we see that the change in gain decreases as bias current increases. Effectively, this means the differential gain decreases towards higher current levels, which is advantageous for higher saturation output power for the reasons mentioned in Chapter 1.

2.1.4 SCOWA Electrical-to-Optical Conversion Efficiency

The electrical-to-optical conversion efficiency ($\eta_{E\text{-}O}$) of a semiconductor optical amplifier refers to the optical power supplied by the amplifier divided by the total input electrical power supplied to the amplifier. It is a measure of how much of the input electrical power is wasted when amplifying an optical signal. Traditionally, few sources cite the electrical-to-optical efficiency of SOAs [42] because semiconductor amplifiers typically are low power devices. That is, they usually have low saturation output power, so they are not pumped to a high degree. In these cases, the wasted electrical power is not critical since it is still only a small fraction of the total

system power budget. For example, typical commercial Alphion SOAs at 1550 nm require an input electrical power of 600 mW to reach an efficiency ~3% at the 3dB saturation point [43].

However, for high power amplifiers (e.g. SCOWAs), the electrical input power required can no longer be ignored. The SCOWA's input electrical power at 5 A is 6.64 W, which is over an order of magnitude larger when compared to conventional SOAs. Fig. 2-5 plots the electrical-to-optical efficiency of the packaged SCOWA as a function of both the input optical power and current bias.

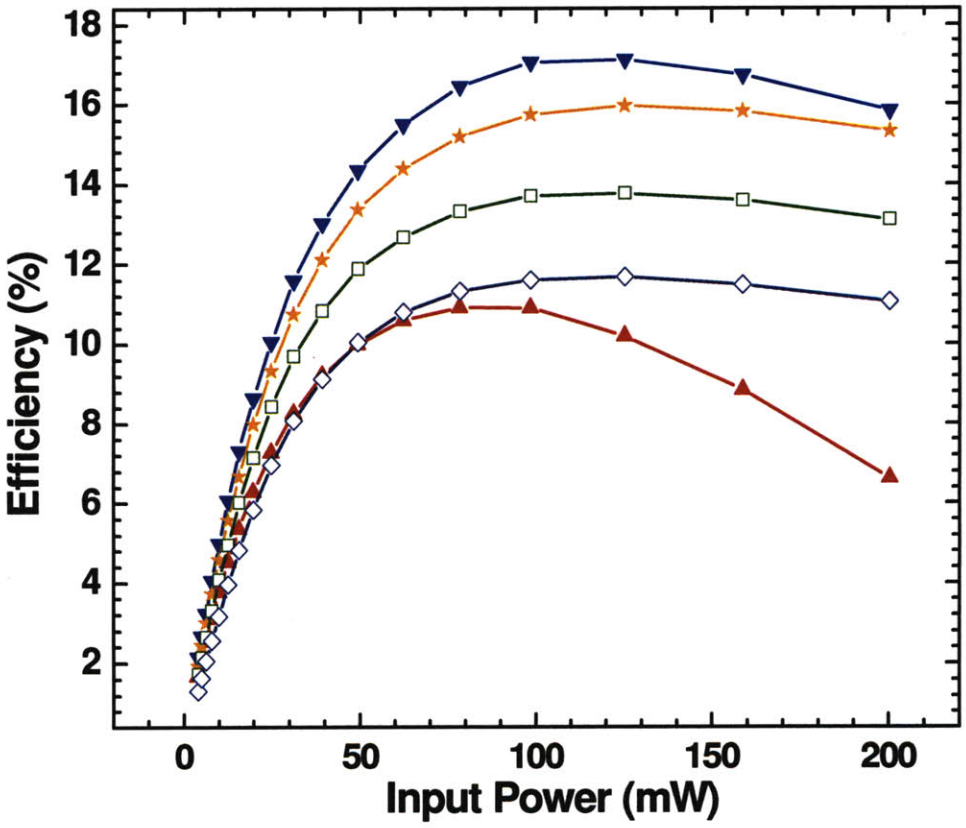

Figure 2-5: Packaged SCOWA Electrical-to-Optical Efficiency at 1 A (upright triangles), 2 A (inverted triangles), 3 A (stars), 4 A (open squares), and 5 A (open diamonds) bias currents. The SCOWA was operated at λ = 1540 nm, T = 16 °C.

The efficiency calculated here is defined as the difference between the output optical and input powers divided by the total input electrical power. The equation for the electrical-to-optical efficiency is [44]

$$\text{Electrical-to-Optical Efficiency} = \frac{P_{optical\_out} - P_{optical\_in}}{P_{electrical\_in}} \times 100\% \quad (2.1)$$

The efficiencies were calculated with the help of Figs. 2-1 and 2-4. Fig. 2-1 provides the electrical input power information, while Fig. 2-4 provides us with both the input and output optical powers. Combining the information on both plots, we were able to calculate the efficiency as a function of input optical power and bias current for 1540 nm wavelength operation. Note, in our graph, the TEC supply input electrical power is not included but should be if the total wallplug efficiency is desired.

From the graph, it is seen that the efficiency is lowest for the 1 A case. This is expected since at such low bias currents, the inversion of the amplifier is low, so that a significant fraction of the input electrical power goes into spontaneous emission and Auger recombination. At 2 A, nearly complete inversion is reached, and the efficiency peaks at >17 % at an output power of 484 mW. The efficiency decreases at higher input powers since the gain heavily saturates, and the input power receives little amplification. We attribute the drop in efficiency from 2 A to 5 A to be due to thermal effects or an increase in losses at higher bias levels. Although it is not clear what the exact mechanism causing the drop in efficiency is, we will see a similar high bias performance reduction when we discuss the noise figure measurement results of the packaged amplifier.

2.1.5 SCOWA Polarization Sensitivity

We measured the polarization sensitivity of the packaged SCOWA using the setup illustrated in Fig. 2-6.

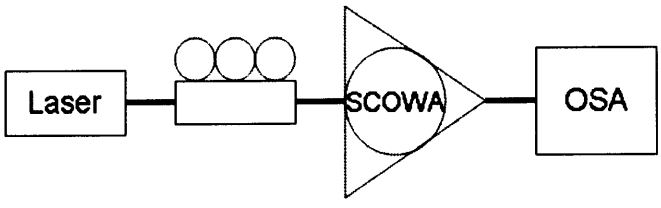

Figure 2-6: Polarization Sensitivity Measurement Setup.

A continuous wave (CW) tunable laser is sent into the polarization paddles for control of the laser polarization. The resulting output is sent into the SCOWA, and the amplified signal is measured by an optical spectrum analyzer (OSA). To determine the polarization sensitivity, the polarization paddles are first tuned to maximize the SCOWA amplified output signal. A measurement by the OSA results in the peak power in the TE polarization state (since the SCOWA output is heavily TE polarized). A second OSA measurement when the paddles are detuned to the lowest peak power results in the amplified power in the TM polarization state. The ratio of the two measurements yields the polarization extinction ratio (PER), which is defined as the ratio of the TE mode gain to the TM mode gain. This test has been performed at the wavelengths of 1460 nm, 1510 nm, and 1550 nm to verify the impact of polarization controller wavelength dispersion on the polarization extinction ratio. The results are summarized in Table 2-1.

	1460 nm	1510 nm	1550 nm
TE Mode Power	-1.58 dBm	-1.4 dBm	-3.00 dBm
TM Mode Power	-18.6 dBm	-19 dBm	-20.5 dBm
PER	17.0 dB	17.6 dB	17.5 dB

Table 2-1: Polarization extinction ratio measurements at 1460 nm, 1510 nm, and 1550 nm. The packaged SCOWA was operated at 5 A current bias and thermo-electrically cooled at 16 °C.

Table 2-1 shows that dispersion results in a ~0.6 dB variation in the polarization extinction ratio between the wavelengths 1460 nm and 1550 nm. The SCOWA output is heavily favored towards the TE polarization state with a > 50-to-1 TE/TM gain ratio. The polarization extinction ratio of the SCOWA is important in the measurement of the amplifier noise figure, as will be described in detail in section 2.2.3.

2.2 Noise Figure Optical Measurement

There are two classes of techniques (optical and electrical) that can be used to measure the noise figure of optical amplifiers. Optical methods aim to measure the ASE spectral density and the gain of the amplifier. Within the category of optical techniques, there are the polarization nulling [45, 46], the time-domain extinction [29, 47], and the interpolation source-subtraction methods [34]. In our experiments, we used the interpolation source-subtraction technique for measuring noise figure. These techniques will be described in the following sections. Afterwards, the theory, calibration, and measurement of the packaged SCOWA noise figure will be discussed in detail. Our electrical measurement techniques and results will be presented later in section 2.3.

2.2.1 Interpolation Source-Subtraction Theory

The interpolation source-subtraction technique estimates the spontaneous emission level by interpolating the spontaneous emission noise around the emission peak. This technique relies on rewriting the ASE spectral density in Eq. (1.20) as a ratio of the ASE power within a specified bandwidth to the optical bandwidth. When this is accounted for, we arrive at

$$Noise\ Factor = \frac{2P_{ASE\parallel}}{Gh\upsilon B_o} + \frac{1}{G} \tag{2.2}$$

where $P_{ASE\parallel}$ is the ASE in the same polarization state as the amplifier signal. For a polarization insensitive amplifier, the equation can be simplified further to the standard noise factor expression given by [30, 34, 46]

$$Noise\ Factor = \frac{P_{ASE}}{Gh\upsilon B_o} + \frac{1}{G} \tag{2.3}$$

where P_{ASE} is the total ASE power. From Eq. (2.3), we see that an optical spectrum analyzer (OSA) can be used to measure all of the unknown parameters. The optical frequency can be readily determined by directly reading off the center wavelength of the output light as displayed

on the OSA. The optical bandwidth is specified by the detection unit, which in this case is the OSA, and its value can be set and recorded. The gain can be computed by conducting two measurements in series. In the first measurement, the light output after amplification is detected on the OSA, and the peak power can then be read off. In the second measurement, the unamplified laser signal is directly detected with the OSA, and the peak power is again recorded. The ratio of the two powers yields the gain of the amplifier.

The last unknown, the ASE power in a unit bandwidth, however requires a two-step indirect measurement process. Here, we use interpolation to estimate the spontaneous emission level around the emission peak. Although it would appear that the ASE can be determined by just measuring this background noise, complications arise because that noise contains the additional contributions from the laser source spontaneous emission power (P_{SSE}) which is further amplified by the SOA. In mathematical terms, this is

$$P_{Noise} = P_{ASE} + G * P_{SSE} \tag{2.4}$$

Therefore, to determine the ASE power, we first measure the total noise by detecting the amplified signal on an OSA. A second measurement is then made where the amplifier is bypassed, and only the laser signal is detected by the OSA. The background noise in this case gives the SSE power of the laser. Now, a simple subtraction can be employed, where we multiply our previously measured gain with the SSE noise and subtract the result from the total noise. This yields the ASE power output of the amplifier. As long as the detection bandwidth is kept the same between both cases, the ASE noise power can be isolated and determined using the above procedure. Rewriting Eq. (2.3), we have

$$Noise\ Factor = \frac{P_{Noise} - GP_{SSE}}{Gh\upsilon B_o} + \frac{1}{G} \tag{2.5}$$

Eq. (2.5) now contains all the theory needed to determine the noise figure of optical amplifiers. Although we have assumed a polarization independent amplifier, Eq. (2.2) is completely general and can be used to measure the noise figure of any signal-spontaneous beat noise dominated optical amplifier. In section 2.2.4, we will discuss the correction factor needed to account for polarization sensitivity.

2.2.2 Noise Figure Optical Measurement System

The setup that we use for both our optical and electrical noise figure measurements is shown in Fig. 2-7.

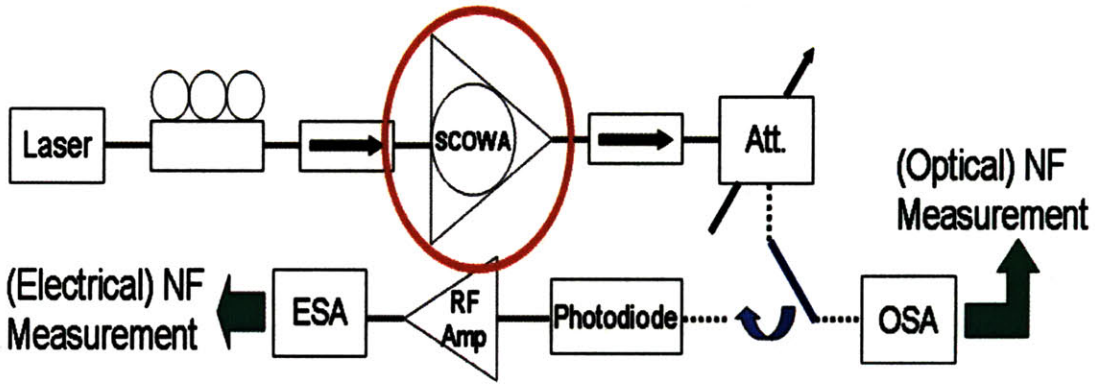

Figure 2-7: Optical and Electrical Noise Figure Measurement Setups

The optical noise figure measurements are based on the optical spectrum analyzer (OSA), while the electrical noise figure measurements utilize an electrical spectrum analyzer (ESA). We will reference this figure again when we discuss the electrical noise figure measurements since both setups share many common system components. In both configurations, an input laser source is sent to the polarization paddles in order to control the polarization state of the signal at the amplifier. The output of the polarization paddles is sent to an optical isolator, which is then sent to the SCOWA. The amplified output passes through another isolator and reaches an attenuator. The isolators are used to prevent back reflections from interfering with SCOWA operation, and the attenuator is used for controlling the intensity of the light before it is detected. After the attenuator, the signal reaches the OSA, where we use the process discussed earlier to measure the SOA noise figure parameters.

2.2.3 Noise Figure Optical Measurement Calibration

If we simply measured all the unknowns and used them in the expression for noise figure derived Eq. (2.5), we would see large errors in our results. That is, a correction needs to be made to the standard noise factor expression in order to account for the polarization dependence of the amplifier gain and ASE. Furthermore, even after this correction, we will see that the expression for noise figure still requires an absolute measurement of the ASE power. Thus, the measurement is sensitive to any losses in the fiber that occur after the amplifier output. In addition, because the OSA is used as the detection instrument, it must also be calibrated in order to yield accurate results. Finally, because of dispersion effects, the polarization controller setting for maximum gain at one wavelength may not be the setting for maximum gain at another wavelength. We will discuss each of these calibration steps in turn and also show the impact if these steps are not taken into account.

Polarization Dependence Correction

Previously, we assumed a polarization independent amplifier to obtain Eq. (2.3) since the ASE measured on the OSA is twice $P_{ASE\|}$. To account for the polarization dependence, we now introduce a factor K that multiplies the ASE term in Eq. (2.3). Here, K is given by

$$K = 2\frac{P_{ASE\|}}{P_{ASE\|} + P_{ASE\perp}} = \frac{2}{1 + P_{ASE\perp} / P_{ASE\|}} \tag{2.6}$$

where $P_{ASE\perp}$, $P_{ASE\|}$ are the ASE in the perpendicular and parallel polarization, respectfully, in relation to the laser signal polarization. The first equation for K makes it clear that K represents the fraction of the ASE in the parallel polarization compared to the total ASE. The extra factor of 2 is the result of lumping a coefficient that was originally part of the noise factor definition Eq. (2.2) into the K factor. With this correction, we then have [30]

$$Noise\ Factor = \frac{K(P_{Noise} - GP_{SSE})}{Gh\upsilon B_o} + \frac{1}{G} \tag{2.7}$$

Here, we see that K = 1 if the optical amplifier is polarization insensitive, and we recover the most common definition for noise factor given in literature. When the amplifier is polarization sensitive, however, K becomes a number between 1 and 2 depending on the degree of polarization dependence of the amplifier. In nearly all cases, a polarization sensitive amplifier will have K ~ 2 since K quickly approaches 2 even for moderate levels of polarization dependence. For our packaged SCOWA, we find K to be 1.965 at 1550 nm based on the discussion in section 2.1.5.

Polarization sensitivity can introduce up to a 3 dB decrease in calculated noise figure if the polarization dependence of the amplifier is not accounted for. However, most sources in literature use the standard polarization insensitive noise figure expression. The reason for this is mostly due to the fact that polarization insensitivity is most critical for in-line and pre-amplifier applications. Currently, EDFAs are the dominant technology for these purposes, and they are typically polarization independent. As a result, there has been little need to account for polarization in the noise figure expression. For these reasons, many of the noise figures reported in literature for polarization dependent amplifiers should be interpreted with caution [5, 26]. Furthermore, it is common practice to specify noise figure results neglecting input coupling losses to the amplifier. However, any coupling losses at the input directly degrade the noise figure measured Eq. (1.27). Thus, an understanding of the assumptions in published results is critical in order to accurately analyze the noise figure of optical amplifiers.

Loss Correction

Losses in the system must be accounted for in order to accurately measure the noise figure of an optical amplifier. However, as seen in Fig. 2-8, only the output losses have an impact on the noise figure. This can be understood in reference to Eqs. (2.4) and (2.5) where we see that there are only two parameters that can possibly depend on the loss within the system, P_{ASE} and G. However, to determine the gain of the amplifier, we divide the output when the amplifier is present by the output when the amplifier is taken out. Thus, any loss that is not intrinsic to the amplifier itself will cancel out and will not affect the gain. As a result, the only term influenced by loss within the system is P_{ASE}.

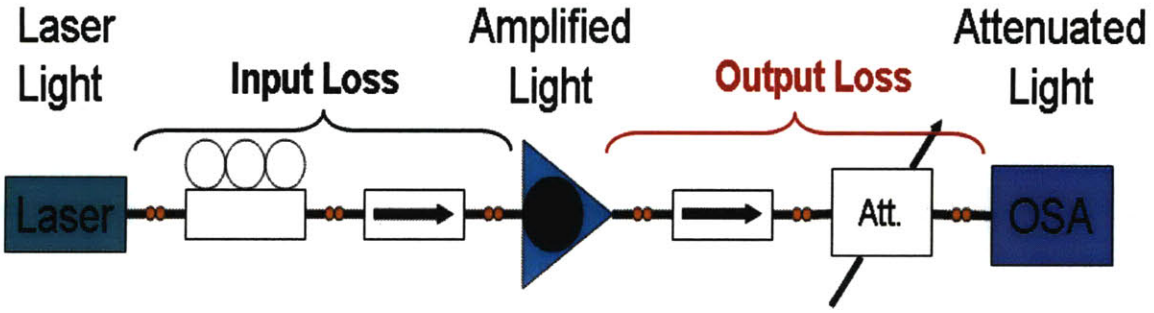

Figure 2-8: Illustration of Output Loss Concept

Since P_{ASE} is generated within the amplifier itself, the ASE power that reaches the OSA does not see any of the losses before the amplifier. Therefore, input losses become irrelevant to the interpolation source-subtraction measurement of noise figure as long as the signal from the laser can be detected by the OSA. Output losses, however, directly decrease the ASE power measured and thus cause the noise figure to appear lower than expected if the losses are not accounted for. To measure the output losses, a separate measurement is performed. For these purposes, the test laser source is input directly into the output isolator of the amplifier, and its signal is measured on the OSA. Next, the test laser itself is input into the OSA, and again a measurement is made. The ratio of the two measurements gives an estimate for the output loss of the system. If we define β as the inverse of this loss, then the corrected noise factor equation accounting for loss is

$$Noise\ Factor = \frac{\beta K(P_{Noise} - GP_{SSE})}{Gh\upsilon B_o} + \frac{1}{G}. \tag{2.8}$$

OSA Calibration

Often, the reading displayed on the OSA will be slightly off calibration as compared to the true value of the reading. To correct for this, the OSA can be calibrated by referencing its displayed output to a calibrated optical power meter. This can be done by first directly inputting a laser's output into a power meter. Typically, the SSE is much smaller in power than the signal and so is negligible compared to the lasing peak. Thus, the power measured on the reference power meter is a very good approximation for the signal power of the lasing peak. We can then send the same

laser output into the OSA. If the laser's linewidth is narrow enough, one resolution bandwidth of the OSA will encapsulate the peak and also some of the source spontaneous emission noise. The SSE is usually much lower in power compared to the signal, and the power measured in one resolution bandwidth is approximately the signal power. A comparison between the powers measured by the power meter standard and the OSA yields the calibration factor of the OSA.

Fig. 2-9 shows the OSA – power meter calibration ratio as a function of power meter power. We see that the relationship between the two quantities is approximately linear. The slope of the line represents the calibration factor of the OSA, and is 0.73 in this case. The offset, which is 0.474 nW from the figure, is mainly due to the noise floor of the power meter. However, it has negligible effect on the calibration factor between the OSA and the power meter. The laser output power was attenuated to the nano-watt level in order to accurately determine the level of the offset noise floor.

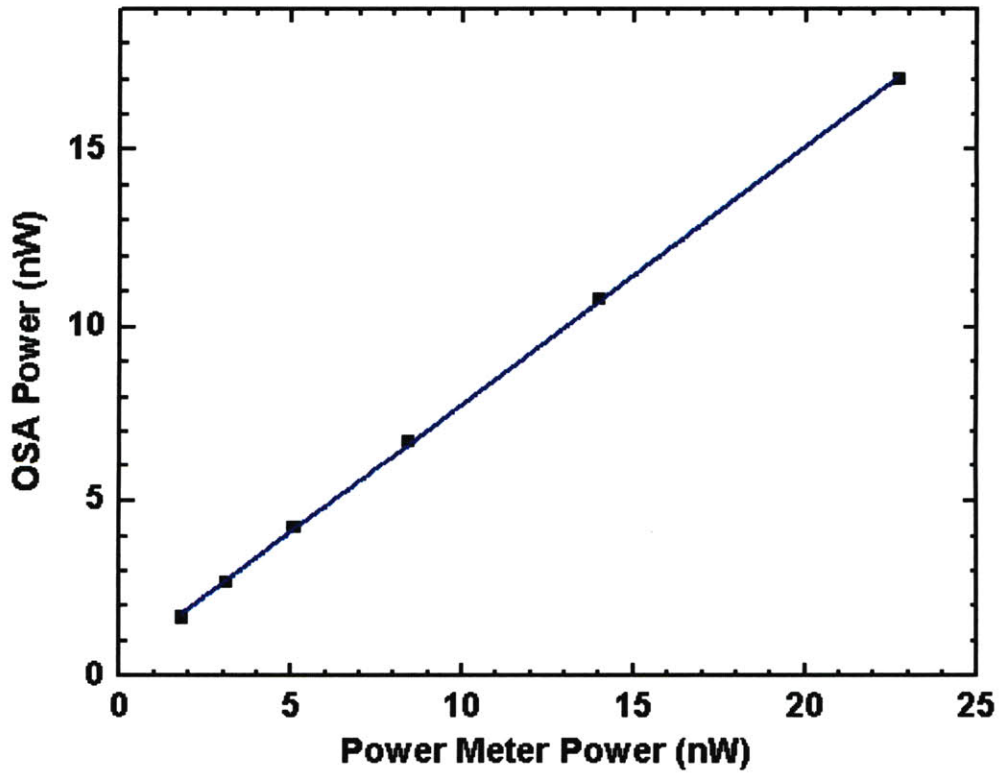

Figure 2-9: Calibration Ratio between OSA and Power Meter at 1550 nm. The extrapolated best fit line is OSA = 0.73*PM + 0.494 (nW) where OSA and PM designate the measured OSA and power meter powers.

In calibrating the OSA, it is important to evaluate how well the calibration holds across the different operating power levels and wavelength ranges. Although the effects of power level on the calibration ratio are not shown here, testing at higher power levels yielded very similar results. Furthermore, Fig. 2-10 shows the robustness of the calibration ratio across the 1510 nm – 1580 nm wavelength range. The data for the graph was taken by sending the output of a tunable laser to a nominally 99/1 splitter with the 99% branch interfaced to the OSA and the 1% branch interfaced to the power meter. Careful measurement of the splitter yielded a measured splitting ratio of 99.28/0.72. The wavelength is swept from 1510 nm to 1580 nm in 10 nm steps. However, the laser output power was not swept during our testing.

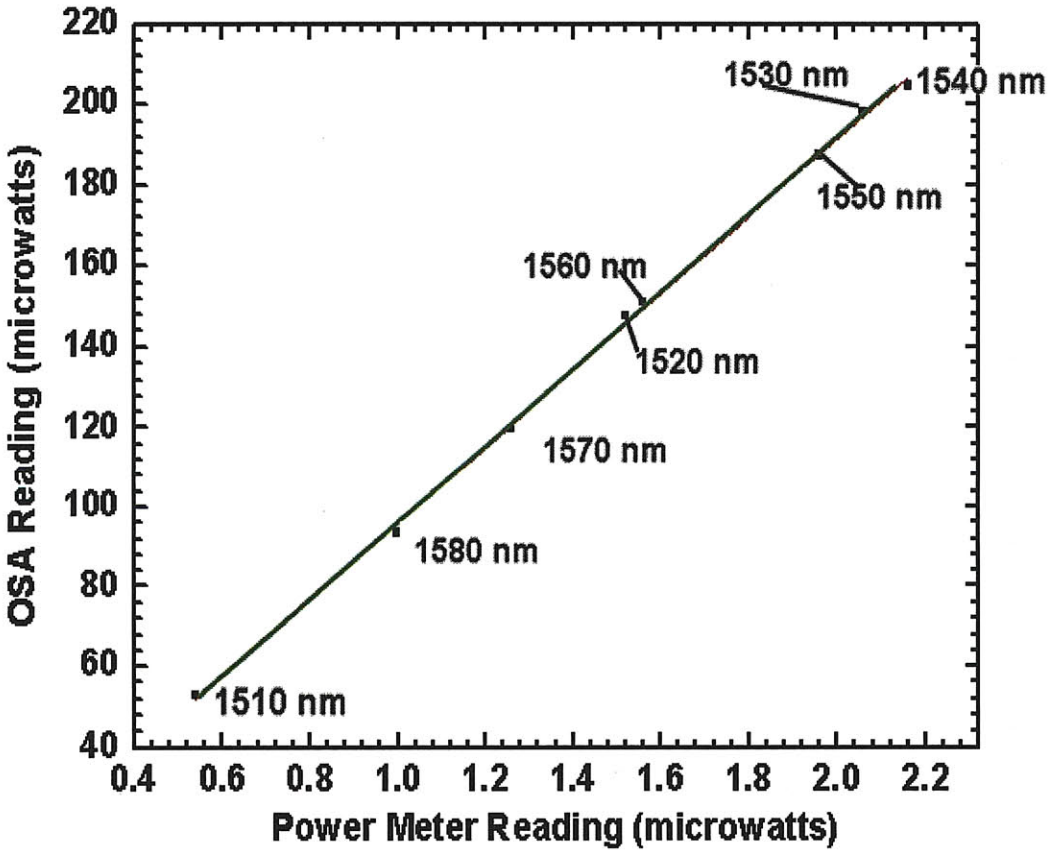

Figure 2-10: Calibration Ratio between OSA and Power Meter across various wavelengths. The extrapolated best fit line is OSA = 0.717*PM where OSA and PM designate the measured OSA and power meter powers.

The range of laser powers seen is due solely to the dependence of output power on wavelength for our laser. The calibration ratio between the OSA and the power meter is given by the slope of the points plotted on the graph. Accounting for the splitting ratio, we find the calibration factor to be 0.717. This estimate agrees well with our earlier estimate of 0.73, which validates the use of the same calibration ratio across the various power and wavelength ranges required for our testing.

Polarization Controller Dispersion Correction

Due to the presence of dispersion in the fiber-based polarization controller, the maximum gain setting at one wavelength may not correspond to the maximum gain setting at another wavelength. However, in many cases it is desirable to use computers to automate the data acquisition process. This presents a problem in our noise figure measurements since the laser wavelength needs to be swept while maintaining the same setup conditions. In this case, dispersion can cause our results to be largely different from what is expected. Here, we develop the theory to compensate for this effect. We begin first by using Eq. 2.8 to write an expression for the noise figure assuming a small fraction of the input signal to the amplifier is polarized in the TM orientation.

$$NF' = \frac{\beta K(P_{Noise} - G'P_{SSE})}{G'h\upsilon B_o} + \frac{1}{G'} \tag{2.9}$$

Here, NF' is the noise figure one would measure if the polarization paddles are not optimized for the SCOWA polarization dependence, and G' is the corresponding gain. The rest of the variables retain their original definitions. If we assume that the dispersion effects are relatively weak such that G' is still large, then we can approximately neglect the $\frac{1}{G'}$ term. Now, P_{Noise} is the sum of the SCOWA ASE power and the gain of the amplifier multiplied by the source spontaneous emission noise.

$$NF' = \frac{\beta K(P_{ASE} + G_{TE}P_{SSE,TE} + G_{TM}P_{SSE,TM} - G'P_{SSE})}{G'h\upsilon B_o} \tag{2.10}$$

In Eq. 2.10, we broke the source spontaneous emission into its TE and TM components such that $P_{SSE,TM}$ + $P_{SSE,TE}$ equals P_{SSE}. Also G_{TE} and G_{TM} are the TE and TM gains of the amplifier respectively. Here, G' is the gain measured when a fraction of the input signal is in the TM state. G' can be expressed as

$$G' = \frac{G_{TE}P_{SSE,TE} + G_{TM}P_{SSE,TM}}{P_{SSE}}. \tag{2.11}$$

When this expression is substituted into Eq. 2.10, we find that

$$NF' = \frac{\beta K(P_{ASE} + G_{TE}P_{SSE,TE} + G_{TM}P_{SSE,TM} - (G_{TE}P_{SSE,TE} + G_{TM}P_{SSE,TM}))}{G'h\upsilon B_o} = \frac{\beta KP_{ASE}}{G'h\upsilon B_o}. \tag{2.12}$$

This can be directly compared to the noise figure expression when none of the input signal is in the TM state

$$NF = \frac{\beta KP_{ASE}}{Gh\upsilon B_o}. \tag{2.13}$$

From Eqs. 2.12 and 2.13, we see that the effect of dispersion on the gain directly results in an increase in the noise figure since gain and noise figure are inversely related. Dispersion behaves similarly to input coupling loss in this respect, which is expected since any power in the orthogonal polarization state is lost. We can divide Eqs. 2.12 and 2.13 to find that

$$\frac{NF'}{NF} = \frac{G}{G'}. \tag{2.14}$$

From Eq. 2.14, we see that if dispersion resulted in an inaccurately measured gain and noise figure of G' and NF' respectively, then it is possible to determine the true NF of the SCOWA if we know what the TE polarization gain is. Since the TE gain measurement can be performed separately, the effects of dispersion can be corrected for after all the initial measurements are finished. Our packaged SCOWA noise figure results, which will be presented in the next section, are calculated using Eq. 2.14.

2.2.4 Noise Figure Optical Measurement Results

The noise figure of the packaged SCOWA was experimentally measured using the interpolation source-subtraction technique. The results are plotted in Fig. 2-11. The results show that the SCOWA noise figure is 5.5 dB at 1550 nm and 5 A bias. A minimum noise figure of ~ 4.5 dB is achieved when operating the SCOWA at ~1550 nm wavelength and at 2 A bias. The noise figure values remain nearly constant over a > 60 nm wavelength range from 1520 nm to > 1580 nm. These characteristics are favorable for amplifiers in WDM applications where low noise amplification over a large bandwidth is required.

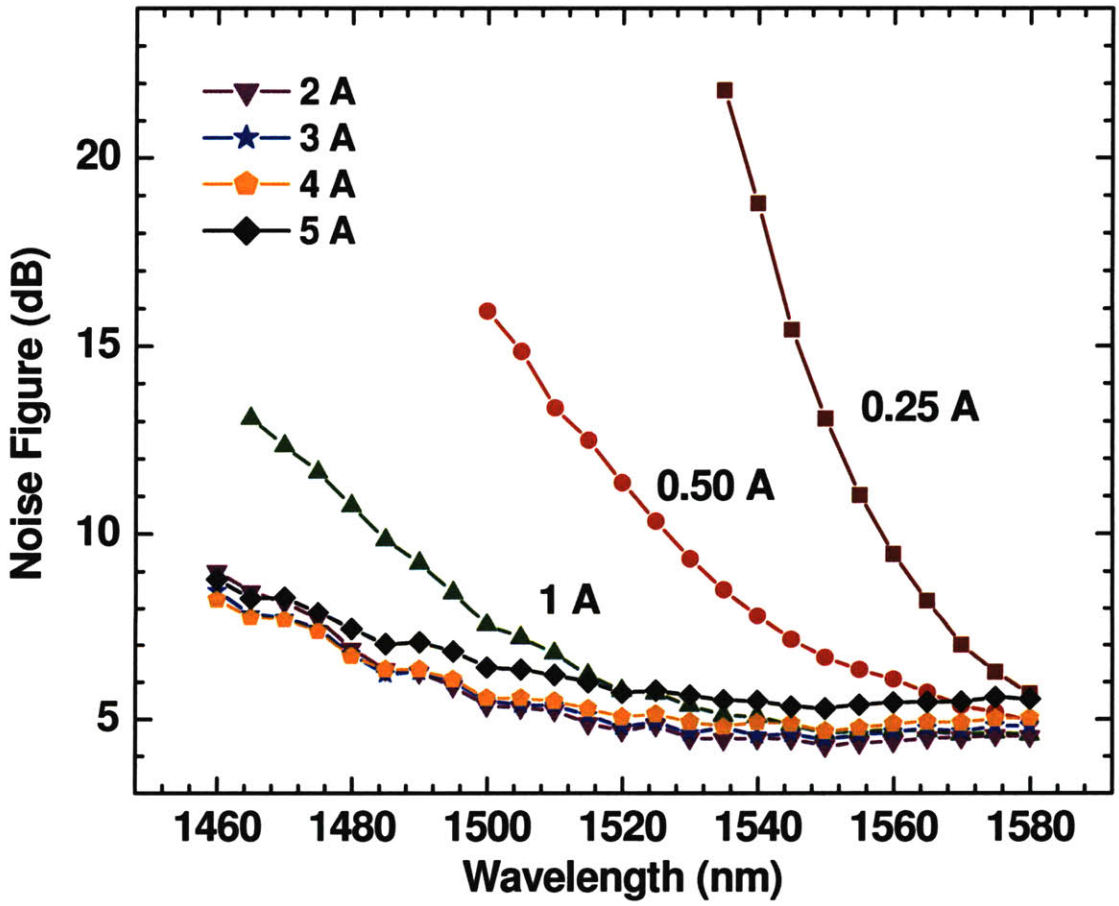

Figure 2-11: Noise Figure of packaged SCOWA for currents 0.25 A – 5 A and wavelengths 1460 nm – 1580 nm The SCOWA was operated at T = 16 ºC.

Typical SOAs have noise figures between 7-11 dB [48]. Their large noise figures are due to the high coupling losses of semiconductor devices. Here, we see that the very high (> 90%) coupling efficiency that the SCOWA achieves allows it to obtain much lower noise figures compared to conventional SOAs. EDFAs can achieve even lower noise figures with some optical amplifiers reaching the 3 dB high gain limit. However, high power EDFAs are still far from these limits. Their noise properties have currently not been proven to be any better those of the SCOWA.

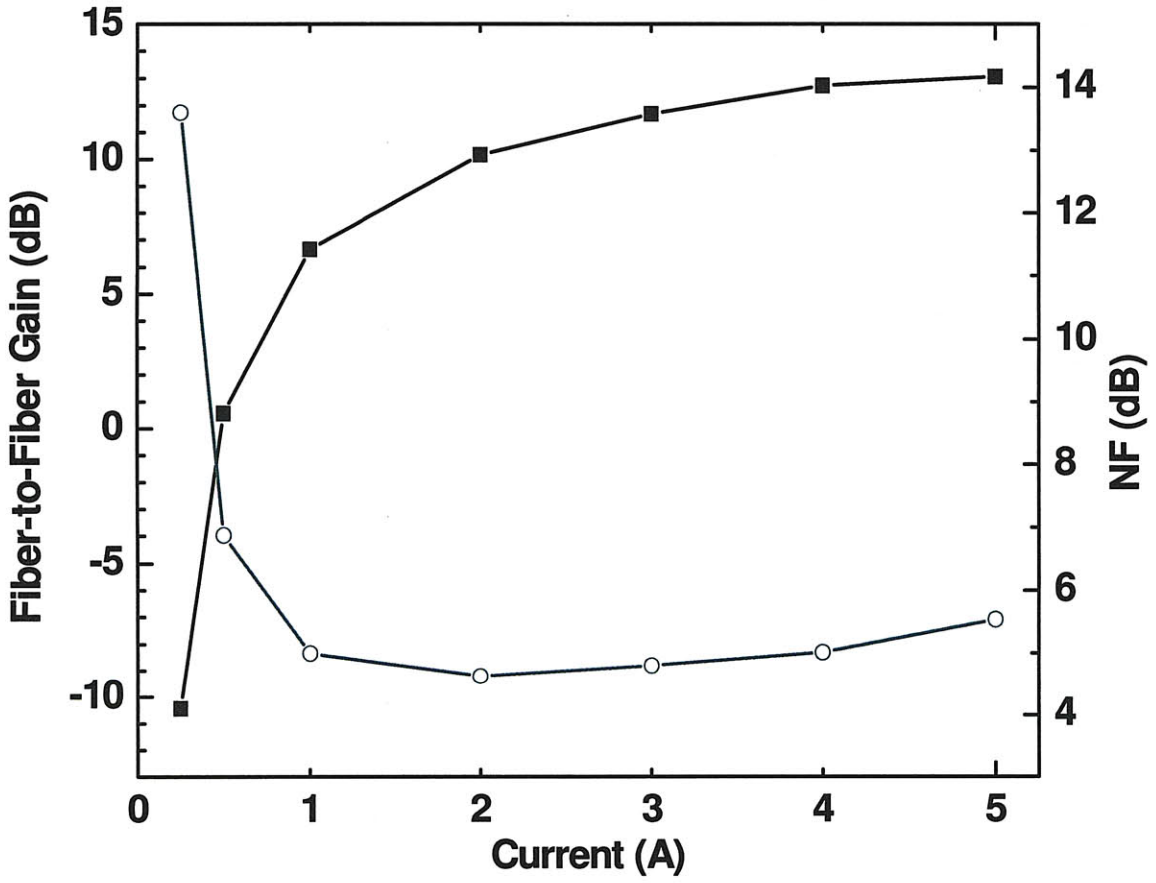

Figure 2-12: Packaged SCOWA Fiber-to-Fiber Gain (squares) and Noise Figure (open circles) as a function of current. The SCOWA was operated at λ = 1550 nm and T = 16 °C.

From Fig. 2-11, we see that the noise figure increases when the SCOWA is operated on the shorter wavelength side. Shorter wavelengths correspond to higher energy states where the population inversion is lower for a particular bias. As seen from Eq. (1.27), an increase in the

inversion factor leads to an increase in the noise figure of the amplifier. This effect is most dramatic when the current is < 1 A. The inversion factor also accounts for the decrease in noise figure when the bias current is increased from 0.25 A to 2 A. The inversion factor decreases with increasing bias signifying a higher inversion of the gain medium and a lower noise figure. However, as the bias current is increased past 2 A, the noise figure surprisingly begins to increase with bias. Currently, the exact cause for this phenomenon is unclear. However, some possible explanations are an increase in thermal effects or an increase in loss with increasing bias. Thermal effects can result in mode repositioning which leads to a decrease in lensed fiber coupling. Thermally induced carrier leakage can also occur, leading to a degradation in performance. Finally, increased intervalence band absorption can result from the high bias conditions. This degradation in performance with increasing bias was also previously seen in our efficiency measurements in Fig. 2-5.

Fig. 2-12 shows the fiber-to-fiber gain and noise figure as a function of the SCOWA bias current. The SCOWA was probed with a 1550 nm small signal laser. The results of the fiber-to-fiber gain and noise figure measurements are generally as expected since we expect the gain to increase and the noise figure to decrease with increasing current. The change in the gain and noise figure with increasing bias is initially fast because the population inversion of the active medium changes fast at low biases. These gain and noise figure variations become slower as the medium nears full inversion. The deviation of the noise figure trend at higher currents was briefly discussed previously.

2.3 Noise Figure Electrical Measurement

To confirm the results of our optical measurements of the noise figure, we performed electrical noise figure measurements on our packaged SCOWA. Electrical measurements differ from optical measurements in that electrical measurements directly measure the total noise of the amplifier. In this way, electrical measurements provide a more complete analysis of the amplifier noise as they measure all the noise contributions at the amplifier output. In this section, we detail the theory relevant to electrical noise figure measurements. We also discuss the setup and calibration for these measurements, and we conclude with a summary of the obtained results.

2.3.1 Noise Figure Electrical Measurement Theory

Noise Figure Expression

The electrical measurement of the optical amplifier noise figure is performed by detecting the amplifier output signal with a photodiode and recording its spectrum on an electrical spectrum analyzer. To describe the theory of this measurement process, we again begin with the standard noise factor expression given in Eq. (1.6). Using the fact that the output signal is the gain of the optical amplifier (G) multiplied by the input, we have

$$\frac{SNR_{in}}{SNR_{out}} = \frac{\left\langle i_{signal}^2 \right\rangle_{in} / \left\langle i_{noise}^2 \right\rangle_{in}}{\left\langle i_{signal}^2 \right\rangle_{out} / \left\langle i_{noise}^2 \right\rangle_{out}} = \frac{1}{G^2} \frac{\left\langle i_{noise}^2 \right\rangle_{out}}{\left\langle i_{noise}^2 \right\rangle_{in}}. \tag{2.15}$$

The input noise is taken to be shot noise limited in the NF, so we have

$$\left\langle i_{noise}^2 \right\rangle_{in} = 2q\Re_{ideal} P_{in}. \tag{2.16}$$

Here $\Re_{ideal}$ is the responsivity of the photodiode with ideal quantum efficiency ($\eta = 1$), and P_{in} is the optical input to the optical amplifier. The output noise is composed of the shot noise contribution and the excess noise added by the amplifier. Thus, we have

$$\left\langle i_{noise}^2 \right\rangle_{out} = 2q\Re_{ideal} P_{in} G + N_{OA}. \tag{2.17}$$

N_{OA} denotes the mean square of the optical amplifier noise current contribution. Under these conditions, it can be shown that [49]

$$\text{Noise Factor} = \frac{N_{OA} P_{IN}}{2h\upsilon I^2} + \frac{1}{G} \tag{2.18}$$

Here, I is the photocurrent produced by the photodiode. This equation accounts for all losses and nonidealities within the measurement process and is completely general as long as N_{OA} can be determined.

To determine N_{OA}, we note that in general, the total noise measured by the RF Spectrum Analyzer will be dominated by contributions from the optical amplifier noise, shot noise, thermal noise, and the laser source RIN. For a constant received power, both shot noise and the laser source's RIN are constant. Furthermore, the thermal noise of the system will be the same if the load resistor is kept the same. Therefore, to find N_{OA}, we make two measurements of the total noise on the spectrum analyzer. In the first measurement, the amplifier is inserted and the total noise within the measurement bandwidth (P_{N1}) is obtained. In the second measurement, the amplifier is removed, but the total optical power reaching the photodiode is held constant. A measurement on the RF spectrum analyzer yields P_{N2}. The difference between the two measurements yields N_{OA}. These noise sources are all represented as current noise sources in a unit electrical bandwidth. Therefore, to convert the measured voltage signal at the input of the electrical spectrum analyzer to current, division by the system impedance (Z) and bandwidth (B_e) is necessary. The resulting noise factor expression becomes [49]

$$\text{Noise Factor} = \frac{(P_{N1} - P_{N2})P_{in}}{2h\upsilon I^2 Z B_e} + \frac{1}{G}. \tag{2.19}$$

The measurement unknowns left to find are P_{in}, I, and G, Z, and B_e. The amplifier optical input (P_{in}) can be easily measured using a power meter, and the photocurrent (I) can be determined using an ammeter. Finally the gain of the optical amplifier can be measured using a two step measurement process. In the first step, an OSA is used to record the amplifier output power driven by a tunable seed laser. In the next step, the amplifier is taken out of the system, and the seed laser power is measured. The ratio of the two measurements yields the gain. Thus, once the transfer function $Z \times B_e$ is determined, the noise figure of the optical amplifier can be calculated.

RIN Transfer Standard

One technique for determining the transfer function of the system is the RIN Transfer Standard method [50]. This method calculates the RIN of a test optical source and compares that RIN to the measured RIN of the source. The ratio of the two yields exactly the system transfer function. The receiver system is kept in the same configuration as the noise figure system so that the measured transfer function parameters directly apply to the noise figure measurement.

The RIN at any frequency can be calculated by taking the autocorrelation of the optical spectrum $S(\upsilon)$ and normalizing the result to the square of the total power (P) [50]

$$R(f) = \int_0^\infty \frac{S(\upsilon)S(\upsilon+f)}{P^2} d\upsilon . \tag{2.20}$$

Typically, filters are used to limit the bandwidth of the optical spectrum. Eq. (2.20) only applies for thermal or Gaussian light sources whose excess RIN due to spontaneous-spontaneous beating is much higher than the shot noise RIN. Also, the RIN expression is only valid for unpolarized light. For polarized light, an extra factor of 2 needs to be included. With these two considerations in mind, we see from Eq. 2.20 that a simple measurement of the source's optical spectrum allows us to determine its theoretical RIN.

Next, the RIN of the optical source is measured by sending its output through the noise figure receiver system. Upon normalizing the spectrum on the electrical spectrum analyzer to the square of the optical power, we obtain the RIN of the optical source as a function of frequency. This RIN already incorporates both the system impedance and integration bandwidth since both effects are intertwined within the measurement process. Therefore, by taking the ratio of the measured RIN to the calculated RIN, we obtain the system transfer function as

$$Z \times B_e = \frac{RIN_{Measured}}{RIN_{Calculated}} . \tag{2.21}$$

2.3.2 Noise Figure Electrical Measurement System

The setup used for the electrical measurements of the noise figure was given previously in Fig. 2-7. The electrical and optical noise figure measurements share the same initial setup but differ at the output of the optical attenuator. In the electrical measurement, the output of the attenuator is passed to a photodiode. The photocurrent generated is converted to a voltage signal after passage through impedance matching resistors. This voltage is amplified by an RF amplifier and is afterwards sent to an electrical spectrum analyzer for measurement of the photocurrent spectral density.

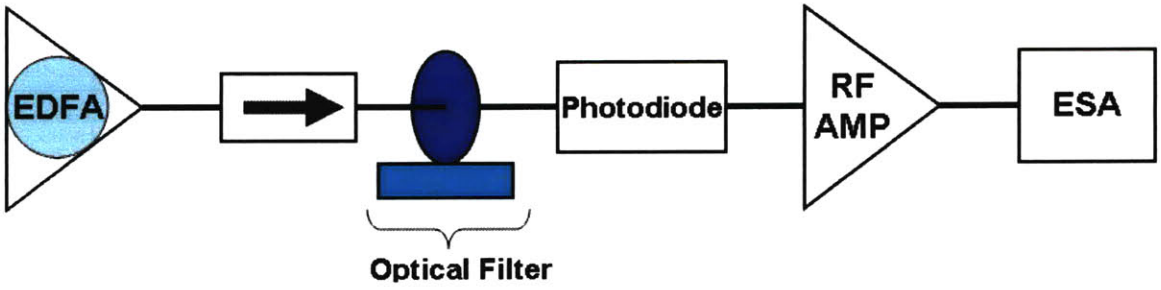

Figure 2-13: RIN Transfer Standard test setup

The electrical noise figure measurement also requires a separate setup to measure the system transfer function, as discussed in section 2.3.1. This measurement system is illustrated in Fig. 2-13. We use a filtered EDFA as the optical source for our RIN Standard. The filter is free-space coupled and has a ~ 14 nm bandwidth centered at 1550 nm. The photodiode we used had a ~1 GHz bandwidth and a responsivity ~0.95. The RF amplifier in our system has a bandwidth of ~3.15 GHz and a nominal gain of 25 dB. Finally, the electrical spectrum analyzer used records the spontaneous-spontaneous beat noise power as a function of frequency within the passband of the photodiode.

2.3.3 Noise Figure Electrical Measurement Results

The results of the electrical noise figure measurements performed on the packaged SCOWA are shown in Fig. 2-14. The results of the optical measurement are also shown for comparison purposes. From the figure, we see that the optical and electrical techniques for noise figure measurement agree to better than a tenth of a dB. The precise calibration of the measurement techniques allows for this excellent agreement to be obtained. The agreement also gives us confidence that the noise figure of the packaged amplifier has been accurately measured. It is the combination of high coupling efficiency and low loss that drives the noise figure to be so low in SCOWA devices. Furthermore, a low confinement factor helps to prevent early saturation in the front end of the amplifier, which also improves its noise properties [51].

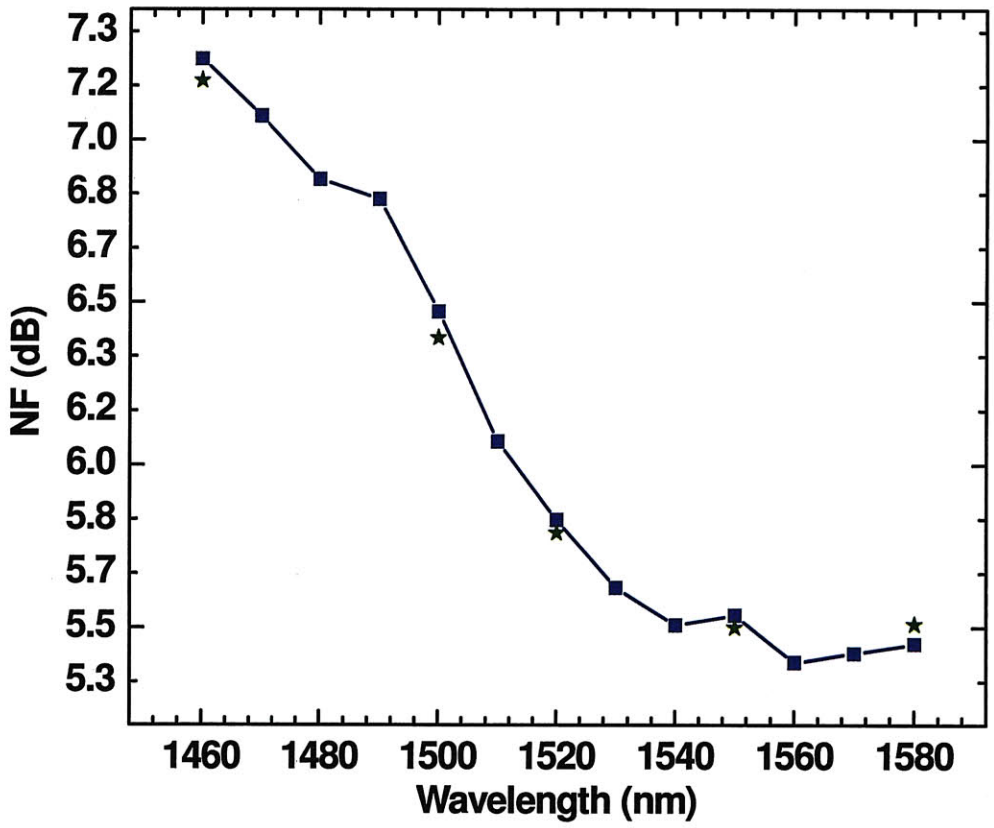

Figure 2-14: Packaged SCOWA noise figure measured using optical technique (squares) and electrical technique (stars). The SCOWA was operated at T = 16 °C.

2.4 Population Inversion Factor of Packaged SCOWA

The population inversion factor (n_{sp}) is a parameter denoting the ratio of the spontaneous emission rate to the stimulated emission rate for an optical device. It can be extracted from noise figure measurements since noise and spontaneous emission are inherently related. n_{sp} ranges from 0 to -∞ when the device operates below the population inversion threshold and from ∞ to 1 above this threshold. In this section, we determine the population inversion factor of the packaged SCOWA using the experimentally measured noise figure values. The population inversion factor is also derived using measured I-V data. The results using both methods are compared and discussed within this section.

2.4.1 Population Inversion Factor from Noise Figure Measurement

Once the noise figure is known, the population inversion factor can be found by solving for n_{sp} in Eq. 1.27. Values for the coupling efficiency, internal loss, and confinement factor are needed in order to obtain numerical results. For the SCOWA, these values have been measured to be $\eta_c \sim 90\%$, $\alpha \sim 0.5\ \text{cm}^{-1}$, and $\Gamma \sim 0.5\%$. The amplifier chip gain (G_{amp}) and modal gain (Γg) are also required parameters for determining n_{sp}. The chip gain can be determined by accounting for coupling losses in measured values of fiber-to-fiber gain. Furthermore, the modal gain can be obtained using the calculated chip gain in Eq. 1.2. Using this method, the population inversion factor of the SCOWA has been calculated as a function of wavelength, and the results are illustrated in Figs. 2-15 – 2-21.

2.4.2 Population Inversion Factor from IV Measurement

To confirm the population inversion factors obtained using measured values of noise figures, we calculate n_{sp} using an alternate formulation

$$n_{sp} = \frac{1}{1 - e^{(E_{21} - \Delta E_F)/kT}}. \tag{2.22}$$

Here, E_{21} is the transition energy, ΔE_F is the energy difference between electron and hole Fermi levels, and T is the electron temperature. Eq. (2.22) results from the definition of the population inversion factor after expressing the spontaneous and net stimulated emission rates in terms of corresponding Fermi factors. As a first order approximation, we ignore the dependence of the electron temperature on bias current and assume a value of T = 289 K. This approximation is expected to lose accuracy at higher biases; however, it is nevertheless useful for the purposes of obtaining numerical estimates.

The other unknown, ΔE_F, can be measured by performing a current-voltage sweep. As in any diode, the misalignment of the Fermi levels is exactly equal to the applied junction voltage. The applied voltage can be determined using the I-V measurement of Fig. 2-1 by accounting for

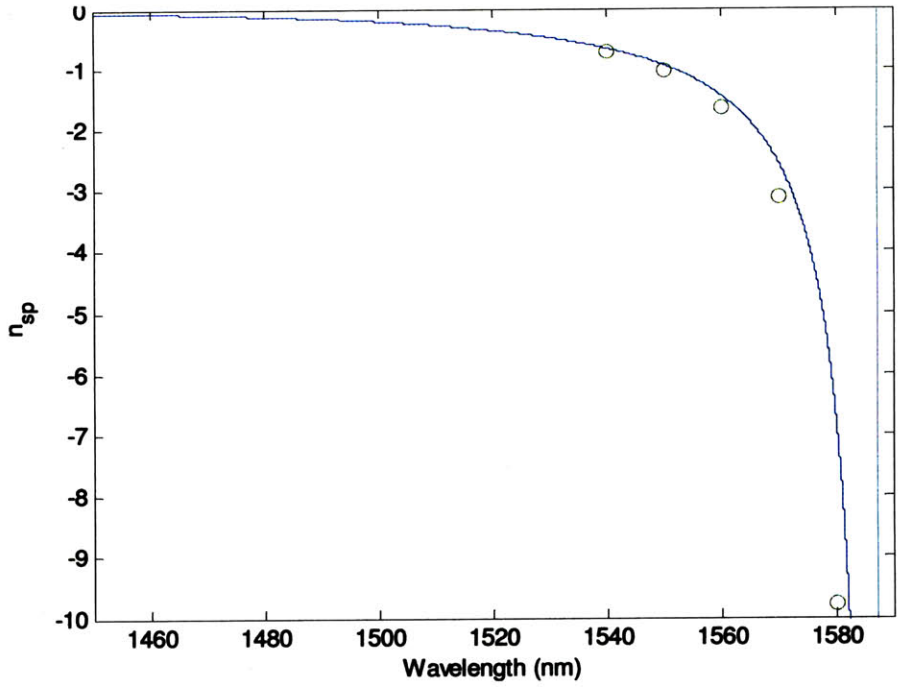

Figure 2-15: Plot of n_{sp} as a function of wavelength for I_{BIAS} = 0.25 A calculated using noise figure measurements (circles) and IV measurements (solid line).

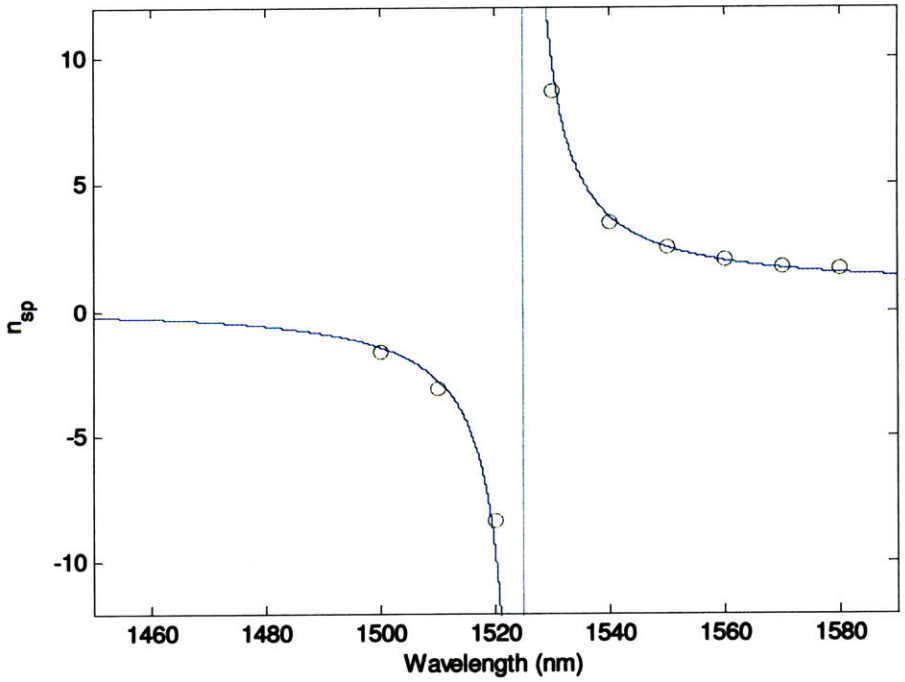

Figure 2-16: Plot of n_{sp} as a function of wavelength for I_{BIAS} = 0.50 A calculated using noise figure measurements (circles) and IV measurements (solid line).

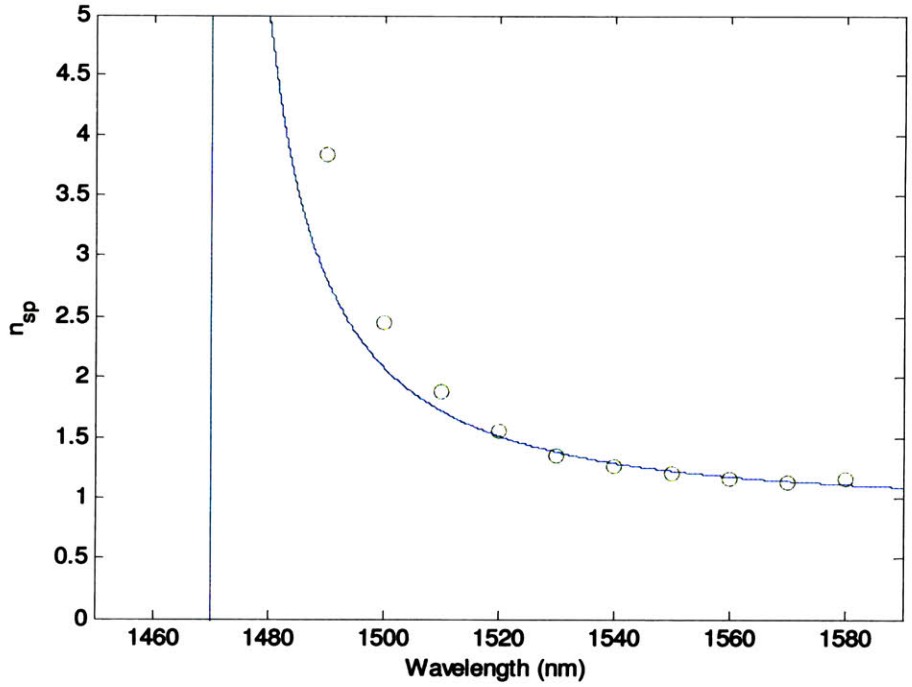

Figure 2-17: Plot of n_{sp} as a function of wavelength for I_{BIAS} = 1 A calculated using noise figure measurements (circles) and IV measurements (solid line).

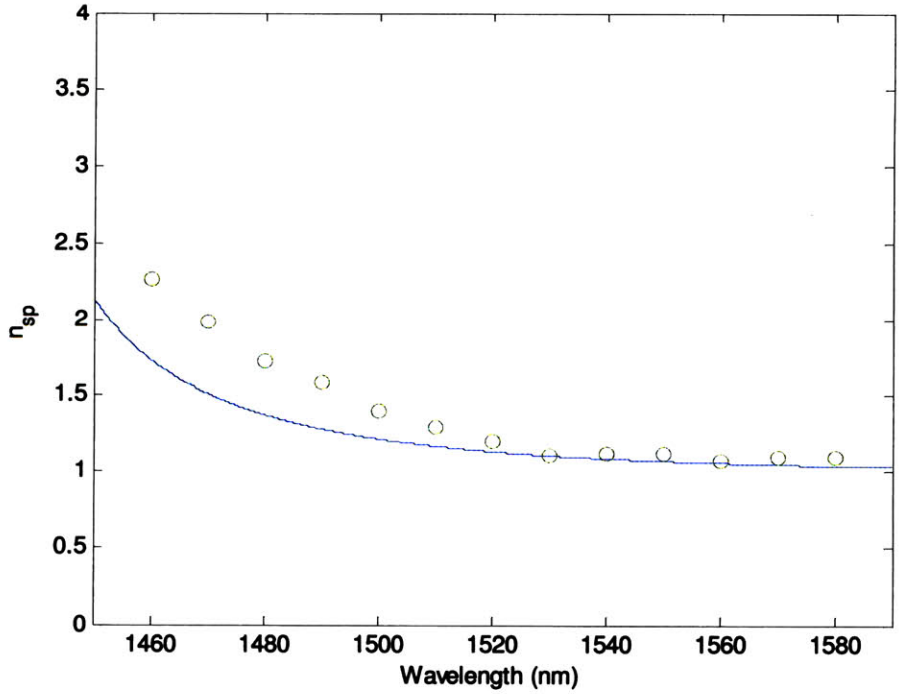

Figure 2-18: Plot of n_{sp} as a function of wavelength for I_{BIAS} = 2 A calculated using noise figure measurements (circles) and IV measurements (solid line).

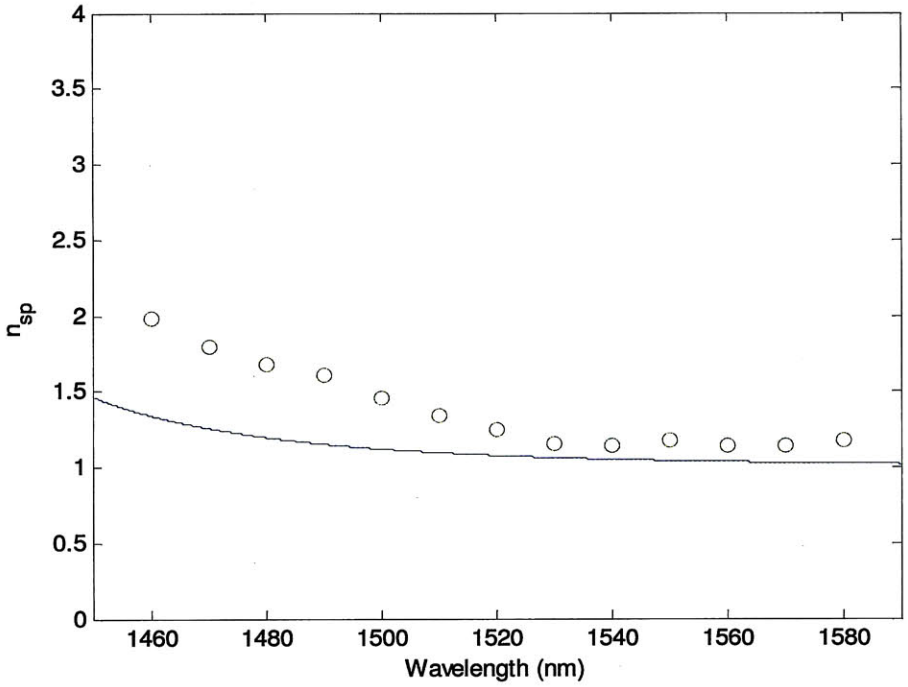

Figure 2-19: Plot of n_{sp} as a function of wavelength for I_{BIAS} = 3 A calculated using noise figure measurements (circles) and IV measurements (solid line).

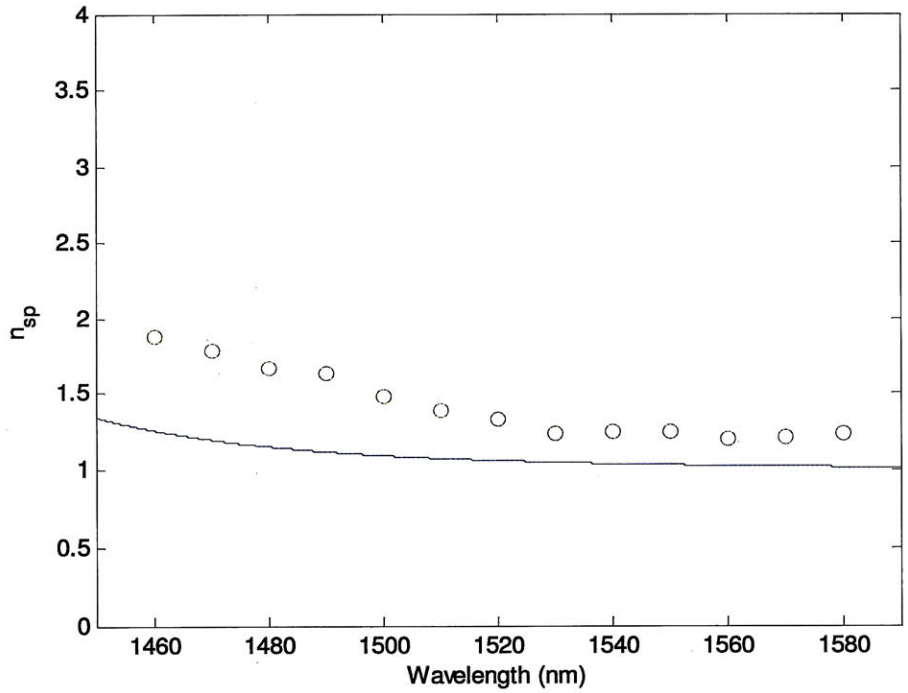

Figure 2-20: Plot of n_{sp} as a function of wavelength for I_{BIAS} = 4 A calculated using noise figure measurements (circles) and IV measurements (solid line).

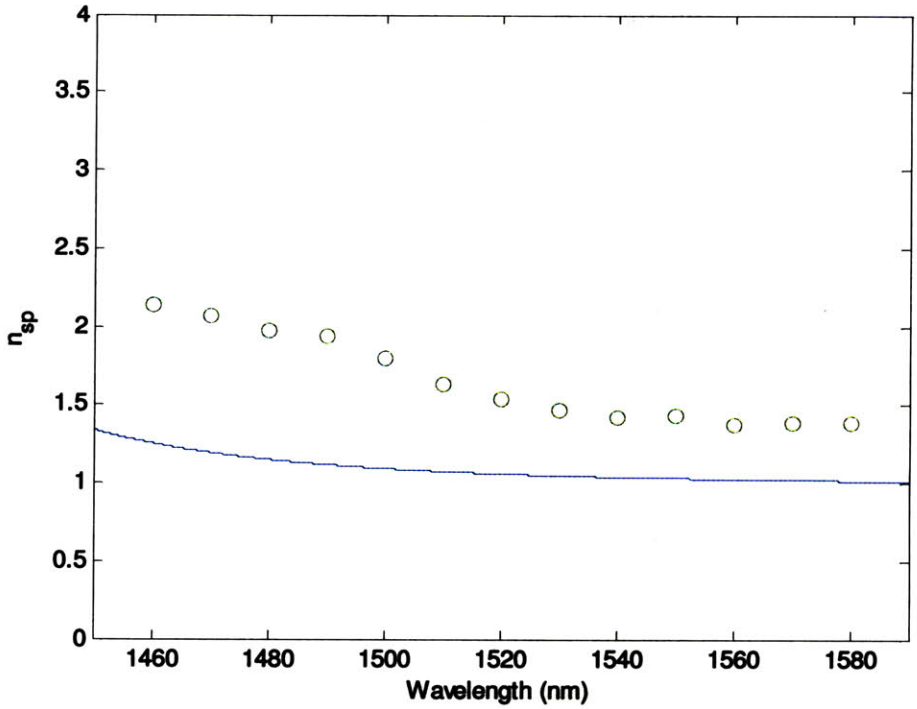

Figure 2-21: Plot of n_{sp} as a function of wavelength for I_{BIAS} = 5 A calculated using noise figure measurements (circles) and IV measurements (solid line).

the voltage drop across the series resistance of the contacts and of the diode itself. The series resistance is measured by taking the slope of a linear fit to the IV relation at high biases (where the diode junction resistance is negligible). The calculated n_{sp} using this technique is shown in Figs. 2-15 – 2-21 alongside with the n_{sp} calculated from the measured noise figure values.

2.4.3 Comparison and Discussion of Results

From the Figs 2.15 – 2.21, it can be seen that a singularity exists for the population inversion factor curves under low current bias operating conditions. The singularity represents the population inversion threshold. Wavelengths above this threshold will receive gain, as long as their corresponding photon energies are above the active layer bandgap. For those wavelengths, population inversion factors closer to 1 signify wavelength transitions which are more inverted. Below the population inversion threshold, n_{sp} becomes negative. This is an artifact acquired from defining the population inversion factor as the ratio of the spontaneous emission rate to the net

single photon stimulated emission rate. The net stimulated emission rate is negative for wavelengths below the population inversion threshold since those wavelengths have net loss. This yields a negative value for the population inversion factor. In this regime, n_{sp} tends towards zero as the absorption rate begins to dominate over the spontaneous emission rate. From the definition of n_{sp}, it is now also clear that the singularity of the population inversion threshold is due to the net stimulated emission rate becoming zero at a particular transition wavelength.

As seen in Figs 2.15 – 2.21, the agreement is excellent between the two measurements at the lower biases (< 1 A) for both the population inversion threshold and the calculated values of n_{sp}. However, above 1 A, the agreement becomes significantly worse especially at the higher energies. There appears to be an overall carrier dependent background loss mixed within the intrinsic loss. This added loss inflates the estimated n_{sp} calculated using noise figure measurements giving rise to a difference between the population inversion factors estimated using both methods. It is not possible to explain this loss with two photon absorption arguments as the deviation is present independent of the signal power of the laser. However, one possible explanation is that the loss may be due to increasing effects of free carrier and intervalence band absorption in the active region at high biases. In conventional SOAs, these loss processes may be completely masked by the high intrinsic losses of the devices. As a result, conventional SOAs do not exhibit degradations in noise figure at higher pump currents. This is not true for a SCOWA where the additional losses are on the order of the intrinsic loss. A carrier dependent loss of 1.05 cm^{-1} was used in addition to the 0.5 cm^{-1} intrinsic loss to simulate n_{sp} in Fig. 2-22. The residual differences in calculated n_{sp} values on the short wavelength side are attributed to a wavelength dependent loss mechanism. However, the assumed constant 289 K electron temperature may yet be another variable contributing to these differences since the electron temperature is expected to increase when the bias current increases. Further investigation is needed in order to accurately determine the cause of this population inversion factor deviation.

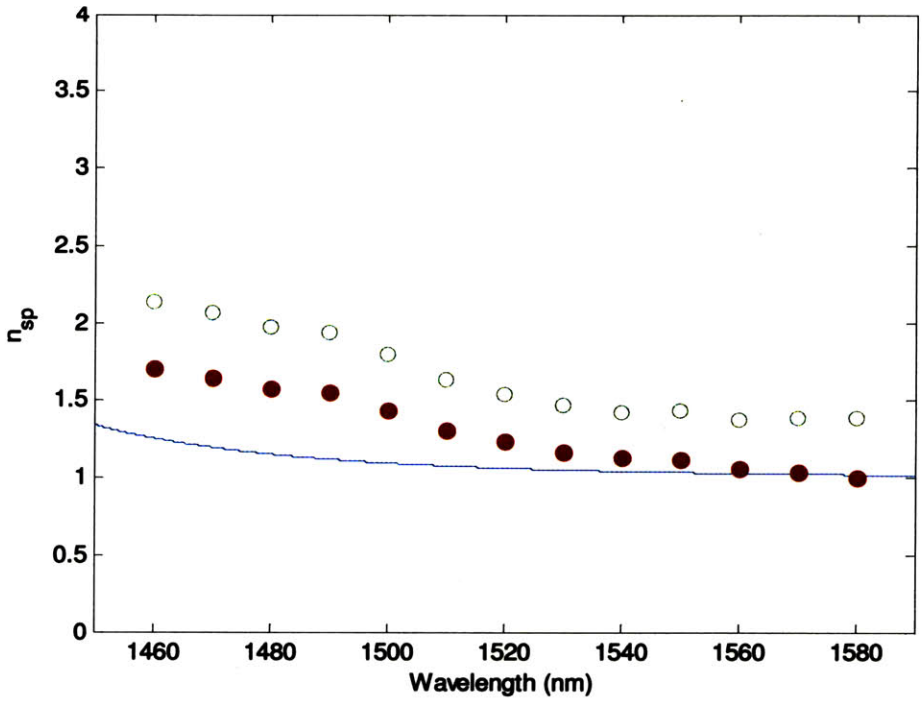

Figure 2-22: Population inversion factor at 5 A calculated using noise figure measurements accounting for (solid circles) and neglecting (open circles) carrier dependent loss effects. The population inversion factor calculated from IV measurements (solid line) is also shown.

2.5 Summary

In this chapter, the measurement results of a packaged slab-coupled optical waveguide amplifier were discussed in detail. Gain saturation, electrical-to-optical conversion efficiency, and gain spectra tests were performed in order to measure the SCOWA signal amplification performance across a wide range of operating conditions. The results indicated Watt class output powers at the telecommunications wavelength (~ 1550 nm) with corresponding gain bandwidths in excess of 100 nm. The theory of the optical amplifier noise figure was also described with emphasis placed on the interpolation source subtraction technique and the electrical technique for noise figure characterization. The steps towards proper calibration of the noise figure measurements were reviewed. Measurements of the SCOWA NF with both optical and electrical methods yielded noise figures of 5.5 dB at 1550 nm and 5 A bias. This noise figure reaches a minimum of ~ 4.5

dB at 2 A current operation. Comparison of the population inversion factors extracted from noise figure measurements with those predicted from I-V measurements yields excellent agreement up to 1 A. Beyond 1 A, additional effects needed to be accounted for in order to explain the n_{sp} inconsistency.

Chapter 3

SCOWECL Measurements

External cavity lasers (ECLs) are useful for coherent optical communication systems requiring narrow linewidth sources. ECLs based on a double-pass SCOWA gain medium are expected to have higher output powers, lower losses, and lower relative intensity noise. With these advantages in mind, we demonstrate the design for the Slab-Coupled Optical Waveguide External Cavity Laser (SCOWECL) to be used as the optical oscillator for an RF front end in a RF receiver link. The SCOWECL is constructed by lens coupling a frequency selective fiber Bragg grating (FBG) to the SCOWA waveguide. Lensed fiber coupling is used to optimize coupling efficiency between the active and passive cavities.

In this chapter, we present measurements of the SCOWECLs characterizing their potential as coherent sources. L-I measurements are performed in order to analyze the efficiency and output power of the laser. Low and high frequency RIN results are taken to analyze the laser's single mode stability and overall intensity noise. Finally, linewidth measurements are performed on the laser by the delayed self-heterodyne method. This chapter presents the theory behind these measurements and also a comparison of the results when parameters of the laser are selectively varied. In particular, the performance characteristics of SCOWECLs fabricated using 10% and 20% reflectivity gratings will be analyzed in detail. These measurements will reveal the extraordinary potential of SCOWECLs as single frequency coherent light sources.

3.1 Use of SCOWECLs in Analog Optical Links

Analog optical links are used for remote distance communication applications where information picked up by a receiving antenna is relayed to the central office via optical fiber. These links have the advantages of very low loss, high bandwidth, and immunity to electromagnetic interference [52]. The receive link consists of a master oscillator laser that is modulated with the information contained in the received RF signal. In Chapter 1, it was mentioned that a SCOWECL is ideal for this application as SCOWECLs are expected to demonstrate high power, low RIN, and narrow linewidth. These attributes are all favorable for obtaining a low noise figure analog optical link. The power gain of an externally phase modulated link can be written as [53]

$$G_{link} = \left[\frac{\beta_{TX}(\omega)}{\beta_{LO}(\omega)} \frac{G(\omega)}{1+G(\omega)} \right]^2 \tag{3.1}$$

where $\beta_{TX}(\omega)$ is the sensitivity of the transmitter phase modulator, $\beta_{LO}(\omega)$ is the sensitivity of the receiver phase modulator, and ω is the frequency. $G(\omega)$ is the photonic phase looked loop (PPLL) open loop gain defined as $G(\omega) = 2\beta_{LO}\Re\sqrt{P_{TX}P_{LO}}R_{term}e^{-j\omega\tau_d}$. Here, $\Re$ is the responsivity of the photodiode, P_{TX} is the optical power of the transmitter, P_{LO} is the optical power of the local oscillator, R_{term} is the terminal resistance, and τ_d is the loop propagation delay. The link noise figure can also be calculated and is given by [53]

$$NF = 10\log\left(\frac{\left\langle I_{phase}^2 + I_{RIN}^2 + I_{SN}^2 + I_{thermal}^2 \right\rangle}{4kT\Re^2 P_{TX}P_{LO}R_{term}\beta_{TX}^2(\omega)} + 2 \right). \tag{3.2}$$

Here, k is Boltzmann's constant, T is the room temperature, I_{phase}^2 is the mean-square phase noise current, I_{RIN}^2 is the mean-square RIN current, I_{SN}^2 is the mean-square shot noise current, and $I_{thermal}^2$ is the mean-square thermal noise current from the photodiode terminal resistance.

The lowest achievable link noise figure is 3 dB. This limit can be reached for a link with low shot noise, RIN, phase noise, and thermal noise. The mean-square RIN and phase noise currents vary with the square of the optical signals. Thus, the power dependence of the noise figure expression corresponding to these terms cancels out. Low intrinsic laser RIN and linewidth is needed in order to prevent these noise sources from degrading link performance. The

thermal noise term does not depend on power, so its noise figure contribution can be made low with high transmitter and local oscillator optical signal strength. The shot noise term increases linearly with the optical signal resulting in an inversely proportional decrease of the noise figure with power. Therefore, a 3 dB noise figure link requires high optical powers, low laser RIN, and narrow linewidth. The SCOWA gain medium is especially suited for this application as it is specifically designed to achieve high power levels and low intensity noise. Furthermore, the gain peak can be engineered according to the operation wavelength to support low α_H and narrow linewidth operation. Thus, the SCOWECL is expected to be well suited to analog optical link applications where noise figure becomes one of the central parameters to optimize.

3.2 SCOWECL Components

The functionality of the SCOWECL is based on the interaction between four essential elements: a double-pass SCOWA gain medium, a narrow-bandwidth fiber Bragg grating (FBG), a lensed fiber, and an optical isolator. The double-pass SCOWA serves as the gain element, while the fiber Bragg grating is used for the selection of a single longitudinal lasing mode within the

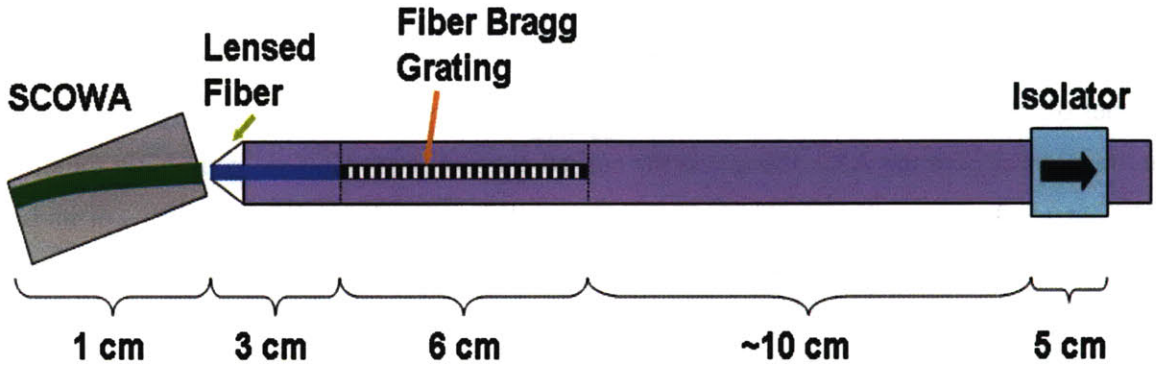

Figure 3-1: Slab-Coupled Optical Waveguide External Cavity Laser Schematic.

cavity. The lensed fiber is used to facilitate coupling between the SCOWA mode and the fiber mode. Lastly, the isolator is used to suppress the effects of back reflections from external optical elements. The schematic of the SCOWECL is shown in Fig. 3-1.

The length scale for each component of the laser is also given in Fig. 3-1. The total length of the laser is seen to be ~25 cm. The laser cavity itself is approximately 7 cm and includes the SCOWA, the lensed fiber, and the fiber Bragg grating. The cavity boundaries were taken to be at the far facet of the SCOWA (away from the lensed fiber) and the midpoint of the FBG. Taking the boundary to be at the middle of the FBG is justified for weakly reflective grating structures such as those used in our SCOWECL measurements. Each component of the laser will be described in detail later in this section.

3.2.1 Double-Pass SCOWA

The double-pass SCOWA has a device length of 1 cm and forms the active cavity of the SCOWECL. The amplifier is designed for low optical confinement (Γ ~ 0.3-0.5 %) to allow for high power operation. The active region of the device consists of four InGaAsP quantum wells bounded by lower index InGaAsP barriers and is grown on top of a 5 μm thick n-InGaAsP waveguide. Ridges of 5.8 μm width were formed by etching through the active region of the device. A double pass through the SCOWA is achieved by antireflection (AR) coating the facet of the SCOWA that is coupled out to the lensed fiber. The AR coating serves the purpose of suppressing back reflections at the facet interface. The other facet is high reflection (HR) coated to prevent the leakage of optical power out of the facet. To further suppress back reflections, the channel of the SCOWA itself is curved to a 5°-angle intersection with the cleaved facet. The combination of both the AR coating and the curved channel results in a reflectivity on the order of 10^{-6} at 1550 nm wavelength. The double-pass amplifier was characterized in terms of its L-I, I-V, gain, and loss characteristics. These measurements are described next.

Double-Pass SCOWA L-I and I-V Characteristic

The L-I and I-V characteristics of the slab-coupled optical waveguide gain medium were measured by monitoring the voltage and power output of the double-pass SCOWA as current was injected into the device. For the L-I measurement, the output light was focused onto the power meter head by means of a low-loss free space lens mounted on a 3-axis translational stage. The results of the L-I and I-V measurements are shown in Figs. 3-2 (a) and (b) respectively.

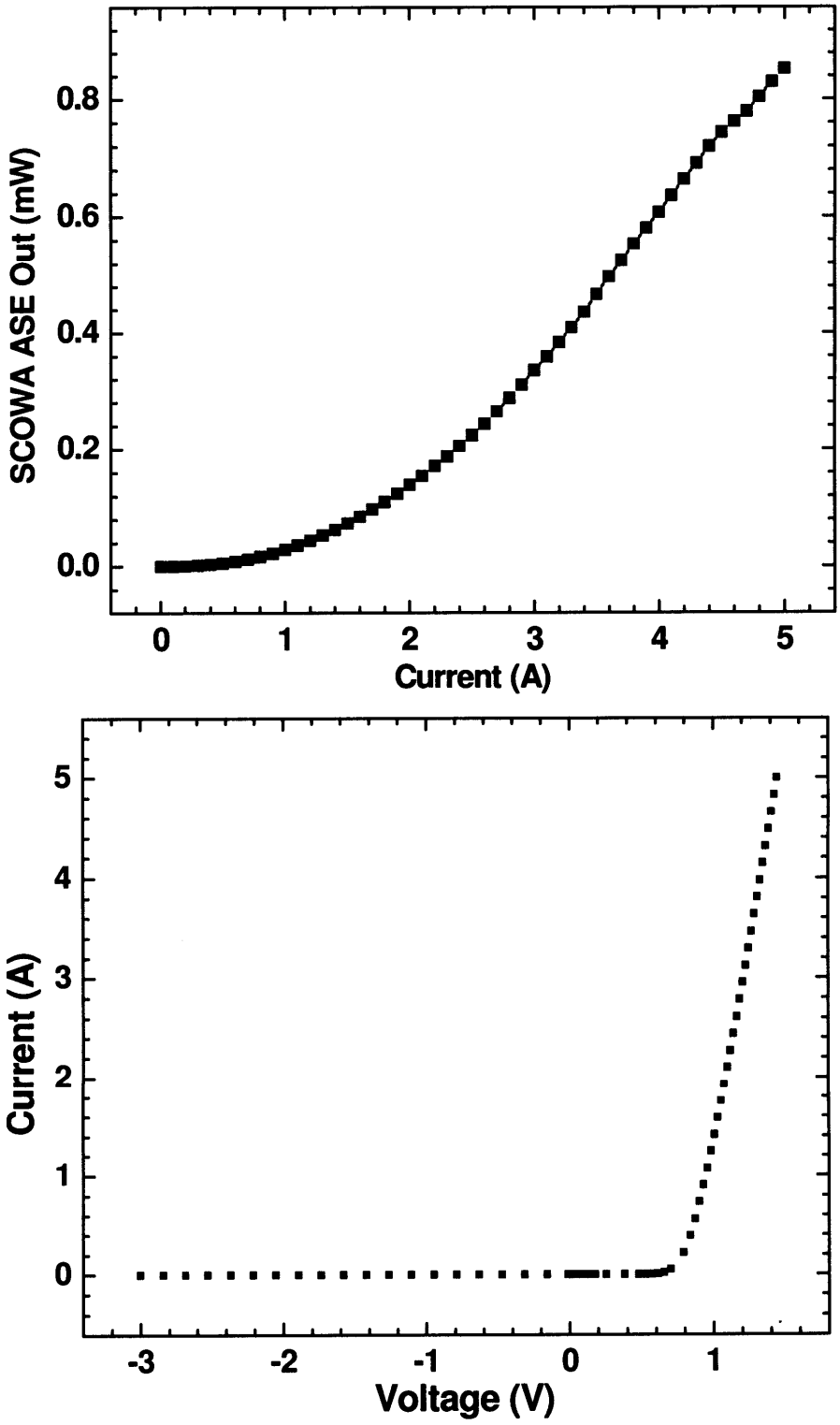

Figure 3-2 (a) and (b): Measured (a) L-I and (b) I-V characteristics of double-pass SCOWA. The TEC temperature was maintained at 16 °C.

From Fig. 3-2 (a), it is seen that the amplified spontaneous emission (ASE) out of the device reaches a peak power of ~ 0.9 mW at 5 A current bias. The low optical powers and the lack of a threshold kink in the L-I curve provides reassurance that the SCOWA gain medium does not self-lase. This is important in order to prevent doubly resonant cavity effects within our external cavity laser. The lack of a lasing threshold for currents as high as 5 A also confirms the low facet reflectivities achieved for the curved channel amplifier.

The slight deviation of the L-I curve at ~4.5 A bias is most likely due to the gradual emergence of thermal effects once higher current levels are reached. For example, thermal processes leading to increased nonradiative recombination can explain the measured decrease in SCOWA ASE at the higher currents. Slight shifts in the coupling due to thermally induced changes in the refractive index may also be a possible cause for the observed shift in L-I characteristics.

The series resistance extracted from the I-V measurement in Fig. 3-2 (b) was determined to be 0.13 Ω. This value is typical compared to previously measured values of series resistance for single pass SCOWA devices. The turn-on voltage of the amplifier was extrapolated to be 0.826 V. The excellent values of series resistance and turn-on voltage are essential to the high performance operation of these amplifiers.

Double-Pass SCOWA Gain Measurement

The double-pass gain through the SCOWA was measured as a function of wavelength and bias current using the setup shown in Fig. 3-3. A continuous wave (CW) tunable laser is sent through the polarization paddles for polarization tuning of the laser output. The resulting signal is sent to port 1 of an optical circulator. The input to port 1 is coupled to port 2 with low loss but is strongly attenuated (> 30 dB) when coupling to port 3. The output of port 2 is lensed fiber coupled to the double-pass amplifier, which results in an amplified signal sent back into port 2. Port 2 now couples to port 3 with low loss and receives significant attenuation (> 30 dB) coupling to port 1. The output of port 3 is sent to an optical power meter for measurement of the amplified power as a function of the laser tuning wavelength and SOA bias. The circulator losses

must be properly calibrated in order to accurately determine the SCOWA's gain characteristics. Table 3-1 summarizes the circulator loss calibration for ports 1 and 2.

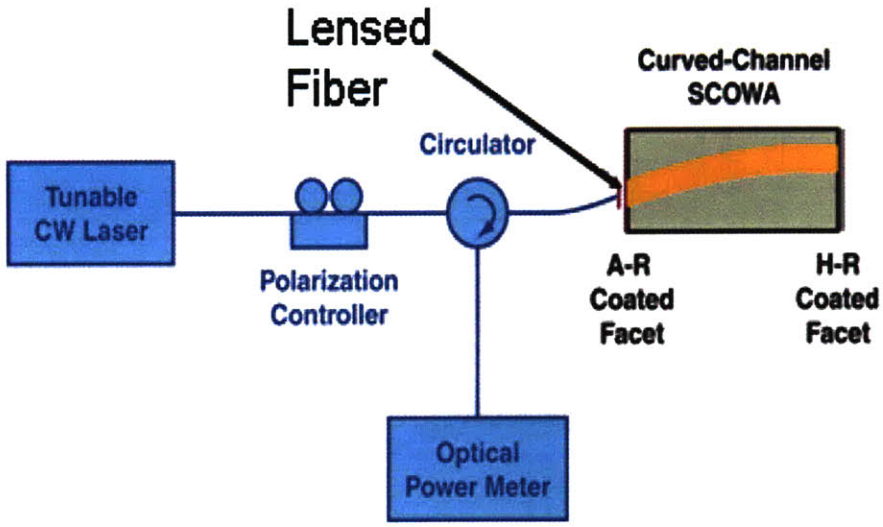

Figure 3-3: Measurement setup for the gain characteristics of the double-pass SCOWA

Port Loss	Output Port 1	Output Port 2	Output Port 3
Input Port 1	—	1.36 dB	> 30 dB
Input Port 2	> 30 dB	—	2.12 dB

Table 3-1: Circulator loss calibration for ports 1 and 2.

Table 3-1 shows that a total loss of 3.48 dB must be accounted for in the measurement of the SCOWA gain characteristics. The extinction ratios are measured to be greater than 30 dB for both propagation along 1-to-3 and 2-to-1. This ensures that the laser signal in port 1 will not significantly affect the measurement results of port 3. Furthermore, this also prevents the amplified signal entering port 2 from interfering with the laser signal at port 1. The results of the SCOWA gain characteristics measurement are shown in Fig. 3-4.

As seen in the figure, the gain of the SCOWA at 1550 nm is ~12.8 dB at 1 A bias but reaches ~23 dB at 4 A bias. The amplifier gain at 1 A is of particular importance since the SCOWECL operates with a threshold current of ~1 A at 1550 nm, as will be shown in detail

later. According to the 1 A gain curve, the laser is seen to operate on the blue side of the gain spectrum peak. This has the effect of reducing the linewidth enhancement factor (α_H), thereby reducing the total linewidth of the laser and increasing sidemode suppression [54, 55].

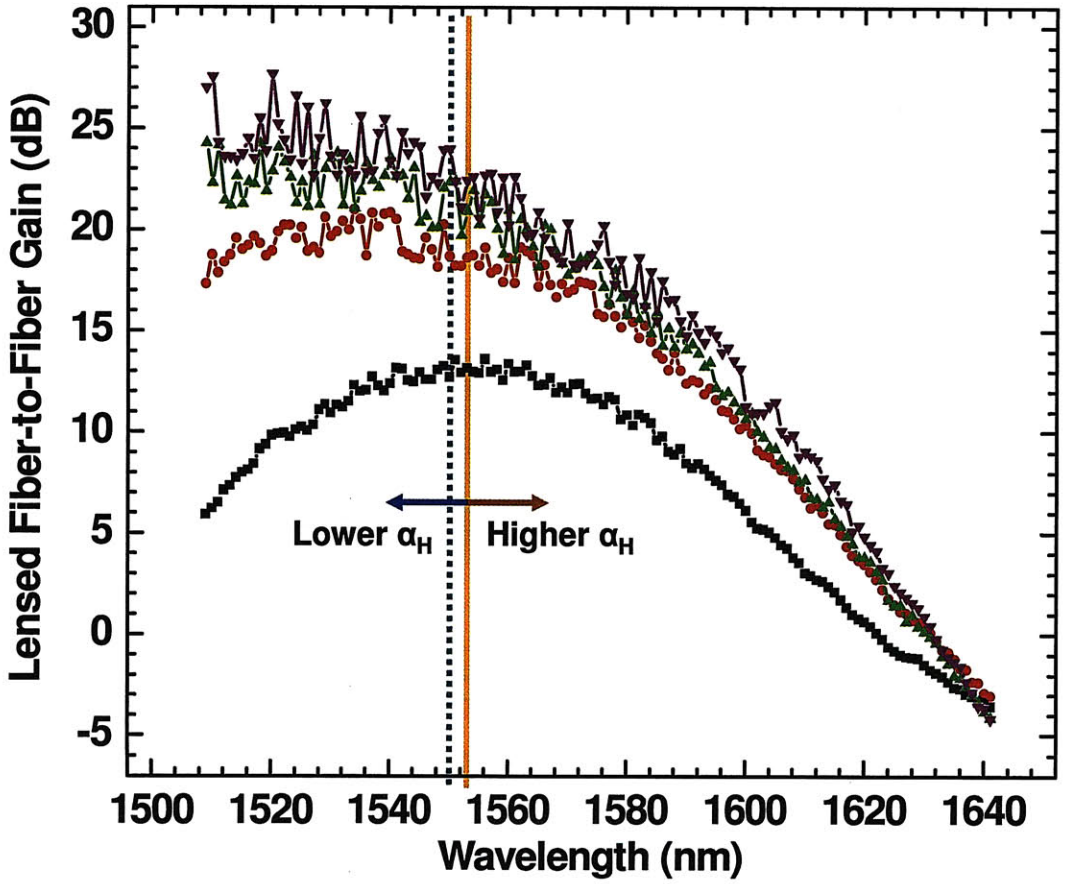

Figure 3-4: Double-pass SCOWA gain characteristics as a function of current and wavelength. The gain curves for 1 A (squares), 2 A (diamonds), 3 A (upright triangles), and 4 A (inverted triangles) are shown. The gain peak wavelength (solid line) and operating wavelength (dashed line) are also illustrated.

In Fig. 3-4, ripples emerge in the gain spectra wherever the gain of the amplifier becomes large. Furthermore, the amplitude of the ripples increases as the gain increases to larger values. At first glance, the ripples appear to resemble the interference pattern expected in the output spectrum of a low-Q Fabry-Perot resonator. Such a resonator may be formed if a small but non-negligible reflection exists at the semiconductor facet interfaces. However, the ripples do not appear to be

due to Fabry-Perot fringe effects as the oscillations occur at a faster rate than the free spectral range spacing. This is illustrated further in Fig. 3-5.

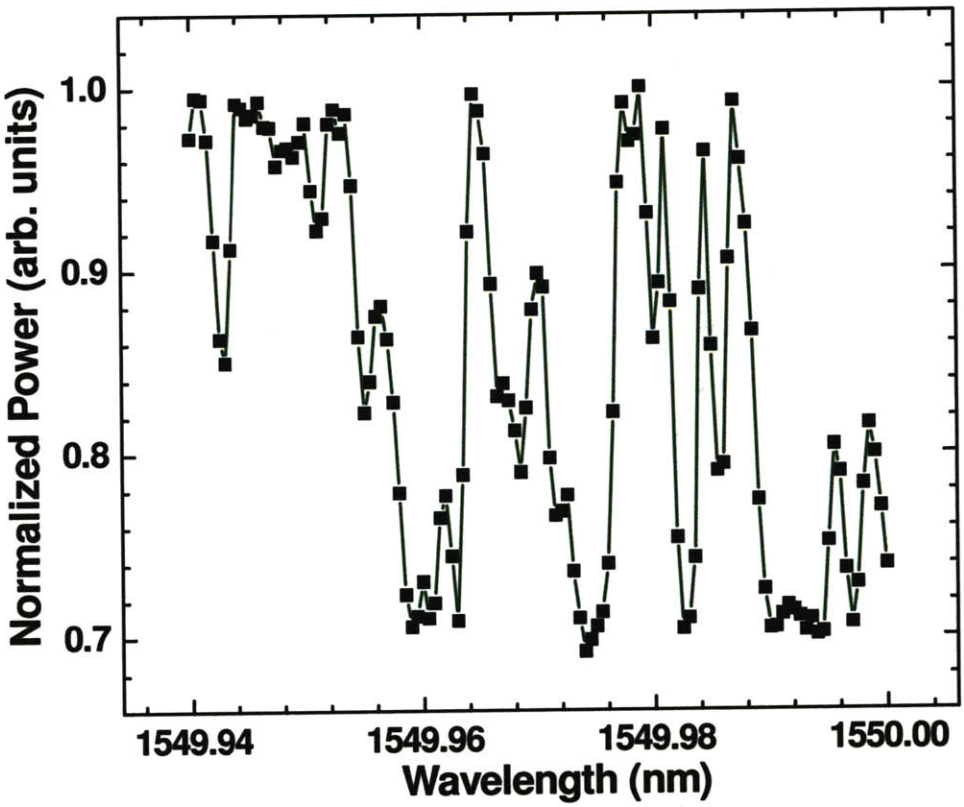

Figure 3-5: High-resolution spectrum for the amplified power out of the double-pass SCOWA.

Fig. 3-5 shows the normalized power out of the double-pass SCOWA as a function of the tunable laser wavelength. The setup used for this measurement was the same as that of Fig. 3-3 except that the tunable laser wavelength scan was performed under a much higher resolution setting. In our tests, the laser was swept between the wavelengths of 1549.94 nm and 1550 nm in increments of 0.5 pm. The amplified output power out of the SCOWA was recorded but was not normalized with respect to the input power. The reason for this is because only the periodicity of oscillations is important for verifying the origin of the observed oscillations.

Theoretically, the ripples in the gain spectra should be spaced apart by the free spectral range if they were caused by Fabry-Perot interference effects. The free spectral range can be mathematically calculated using

$$FSR = \frac{c}{2nl} \tag{3.3}$$

where c is the speed of light, n is the group index at which the mode propagates, and l is the length of the resonator. For a SCOWA device, the FSR is ≈ 4.30 GHz. This corresponds to a wavelength spacing of 34.4 pm. It is clear from Fig. 3-5 that the oscillations occur on a faster scale than the theoretical mode spacing of the Fabry-Perot resonator. Finer resolution wavelength sweeps (0.1 pm) have even confirmed ripple effects below the picometer wavelength scale. However, the peaks of the ripples do not appear to follow an underlying periodicity in any of the performed measurements.

One possible explanation for the occurrence of these oscillations is that the circulator extinction ratio between ports is not high enough to prevent the amplified signal entering port 2 from significantly affecting laser operation at port 1. The circulator extinction ratio was measured to be only slightly above 30 dB as seen from Table 3-1. However, the double-pass gain of the SCOWA graphed in Fig. 3-4 reaches levels close to ~25 dB. Therefore, under large gains, the return signal of port 1 is on the order of the signal emitted by the laser. This return signal can couple into the laser cavity and interfere with the established optical field of the cavity. Two resonant optical cavities are created this way with the second cavity spanning across the tunable laser, ports 1 and 2 of the circulator, and the SCOWA device. The length of this second cavity is long yielding a very narrow FSR. The sub-picometer oscillations in the gain spectra observed when the gain levels are high may be due to the supposition of the signals output from both cavities.

Based on the previous discussion, the ripples present in the gain spectra are expected to make little impact on the operation of the assembled external cavity laser. The theory of two resonant cavities is specific to the use of a circulator in the measurement of the gain characteristics. Furthermore, even if the ripples were intrinsic to the double-pass SCOWA, the lasing threshold of the SCOWECL was already mentioned to be 1 A. Once the laser reaches threshold, the gain characteristics are clamped. As seen from Fig. 3-4, the 1 A gain curve is

almost completely free from gain spectra oscillations. As a result, we do not expect any performance degradation to occur due to the double-pass SCOWA gain medium.

Double-Pass SCOWA Loss Measurement

Cutback measurements were performed on Slab-Coupled Optical Waveguide Lasers (SCOWLs) fabricated from the same material as the double-pass SCOWA in order to estimate the intrinsic loss of the SCOW gain medium. In this measurement technique, the L-I characteristics of the SCOWL are recorded as successive lengths of the laser are cleaved off. The variation in the L-I curves as a function of the device length can be used to determine the internal loss and injection efficiency of SCOW based devices. The theory for the cutback measurement technique is based on the linear relationship between output power and current when the laser is operated above threshold. This L-I relation is widely known for semiconductor lasers and is given by

$$P = \eta_i \frac{h\upsilon}{q} \frac{\alpha_m}{\alpha_m + \alpha_i} (I - I_{th}) \tag{3.4}$$

where η_i is the injection efficiency, υ is the optical frequency, I is the current bias, I_{th} is the threshold current, and α_i is the internal loss. α_m is the mirror loss and can be found from

$$\alpha_m = \frac{1}{2l} \ln\left(\frac{1}{R_1 R_2}\right). \tag{3.5}$$

Here l is the device length and R_1 and R_2 are the reflectivities of the two facets of the laser. Using Eq. (3-5), the reciprocal of the slope to the L-I relation in Eq. (3-4) can be found to be

$$\frac{1}{S} = \frac{1}{\eta_i} \frac{q}{h\upsilon} \frac{2l\alpha_i}{\ln(1/R_1 R_2)} + \frac{1}{\eta_i} \frac{q}{h\upsilon}. \tag{3.6}$$

From Eq. (3-6), it is apparent that a plot of the inverse L-I slope as a function of the device length yields the injection efficiency when the length is extrapolated to zero. Furthermore, the slope of the plot yields the internal losses if the other device parameters are known beforehand. Fig. 3-6 illustrates the setup used to perform the cutback measurements, while Fig. 3-7 shows the

results for the internal loss and injection efficiency after applying the technique on five separate SCOWL lasers.

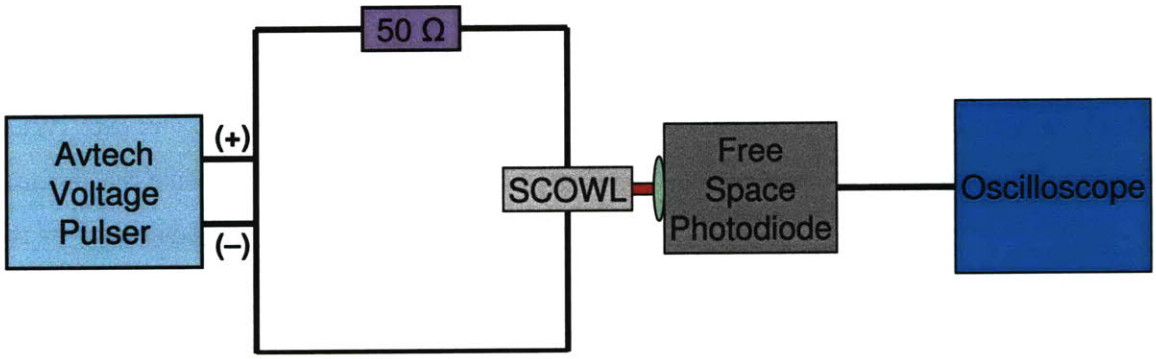

Figure 3-6: Test Setup for Cutback Measurements

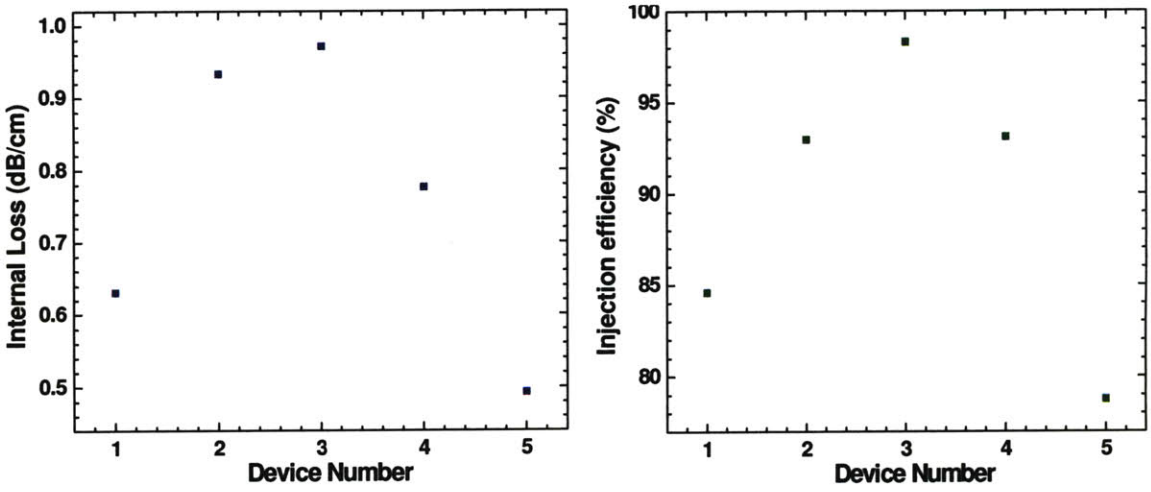

(a) (b)

Figure 3-7 (a) and (b): Measured (a) internal loss and (b) injection efficiency determined from cutback measurements performed on five samples of SCOWL lasers.

The setup, as shown by Fig. 3-6, consists of a voltage pulser, a bias resistor, a photodiode, an oscilloscope, and a SCOWL device. The SCOWLs were operated pulsed in order to prevent thermal effects from corrupting measured data. The 50 Ω resistor sets the bias for the SCOWL by transforming the voltage pulse signal into a current signal. The current pulse is injected into the laser, and a free-space photodetector is used to detect the optical output. The resulting

photocurrent is sent into an oscilloscope in order to measure the laser power as a function of SCOWL bias current.

The cutback measurements were performed on each of the five lasers by measuring the L-I characteristics across a range of device lengths. Device lengths ranging from 1.2 cm to 0.5 cm were tested by successively cleaving each laser back in 0.1 cm steps. Deviations in the L-I slope were observed below device lengths of 0.8 cm, which we attribute to the emergence of multiple transverse mode effects. The SCOWA's coupled mode filtering becomes weaker as the device length decreases since the contrast between the gain of fundamental and higher order modes decreases. The cutback measurement results for device lengths of 0.8 cm – 1.2 cm were used to determine the internal losses and injection efficiencies graphed in Fig. 3-7. The device facet reflectivity required for the calculation of mirror loss was estimated to be 28% with a corresponding index of refractive of 3.25.

As seen in Fig. 3-7, the average internal loss across the five laser samples tested was 0.76 cm^{-1}, and the average injection efficiency was 89.5 %. The internal losses are slightly higher than the expected 0.5 cm^{-1} but are still reasonable given device variations between different fabrication runs. The injection efficiency of ~90% is in good agreement with previously measured efficiency values in the SCOW gain medium. The combination of low loss and high injection efficiency is critically important for compensating the low modal gain of SCOW devices.

3.2.2 Fiber Bragg Grating

The fiber Bragg grating serves as the wavelength selective element in the SCOWECL cavity. In general, a laser has many different longitudinal modes spaced by the cavity's free spectral range (FSR). By extension of Eq. (3.3), the FSR for a resonator with both an active and a passive cavity can be found to be

$$FSR = \frac{c}{2(n_a l_a + n_p l_p)} \tag{3.7}$$

where c is the speed of light, n_a is the active material group index, l_a is the active cavity length, n_p is the passive material group index, and l_p is the passive cavity length. In order to ensure that only a single mode is resonant within the cavity, the bandwidth of the FBG's reflectivity spectrum should theoretically be narrower than the free spectral range. However, because of nonlinear mode suppression, this condition for single mode stability is relaxed in practice [56]. Because the SCOWA itself is long and has a group index of $n_a = 3.49$, the FBG bandwidth should be made as narrow as possible. To achieve a narrow grating bandwidth, a long FBG must be used. However, since the fiber Bragg grating is also part of the laser cavity, a long grating leads to a reduction in the longitudinal mode spacing.

The FBGs employed in our SCOWECL lasers had reflectivities of either 10% or 20% with bandwidths of ~ 20 pm. The reflectivity spectra of the fiber Bragg gratings were measured with a suitable wavelength sweep across the reflection bandwidth. The losses in the grating were determined in a similar manner by measuring the optical transmission at the output of the FBG. The gratings tested were nominally 6 cm long as specified by the edges of the photomask. However, in actuality, the grating reflectivity is nonzero even past the 6 cm mask boundary. Reflectometer measurements were performed to precisely determine the positions along the fiber where the FBGs began and ended. The gratings were also tested in terms of the tunability of their characteristic Bragg reflection wavelength. This wavelength tuning was achieved by stretching the fiber uniformly across the length of the FBG. The results of these measurements are described next.

Fiber Bragg Grating Reflectivity Spectrum Measurements

The characteristics of the fiber Bragg gratings were verified by measuring the reflectivity spectra of the gratings. This allows for the determination of the FBG reflectivity and reflection bandwidth, both of which are critical for high performance single-mode laser operation. The measurement setup is similar to that shown in Fig. 3-3 except that the SCOWA and lensed fiber in port 2 are replaced by the FBG under test. A tunable CW laser is sent through port 1 of the circulator and is directed to port 2 with low loss. The signal in port 2 couples to the grating, and the reflected signal from this interaction is redirected to port 3. Once the optical losses in the circulator are calibrated, the measurement of the reflected power at port 3 can be used to

determine the grating reflectivity spectrum. The results of this measurement performed on a 20% FBG are shown in Fig. 3-8.

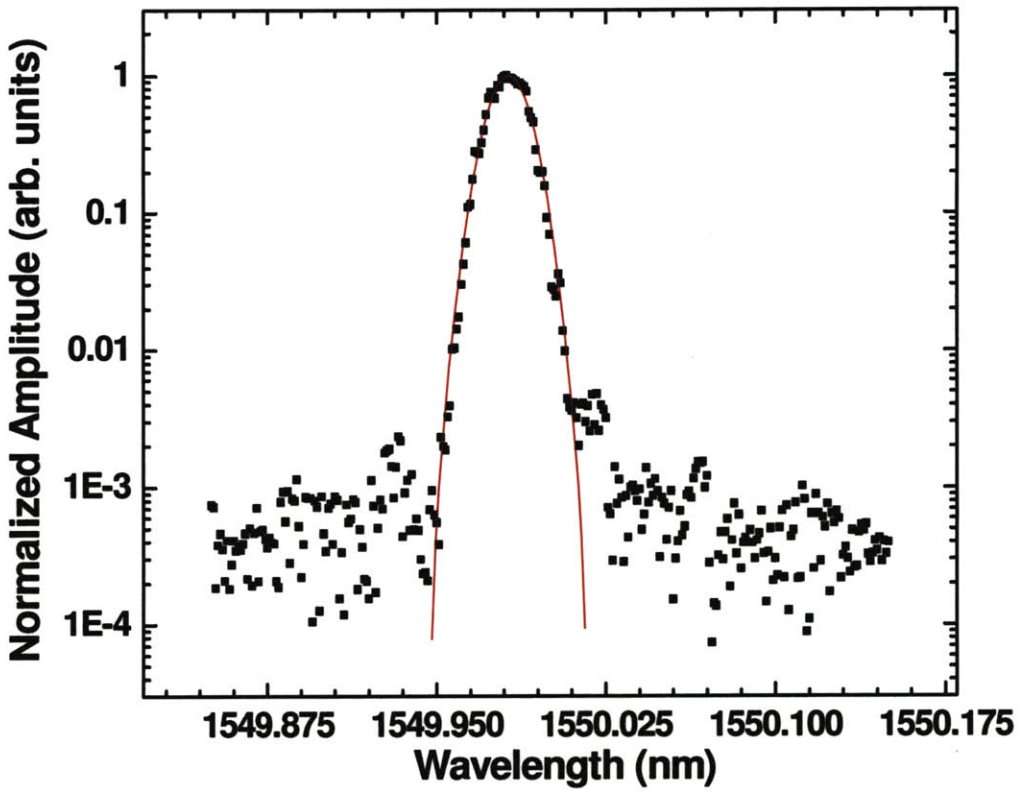

Figure 3-8: Normalized reflectivity spectrum of 20% FBG. The reflectivity was measured to be 22.4 %, and best fit Gaussian curve to the measurement yields a full-width-half-maximum of 19.9 pm.

The reflectivity of the FBG was measured to be 22.7 % after the circulator losses were accounted for. There is a ~ 0.5 dB error between the specified and measured reflectivity, which may be partly due to the losses acquired through fiber connections. This error in peak reflectivity is acceptable from the standpoint of demonstrating SCOWECL functionality since the reflectivity does not need to be very precise for the laser to perform well. The best fit curve to the reflectivity spectrum yields a Gaussian with a full width half maximum (FWHM) of 19.9 pm. This is in contrast to the manufacturer FWHM specification of 25 pm for the grating. However, in this case, the error works to our favor as a lower grating bandwidth is desirable for the suppression of higher order side modes. Finally, the center wavelength of the grating was measured to be

1549.98 nm, which is in excellent agreement with the specified 1550 nm Bragg reflection resonance.

Fiber Bragg Grating Loss Measurements

The losses of the fiber Bragg gratings were measured in order to determine the impact of the losses on the performance of the assembled laser. The losses were determined by sending the output of a tunable CW laser into a FBG and recording the transmitted power on an optical power meter. The ratio of the transmitted power to incident power extrapolated at the Bragg reflection wavelength yields the loss of the grating. Fig. 3-9 illustrates the results obtained from the loss measurement performed on a 5% fiber Bragg grating. Note that the 5%, 10%, and 20% gratings are all identical except for the grating reflectivity. Therefore, we expect that the loss measured here to be equally applicable for any FBG we decide to use in our SCOWECL design.

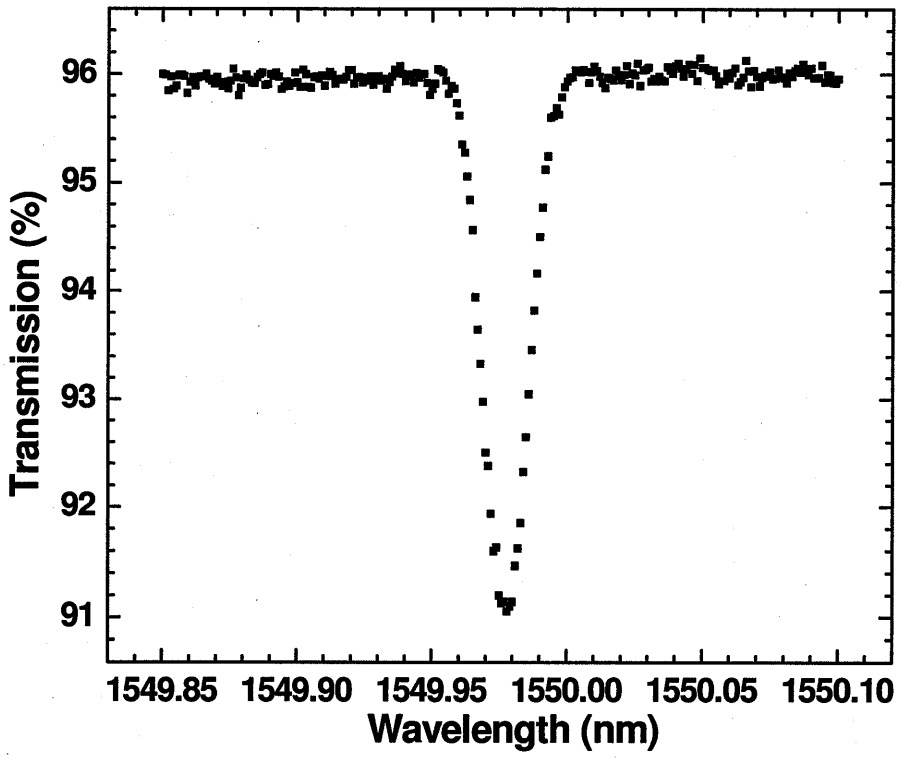

Figure 3-9: Plot of FBG transmission as a function of wavelength for a 5 % reflectivity FBG. The transmission at the peak reflection wavelength is extrapolated to be 96%.

Fig. 3-9 shows that there is a 4% (0.18 dB) transmission loss after passage through the fiber Bragg grating. The measured loss is low, so we expect grating losses to have only a small impact on overall laser performance.

Fiber Bragg Grating Reflectometer Measurements

It was mentioned in the introduction to this section that the FBG reflection bandwidth should theoretically be narrower than the FSR of the longitudinal modes in the cavity in order to establish single mode operation. It is therefore important to exclude all unnecessary fiber from contributing to the external laser cavity. An optical backscatter reflectometer (OBR) was used to pinpoint the exact starting and ending locations of the fiber Bragg grating within the housing SMF fiber. The OBR measures the optical signal reflection as a function of distance along the optical fiber. Reflectometer measurements performed on a 20% reflectivity grating are shown in Figs. 3-10 (a) and (b).

The cursors in Fig. 3-10 (a) highlight the alignment marks of the photomask used in the production of the fiber Bragg grating. The measured cursor spacing of ~6 cm indicates the nominal length of the FBGs that were tested in our laser cavity. Fig. 3-10 (b) shows that the currently tested 20% grating has an additional length of ~1 cm that extends beyond both sides of the mask. However, the reflection strength of the FBG past the mask boundaries is over 20 dB below that of the peak. In our SCOWECL design, we excluded the additional grating length beyond the mask in order to minimize the length of the optical cavity. The grating was spliced to a lensed fiber such that the splice junction occurred right at the location of the mask boundary. The precise location of the grating was determined in reference to the cleaved end of the SMF fiber housing the FBG. This cleave appears as a reflection peak as seen in Figs. 3-10 (a) and (b). Note that only one end of the grating was cleaved short. The other end lies outside the resonator of the assembled laser and does not therefore affect the cavity free spectral range.

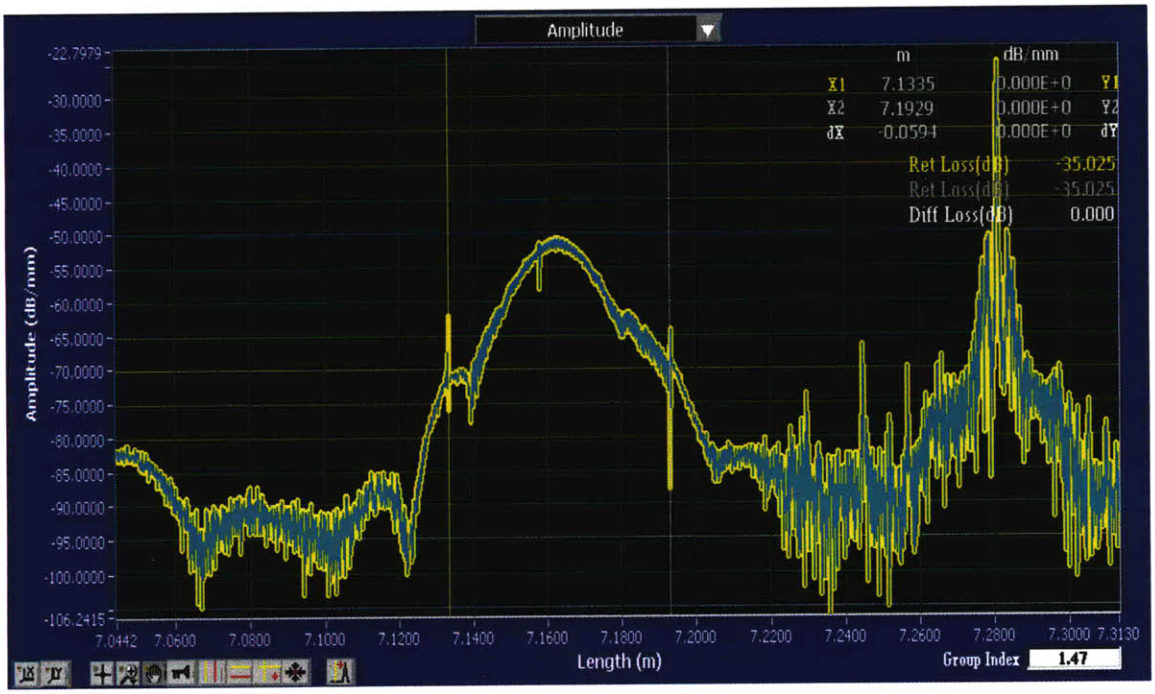

(a)

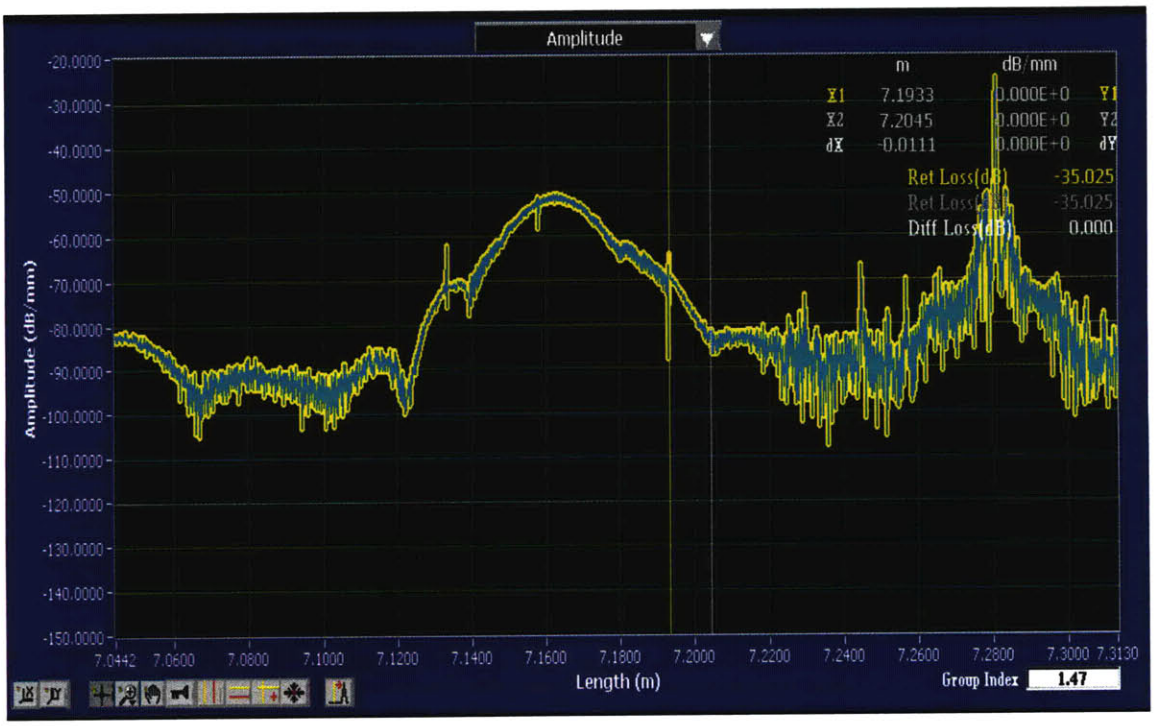

(b)

Figures 3-10 (a) and (b): Illustration of (a) optical backscatter reflectometer measurement of a 20% reflectivity FBG and (b) residual grating length beyond photomask.

Fiber Bragg Grating Wavelength Tuning Measurements

Fiber Bragg grating tuning is important for allowing laser operation across multiple wavelength regimes. Here, we explore the wavelength tuning capabilities of our SCOWECL by stretch-tuning the FBG resonance. Because the Bragg reflection wavelength depends on the periodicity of the index modulation through

$$\lambda_B = 2n\Lambda, \tag{3.8}$$

a uniform axial stretch across the length of the grating results in a shift of λ_B towards longer wavelengths. In Eq. (3.8), n is the refractive index of the fiber, and Λ is the spatial period of the grating.

The fiber stretching was accomplished by mounting the grating on a piezo-electric transducer. Application of a voltage between 0 V -1000 V resulted in a stretching of up to 120 μm. Assume that the 120 μm length is uniformly distributed across the length of the piezo actuator (10.6 cm), a 6 cm long FBG will only experience a 68 μm stretch. Thus, each grating period will be extended by 0.585 nm resulting in a maximum overall Bragg resonance shift of 1.75 nm. This estimate assumes ideal conditions with a uniform stretch across the length of the grating. For comparison purposes, the results of FBG tuning measurements performed on a 5 % reflectivity grating are shown in Fig. 3-11.

The setup is the same as that used previously in the FBG reflectivity spectra measurements except for the addition of a 5000 V source used to bias the piezo stretcher. The FBG was held to the piezo actuator through epoxy applied to the ends of the grating. Ideally, the polymer coating over the FBGs should be removed so that the coating does not shear and result in nonuniformity or severe reductions in stretch length. However, the coating protects the core from damage that would otherwise occur during testing and packaging, so it is highly desirable not to strip off the protective polymer layer.

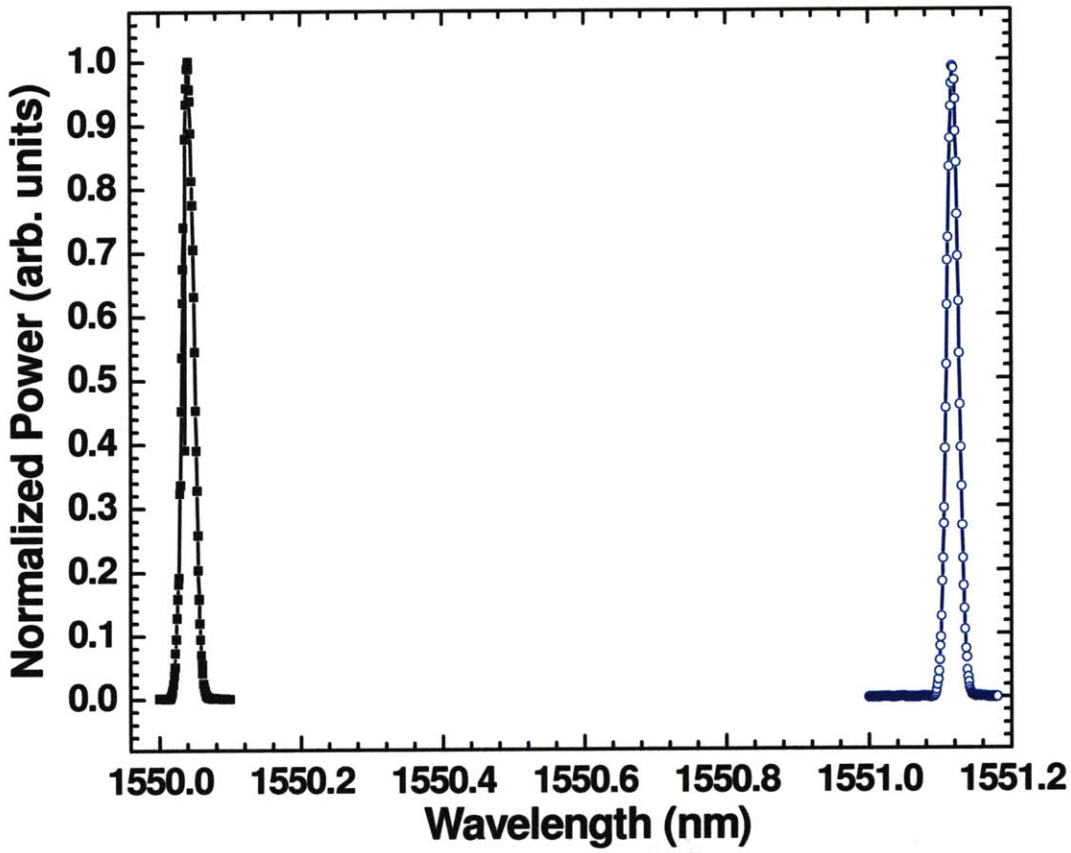

Figure 3-11: Plot of the FBG tuning measurement performed on 5 % grating. The reflectivity spectrum with zero applied voltage (solid squares) and 1000 V applied (open circles) is illustrated. The wavelength shift of the spectrum peak is 1.08 nm. Only the ends of the FBG were epoxied down onto the piezo actuator.

Fig. 3-11 shows the tuning capabilities of the fiber Bragg grating with the polymer coating still attached. With application of 1000 V to the piezo stretcher, the resulting FBG resonance shifted from a wavelength of 1550.04 nm to 1551.12 nm yielding a wavelength tuning of 1.08 nm. This is ~60 % of the predicted shift in Bragg resonance based on theoretical calculations. Clearly, the shear of the polymer coating plays a significant role in hindering the stretching capacity of the fiber. In an attempt to achieve a larger tuning range, another measurement was performed but with the entire length of FBG epoxied to the piezo actuator. This has the effect of pulling the grating along its entire length instead of only along its two ends. The results of this experiment performed on the same 5 % FBG are illustrated in Fig. 3-12.

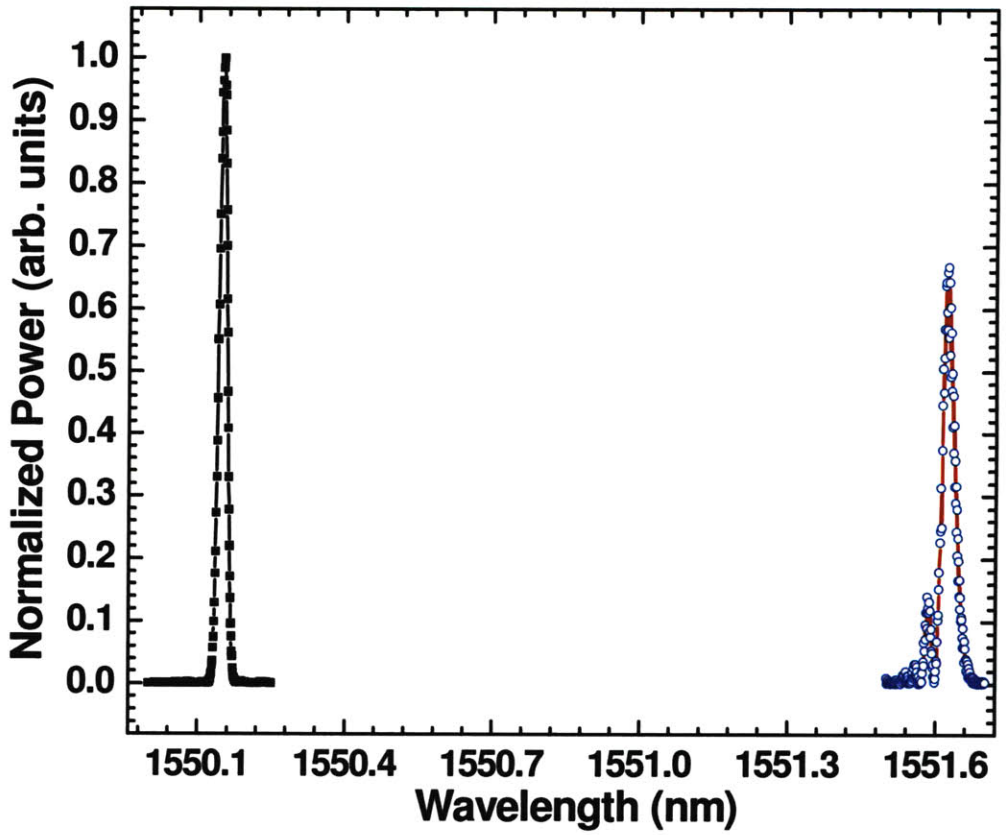

Figure 3-12: Graph of FBG tuning measurement with the entire grating length epoxied down onto the piezo actuator. The reflectivity spectrum with zero applied voltage (solid squares) and 1000 V applied (open circles) is illustrated.

The measured wavelength changed from 1550.15 nm to 1551.62 nm with the application of 1000 V of bias. This yields a wavelength tuning of 1.47 nm, which is 84 % of the calculated theoretical Bragg resonance shift. However, the increased wavelength tuning comes at a price of reduced reflectivity as the reflection peak is now ~67 % of its original value. Furthermore, as seen from Fig. 3-12, there is also an added irregularity resulting in the appearance of a secondary reflection resonance. These effects are due to a nonunfiorm stretching of the grating across the length of the fiber. During the epoxy process, the FBG was not tautly glued to the piezo actuator. The FBG is tautly epoxied onto the stretcher across the entire length of the grating in our final SCOWECL design in order to avoid these abnormalities during tuning.

In our measurements of FBG wavelength tuning, the hysteresis of the piezo actuator was also measured. Typical piezo stretchers exhibit a small degree of hysteresis since the length of

the piezo material does not relax back to its initial state until long after the bias has been removed. This results in a slight red shift of the Bragg resonance after each voltage sweep. The effect of hysteresis on our FBG was tested by recording the 0 V reflectivity spectrum after successive voltage sweeps to and from 1000 V. The initial spectrum along with the results after the first and second voltage ramps are shown in Fig. 3-13.

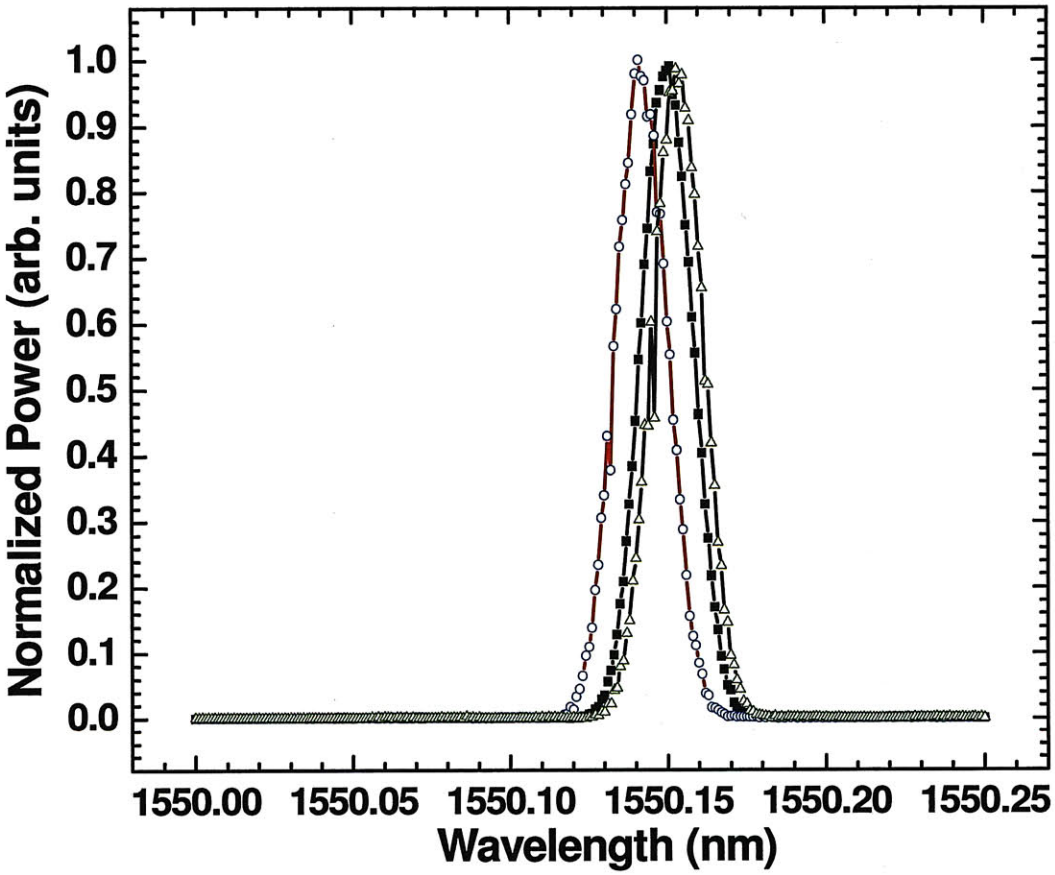

Figure 3-13: Measurement of piezo actuator hysteresis effect. The initial FBG reflectivity spectrum (solid squares), spectrum after one voltage ramp (open circles), and spectrum after two voltages ramps (open triangles) are illustrated.

It is seen from Fig. 3-13 that the spectrum recorded after the first voltage sweep is unexpectedly blue-shifted compared to the initial spectrum. This can occur if parts of the grating were inadvertently stretched during the epoxy process. The initial voltage sweep caused these nonuniformities to slightly relax, resulting in a blue-shifted zero bias Bragg resonance. A

comparison of Figs. 3-12 and 3-13 shows that the measured initial reflectivity spectra exhibit different center wavelengths. The resonance wavelength when the entire length of the FBG was epoxied down was higher compared to the case when only the ends of the FBG were epoxied. This provides further evidence that nonuniformities in the grating were introduced during the epoxy process. The reflectivity spectrum taken after the second voltage sweep is shifted towards the red as compared to the other two measurements, which is in good agreement with our expectations. The wavelength shift has only a minor impact as the reflection peak is seen to change by < 0.02 nm between the trials.

3.2.3 Lensed Fiber

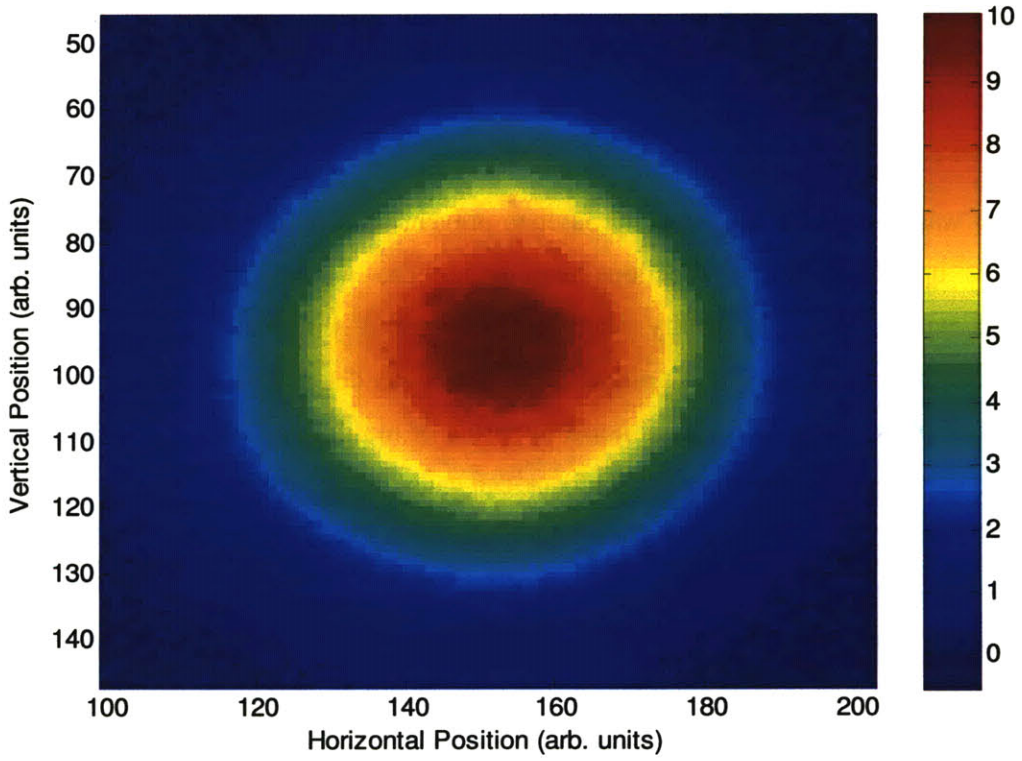

Figure 3-14: Mode field profile of lensed fiber mode.

Lensed fibers were used in order to facilitate coupling of the SCOWA and the fiber Bragg grating. The lensed fibers have a spot size of ~6.5 μm which allows for efficient coupling to the

5.5 μm X 7.5 μm SCOWA mode. The 25 μm working distance of the lensed fibers allows for easy alignment between the fiber and the device with little risk of accidentally damaging the device. The lensed fibers were cleaved to be 3 cm long and spliced onto the ends of the fiber Bragg grating as mentioned previously. The length of 3 cm was determined to be the minimum fiber length required for a repeatable splice.

In order to achieve good coupling, the mode field diameter of the SCOWA and lensed fiber modes should be well matched. The lensed fiber spot was measured by injecting light from a CW laser into the fiber and focusing the resulting output onto an infrared (IR) camera. The measured mode profile is illustrated in Fig. 3-14. The regions of high optical intensity are red as indicated by the colorbar. The $1/e^2$ mode field diameter of this mode was measured to be 7.0 μm in the horizontal direction and 6.9 μm in the vertical direction. The excellent match to the 5.5 μm X 7.5 μm SCOWA mode allows for efficient coupling between the SCOWA and lensed fiber.

3.2.4 Isolator

An isolator was used at the output of the laser to prevent back reflections from interfering with SCOWECL operation. Back reflections can disrupt the natural standing wave resonance established within the laser cavity leading to increased jitter and degradations in RIN performance. In particular, the noise properties of lasers can deteriorate rapidly as a result of the conversion of phase noise to intensity noise by virtue of multiple reflection interference effects [57]. In the worst cases, severe optical feedback can cause instability rendering lasers to become unusable. Polarization insensitive isolators with high return losses are needed in order to prevent back reflections from affecting laser performance.

The isolator used in our SCOWECL was spliced onto the output side of the fiber Bragg gratings with a distance of ~10 cm between the edge of the grating mask and the isolator. The propagation loss of the isolator was measured by sending a CW optical signal from a tunable laser into the isolator. The output of the isolator was monitored by an optical power meter. The ratio of the output and input measured powers yielded the isolator transmission efficiency. The transmissions in both the forward and backward propagating directions were measured by reversing the orientation of the isolator relative to the laser input signal. The measured results indicated an isolator forward propagation transmission of 87.3 % and a backward propagation

efficiency of < 0.0001 % (> 60 dB propagation loss). The large extinction ratio between forward and backward propagation along the isolator allows for stable single mode laser operation to be achieved.

3.3 Impact of Fiber Bragg Grating Reflectivity

In the implementation of the SCOWECL design, SCOWECLs incorporating FBGs with reflectivities of 10 % and 20 % were tested. The SCOWA amplifier was kept the same for both cavities. The lensed fibers and isolators could not be reused between the 10 % and 20 % trials, so lensed fibers and isolators of the same model were used in each case. Finally, the 10 % and 20 % FBGs that were utilized had similar center wavelengths of 1550 nm and grating bandwidths of ~20 pm and differed only in their peak reflectivity. This uniformity between components allows direct comparisons to be made based on the results of the laser measurements. The SCOWECL was tested on a bench-top environment and stabilized with a 16 °C thermoelectric (TE) cooler. The laser was mounted on foam blocks and encapsulated by a plexiglass box in order to damp out external thermal and vibrational noise. This section describes the L-I, RIN, and linewidth techniques and measurements performed on the laser. We will show that the SCOWECL demonstrates phenomenal laser characteristics exhibiting stable single-mode behavior with low RIN, narrow linewidth, and high output power.

3.3.1 SCOWECL L-I Measurements

The SCOWECL L-I measurement setup is exactly the same as that for the Er-doped fiber external cavity laser case. The laser output power is recorded as the current is ramped to 5 A. Here, the L-I comparisons between the 10 % and 20 % gratings are discussed. Comparisons of the butt and lensed fiber L-Is are also described in order to assess the coupling efficiency improvement gained by using lensed fibers. Finally, the extracted electrical-to-optical conversion efficiency is detailed using measurements taken from the SCOWECL L-I and I-V.

10 % and 20 % L-I Measurements

The L-I measurement results are provided in Figs. 3-15 for both the 10 % and 20 % FBG reflectivity cases.

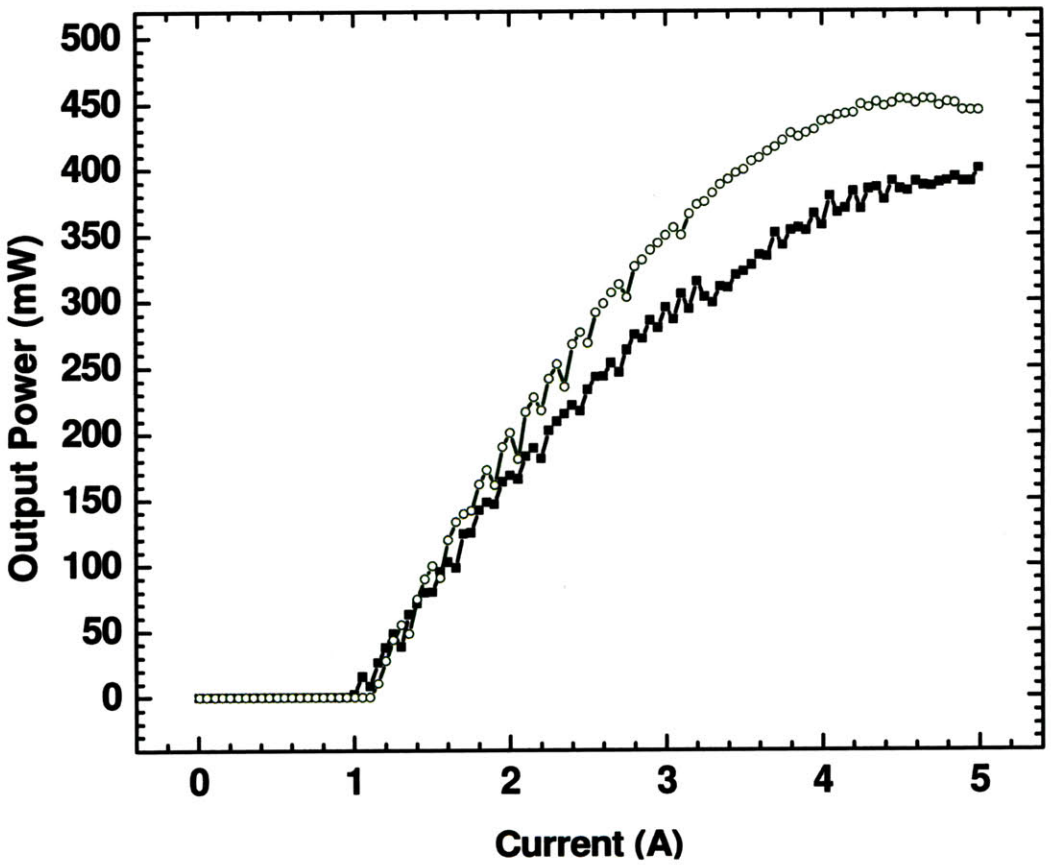

Figure 3-15: L-I curves for 10 % (open circles) and 20 % (solid squares) reflectivity fiber Bragg grating SCOWECLs. The laser was maintained at 16 °C.

From Fig. 3-15, we see that the L-I characteristics for the 10 % and 20 % FBGs both suffer from a thermal rollover effect once the bias current extends beyond 3 A. However, compared to the L-I for the erbium-doped SCOWECL case (Fig. A-4), this roll-over is much less pronounced. Furthermore, the differential efficiency is also higher without the Erbium fiber (26.7 % as compared to 10.4 % for the 20 % reflectivity grating case) since the Erbium saturable absorber

introduces loss. The combination of these two properties allows the SCOWECL to reach much higher output powers, as confirmed by Fig. 3-15. Comparing the 10 % and 20 % L-I characteristics, the 10 % grating reaches a higher output power of 450 mW compared to the 20 % grating power of 400 mW. This is largely due to its higher differential efficiency. Finally, the threshold current of the 10 % FBG is larger due to the larger intra-cavity losses incurred using a lower reflectivity grating. A summary of the L-I comparison between the FBGs is provided in Table 3-2.

L-I Comparison	Peak Output Power (mW)	Threshold Current (A)	Differential Efficiency (%)
10 % FBG	450 mW	1.15 A	26.7 %
20 % FBG	400 mW	0.95 A	21.9 %

Table 3-2: L-I comparison between 10 % and 20 % FBG SCOWECLS.

The ripples in the L-I characteristics are due to mode hop effects as the bias current is ramped. However, at a fixed current and with optimal alignment, the SCOWECL is able to operate in a stable single longitudinal mode for over ten minutes in an isolated environment.

Butt-Coupling and Lensed Fiber Coupling Comparison

In order to fully evaluate the effect of the lensed fiber on the overall coupling efficiency, we compared the L-I characteristics of the butt-coupled and lensed fiber coupled external cavity lasers. The results of the comparison for currents up to 5 A are illustrated in Fig. 3-16.

Interestingly, according to Fig. 3-16, the lensed fiber and butt-coupled lasers exhibit almost identical threshold currents. This is unexpected since the use of lensed fibers should theoretically increase the coupling efficiency, thereby reducing the overall loss in the cavity. In addition, there does not appear to be any improvements in the differential efficiency from using lensed fiber coupling. However, the thermal rollover in the butt-coupled case is much more pronounced leading to a lower output power at high bias currents. Currently, it is unclear why the

coupling efficiency and threshold current is not improved when mode field matched lensed fiber coupling is employed. Further investigation is needed in order to fully describe the measured results.

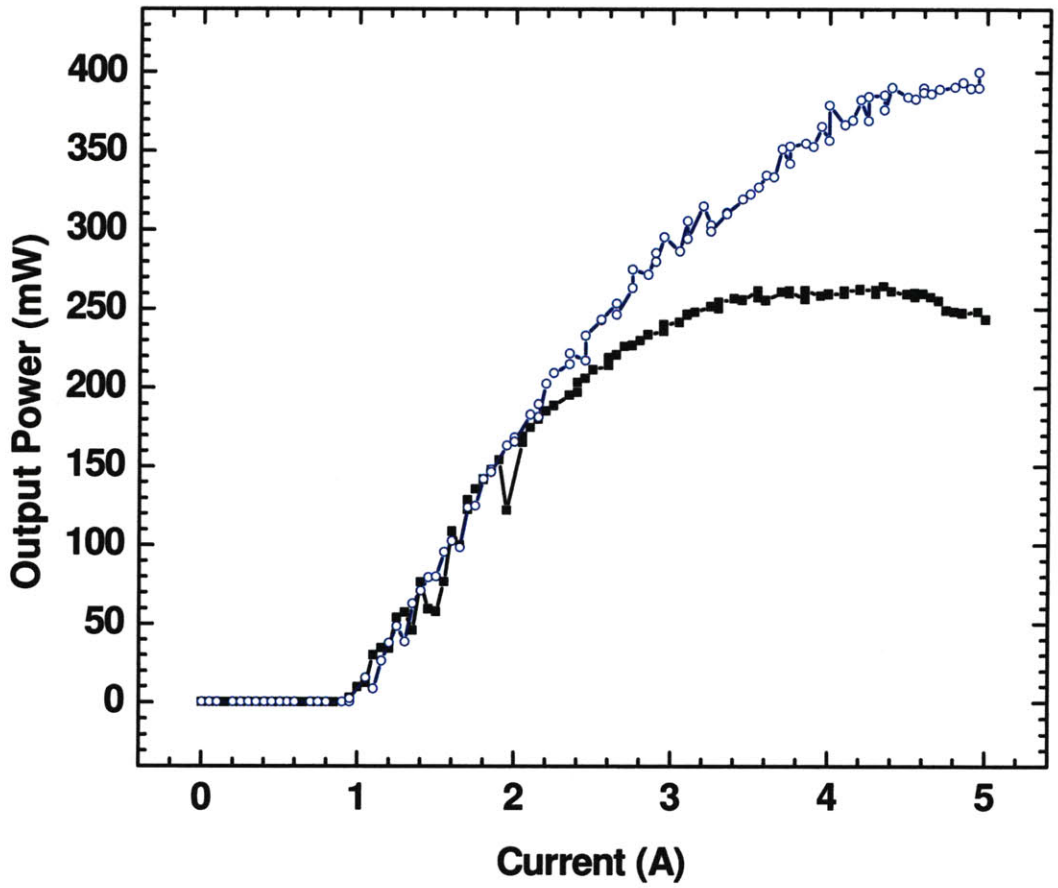

Figure 3-16: L-I comparison of lensed fiber (open circles) and butt-coupled (solid squares) SCOWECLs. The lasers were maintained at 16 °C over the current sweep.

Electrical-to-Optical Conversion Efficiency Measurement

The electrical-to-optical conversion (E-to-O) efficiency of the lasers can be calculated as a function of the bias current with the help of the SCOWA I-V and laser L-I measurements. The results of the 10 % and 20 % electrical-to-optical conversion efficiency measurements are illustrated in Fig. 3-17.

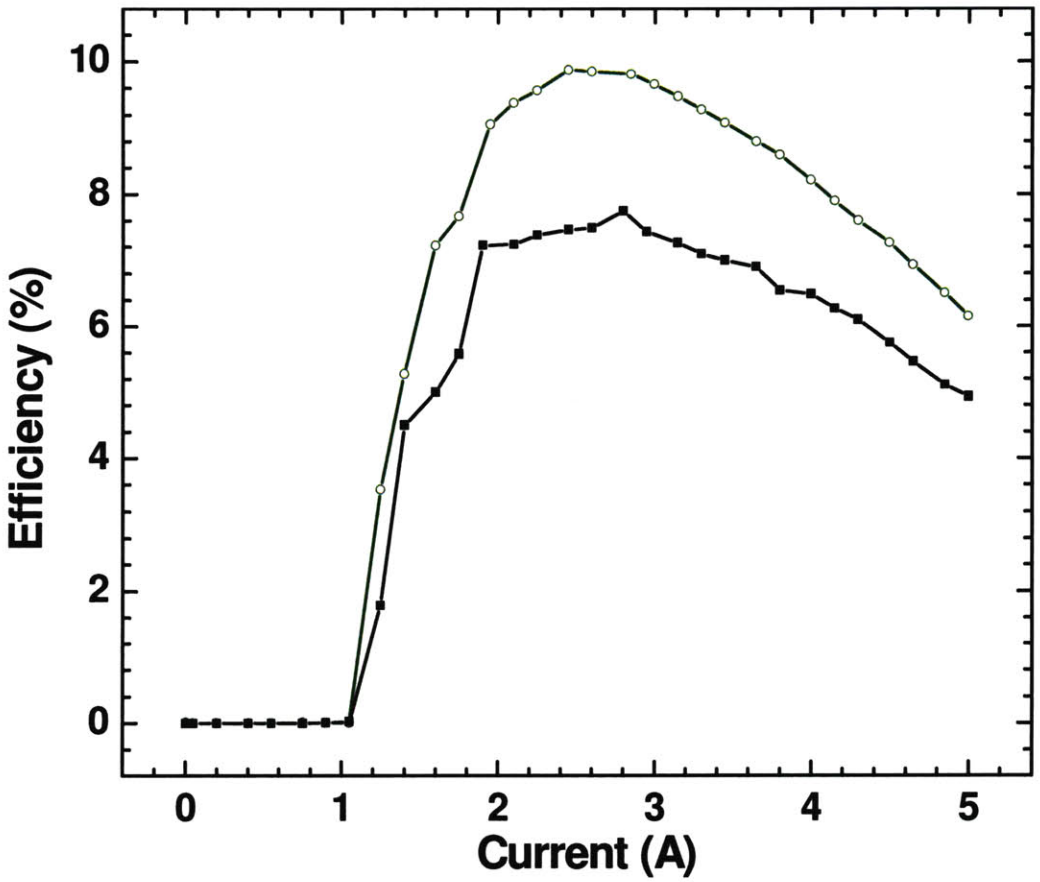

Figure 3-17: Electrical-to-Optical conversion efficiency for 10 % (open circles) and 20 % (solid squares) grating SCOWECLs as a function of current bias. The laser was operated at 16 °C.

Fig. 3-17 indicates that both the 10 % and 20 % FBG SCOWECLs never reach E-to-O efficiencies beyond 10 % across the entire tested current bias range. The threshold current at ~ 1 A is clearly apparent in the graph. The illusion of the 10 % and 20 % FBG SCOWECLs sharing the same threshold is due to the coarse current sampling used during the efficiency calculation. Above 3 A, the efficiency continuously drops in both cases. This is not surprising given the thermal rollover effects seen in the previous measured L-I characteristics. In general, however, these efficiency levels are relatively low for a laser. This is partially due to the large unexpected loss in the coupling of lensed fibers to the SCOWA device. Nonlinear effects such as two photon absorption can also account for much of the optical power lost at high output powers. This will be discussed in greater detail during a future section.

3.3.2 SCOWECL RIN Measurements

RIN measurements were performed on the SCOWECL in order to determine the intensity noise level of the laser under CW operation. The RIN measurements were performed at 4 A bias across a frequency range of 10 kHz – 10 GHz. The frequency sweep was implemented in two separate scans of the laser noise spectrum. The first scan was performed across a frequency range of 10 kHz – 2 MHz in order to provide a high resolution measurement of the low frequency RIN spectrum. The second sweep was performed across a frequency range of 10 kHz – 10 GHz for the purposes of capturing the relaxation resonance and side mode beating effects in the high frequency RIN spectrum. The RIN measurement setup, theory, and results are presented next.

RIN Measurement Setup

The setup for both the low and high frequency laser RIN tests is shown in Fig. 3-18.

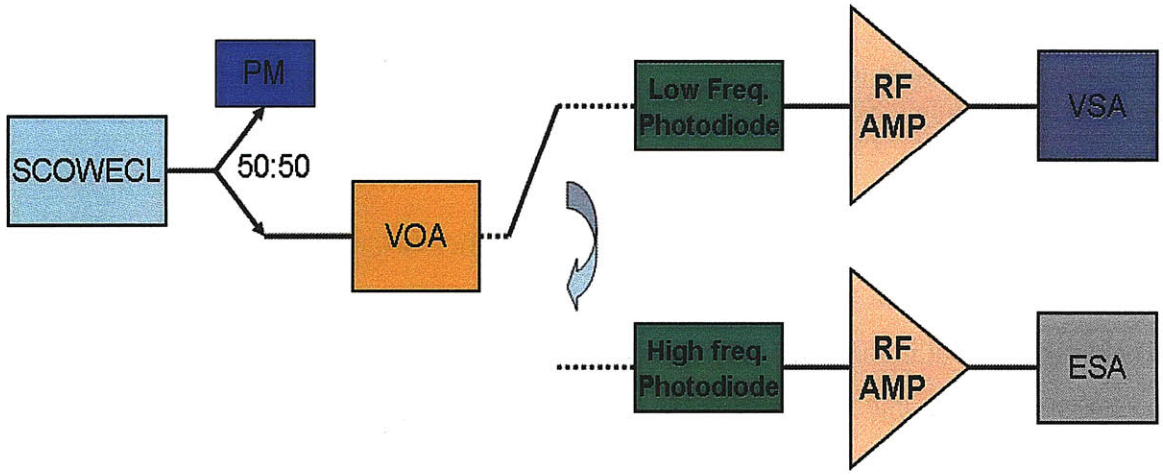

Figure 3-18: Low and high frequency laser RIN measurement system

The output of the SCOWECL is first sent to a 50/50 splitter. One of the splitter taps is monitored by a power meter (PM), while the other tap is redirected to a variable optical attenuator (VOA).

In the low frequency RIN measurement system, the attenuator output is detected by a 1 GHz bandwidth photodiode. The photocurrent is then amplified by a 3.15 GHz bandwidth RF amplifier before it is processed by an Agilent 89410A vector signal analyzer (VSA). In the high frequency RIN measurement, a 40 GHz photodiode is used along with a 26 GHz RF amplifier in the place of the low frequency equivalent diction system. The output is sent to a HP8565E electrical spectrum analyzer (ESA), which processes the spectrum of the amplified signal.

RIN Measurement Theory

The measurement of the laser relative intensity noise is in many ways similar to the electrical noise figure measurements described in Chapter 2. This is evidence of the strong correlation between laser RIN and optical amplifier noise figure. To measure RIN, a direct measurement of $(\Delta P)^2/(\overline{P})^2$ (Eq. 1.28) is performed. The electrical signal analog to this equation after detection by the photodiode is

$$RIN = \frac{(\Delta i)^2}{(\bar{i})^2} \tag{3.9}$$

where $(\Delta i)^2$ is the mean-square noise current and $(\bar{i})^2$ is the square of the average photocurrent. The mean-square noise current at a particular frequency is easily measured through use of an electrical spectrum analyzer. However, the measurement result is complicated by an additional multiplication with the system transfer function since the photocurrent is converted into a voltage signal before reaching the ESA. This transfer function can be calibrated out of the measurement using the RIN transfer technique described in Chapter 2. The average photocurrent can be determined with an ammeter measurement of the photodiode output. The ratio of the two results yields the relative intensity noise at the frequency of the noise component. This process can be performed for a spectrum of frequencies to fully characterize the laser RIN across a frequency band of interested. The thermal noise is subtracted out in all cases in order to obtain higher measurement accuracy.

Low Frequency RIN Measurement Results

The previously described technique was applied to characterize the SCOWECL RIN across both low and high frequency ranges of operation. The low frequency measurement was performed for laser bias currents ranging from 1.5 A to 4.5 A across a 0 – 2 MHz span. The results of the RIN characterization at 4 A for both the 10 % and 20 % grating SCOWECLs are shown in Fig. 3-19 along with the calculated shot noise RIN level. Similar performance levels are achieved across the range of bias currents tested.

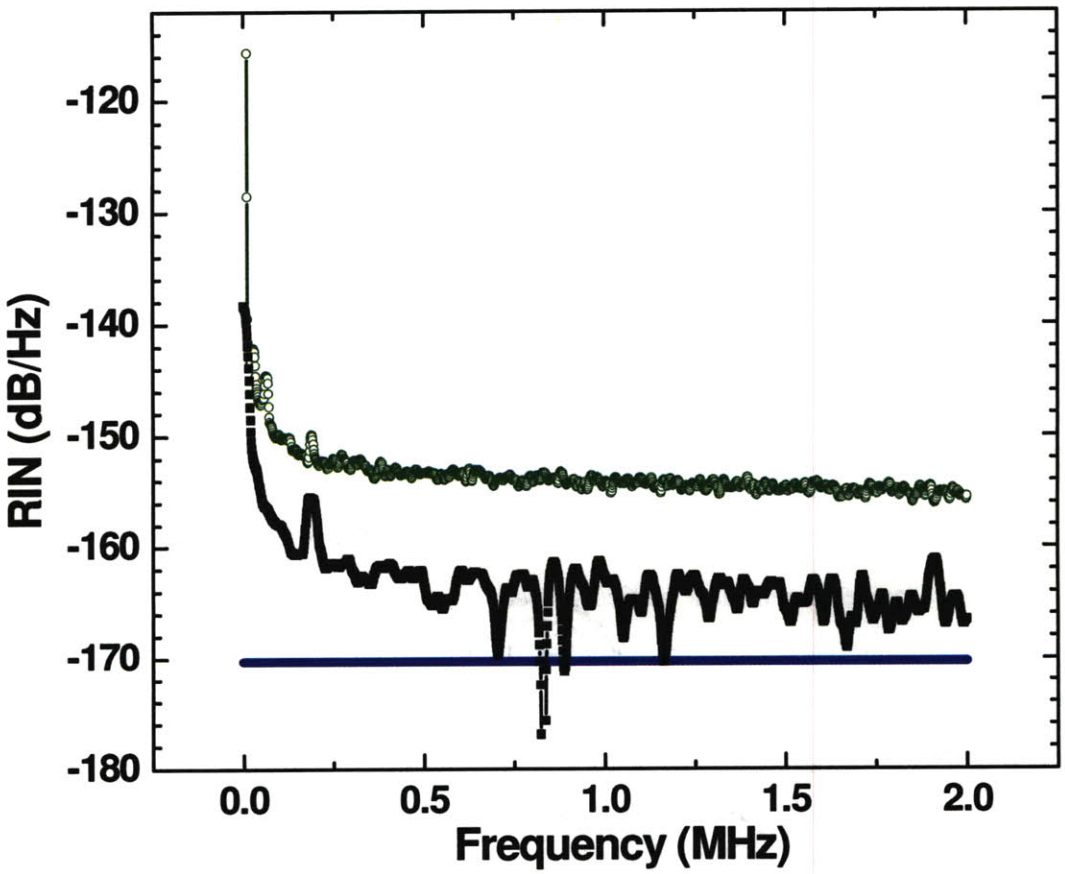

Figure 3-19: Low frequency RIN spectrum for 10 % (open circles) and 20 % (solid squares) FBG SCOWECLs. The shot noise RIN is indicated by the horizontal line. The laser was operated at 4 A bias and maintained at a temperature of 16 °C. The photodiode current in both cases was ~ 35 mA.

The results of the low frequency RIN measurements indicate that neither the 10 % nor the 20 % SCOWECLs operate at the shot noise limit below 2 MHz. However, the noise performance of the 20 % FBG laser (≈ -165 dB/Hz) is noticeably better than that of the 10 % laser (≈ -155 dB/Hz). This is largely attributed to the higher cavity quality factor (Q) when resonant feedback effects are increased (via increased grating reflectivity). In a high Q cavity, most of the stimulated emission power is used to pump the central lasing mode so that power is not wasted in energizing other spontaneously emitted modes. Fig. 3-19 also shows evidence of a spectral peak near 200 kHz. This peak is part of the electronic detection system as the peak was present even when the optical signal was blocked. The increase in RIN at the lower frequencies is most likely due to 1/f noise contributions from the laser's current supply source and/or from the laser itself.

High Frequency RIN Measurement Results

The high frequency RIN was measured at a laser bias of 4 A for frequencies ranging from 10 kHz – 10 GHz. The 10 % and 20 % SCOWECL high frequency RIN results are shown in Figs. 3-20 (a) and (b). The high frequency RIN results indicate shot noise limited performance for the SCOWECL with the 20 % fiber Bragg grating reflector across the 10 GHz frequency span. The 10 % SCOWECL RIN noise is slightly worse and also exhibits a sharp RIN peak at ~ 2.4 GHz. This peak is due to the beating of two incompletely suppressed side modes in the laser cavity. The side modes are expected to be spaced apart by 1.2 GHz as calculated using Eq. 3.7. We see that the 2.4 GHz peak corresponds to a beat note of modes spaced exactly two free spectral ranges apart. The peak at 1.3 GHz likely corresponds to the beat frequency between two adjacent side modes but is not far enough above the shot noise floor to draw any definite conclusions. Similarly, the peak at 2.6 GHz seen in the 20 % SCOWECL RIN measurement may also be due to side mode beating effects.

Currently, it is unclear why the low and high frequency RIN results yield different levels of laser noise performance. However, this difference is not due to the photocurrent limitation of the high frequency RIN photodiode as shot noise limited performance at the -170 dB/Hz level has recently been measured. The difference in results is intrinsic to the low frequency noise spectrum of the laser.

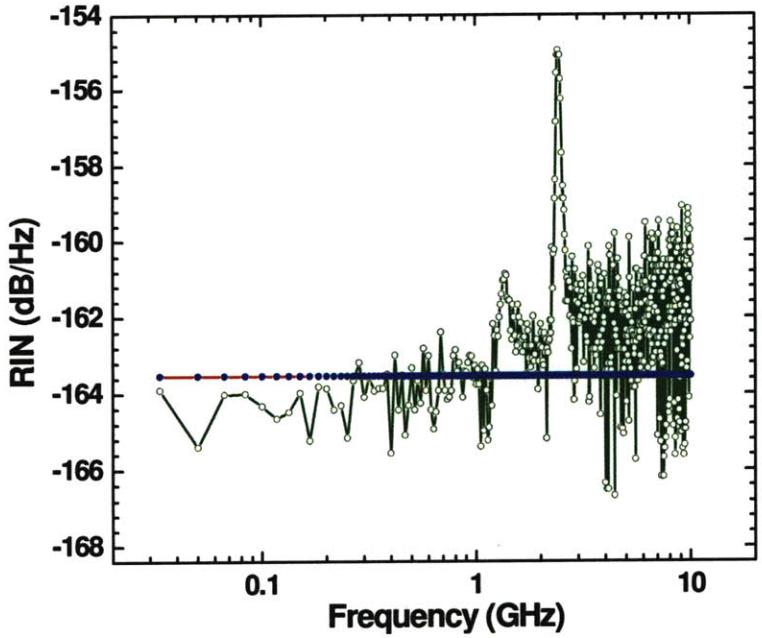

(a)

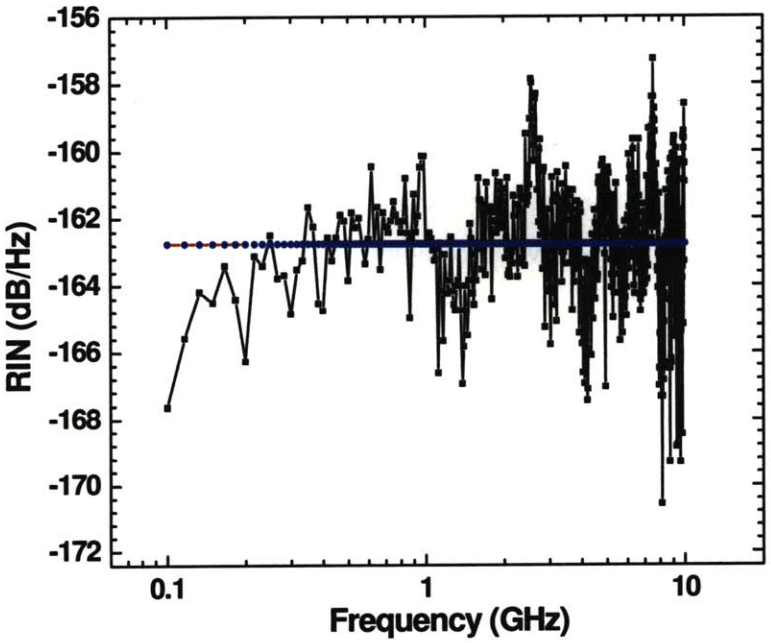

(b)

Figures 3-20 (a) and (b): Plot of the high frequency RIN for (a) 10 % and (b) 20 % FBG SCOWECLs. The shot noise RIN level is indicated in each case with a horizontal line. Photocurrents of 7 mA in (a) and 6 mA in (b) were used to derive the shot noise levels. The laser was operated at 4 A bias and maintained at a temperature of 16 °C in both trials.

It should be noted that the RIN measurements performed previously were taken shortly after the laser alignment was optimized. For a long delay between measurement and alignment, the RIN measured for the 20 % FBG SCOWECL showed signs of instability. The results of the high frequency RIN spectrum after a long free-running time interval are shown in Fig. 3-21.

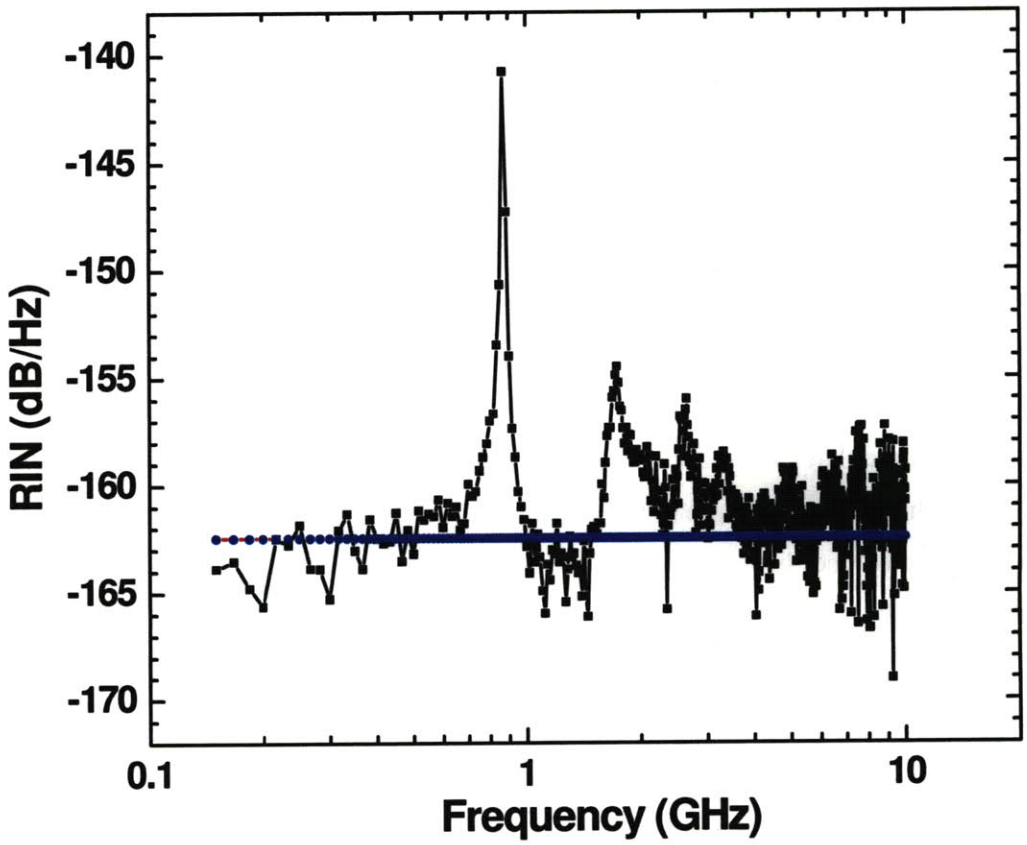

Figure 3-21: High frequency RIN spectrum of 20 % SCOWECL for long time delay between laser alignment and measurement. The horizontal line is the shot noise RIN. The laser was operated at 4 A bias and maintained at a temperature of 16 °C. The photodiode current was approximately 6 mA.

Fig. 3-21 indicates the presence of multiple side mode peaks with the main peak occurring at 0.87 GHz. The second, third and fourth peaks occur at the frequencies 1.7 GHz, 2.6 GHz, and 3.3 GHz. These peaks occur at beat notes between multiples of the free spectral range. In this particular case, the FSR is seen to be 0.87 GHz, in contrast to the predicted FSR of 1.2 GHz.

This is likely to be due to length inaccuracies in the lensed fiber and fiber Bragg grating during the assembly process of the passive cavity. The lower than expected free spectral range also explains why side mode instabilities were observed in the RIN spectrum. These instability effects were not seen in any of the other 10 % and 20 % SCOWECLs tested to date.

3.3.3 SCOWECL Linewidth Measurements

The SCOWECL linewidth was determined using the delayed self-heterodyne technique. The beat note spectrum of the laser signal with its delayed replica can be used to determine the laser linewidth as long as the two signals are no longer coherent with each other. This manifests itself as a requirement that the delay path be long in comparison to the coherence length of the laser. If the delay length is not long enough, coherence artifacts appear in the beat spectrum of the two signals. The delayed self-heterodyne technique imposes no other restrictions on the laser properties and requires no additional components other than a fiber delay line and an optical modulator. The modulator is used to shift the beat spectrum away from 0 Hz. The delayed self-heterodyne method finds widespread use because of its simplicity compared to other linewidth extraction methods and because of its applicability to measuring very narrow linewidths approaching 1 kHz. This section details the delayed self-heterodyne linewidth measurement setup and presents the relevant theory for the measurement technique. The linewidth results of 10 % and 20 % Bragg reflector SCOWECLs will also be discussed.

Delayed Self-Heterodyne Linewidth Measurement Setup

The setup for the delayed self-heterodyne measurement is shown in Fig. 3-22. The output of the SCOWECL enters a 50/50 splitter. One port of the splitter is sent to a power meter (PM) in order to monitor the laser power. The other port is sent to a variable optical attenuator (VOA) for control of the optical signal level. The output of the attenuator is sent to another 50/50 splitter. One tap of the splitter is sent through 50 km of fiber delay and an acousto-optic modulator (AOM). The AOM modulates the optical signal to shift its frequency by 35 MHz. The other tap is sent to a polarization controller (PC) for control of the relative polarization between the two

paths. The two paths are combined with a third 50/50 splitter and the combined signal is detected by a photodiode. Detection of the optical signal results in beating effects between the original and delayed signals within the photocurrent. The photocurrent output is then amplified by the RF amplifier. The electrical spectrum analyzer (ESA) displays the spectrum of the photocurrent.

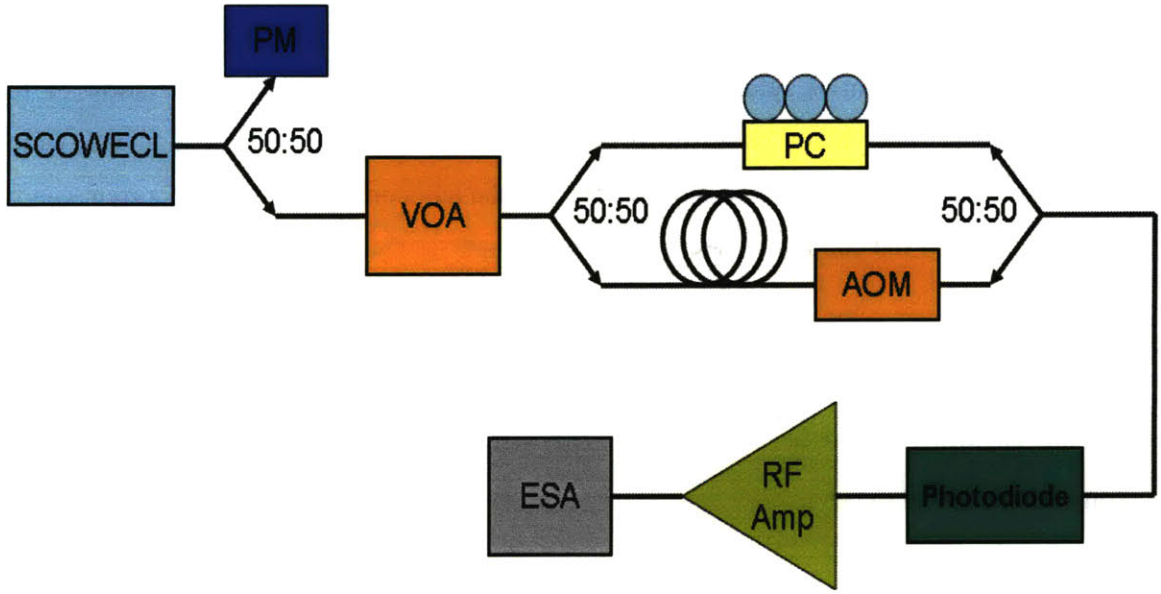

Figure 3-22: Delayed self-heterodyne linewidth measurement setup

The laser was placed in a plexiglass box to prevent environment noise from interfering with the measurement. The laser itself was mounted on a metallic plate resting on foam blocks. These block help to damp out vibrations that may otherwise disrupt laser stability. The external cavity fiber was taped down onto a holding plate to prevent motion in the fiber. These precautions are needed in order to ensure optimal laser performance during the linewidth measurements.

Delayed Self-Heterodyne Linewidth Measurement Theory

Here we present a brief overview of the delayed self-heterodyne theory in order to gain useful intuition of the expected measurement results. The combined optical field at the input to the photodiode results from the superposition of a signal with its delayed and modulated replica after

propagation through the arms of the interferometer. Following the treatment of [58], this can be mathematically expressed as

$$E_T(t) = E(t) + kE(t+\tau_0)e^{j\Omega t} \tag{3.10}$$

where E(t) is the original electric field, E(t+τ_0) is the delayed electric field, k is the power ratio between the two paths, and Ω is the modulation frequency. By the Wiener–Khinchin theorem, the photocurrent spectrum is related to the Fourier transform of the autocorrelation of the photocurrent signal. The photocurrent signal is directly proportional to the optical signal, which is related to the square of the electric field. Therefore, the autocorrelation in photocurrent can be expressed in terms of the combined electric field as

$$G^{(2)}_{E_T}(\tau) = \left\langle E_T(t)E_T^*(t)E_T(t+\tau)E_T^*(t+\tau)\right\rangle. \tag{3.11}$$

Taking the electric field to be of the form $E(t) = E_0 e^{j[\omega_0 t+\phi(t)]}$, the normalized photocurrent spectrum can be found to be

$$\begin{aligned} S_I(\omega) = &\left[1+k^2\right]^2 \delta\left(\frac{\omega}{2\pi\Delta\upsilon}\right) + k^2 e^{(-2\pi\Delta\upsilon\tau_0)}\delta\left(\frac{\omega-\Omega}{2\pi\Delta\upsilon}\right) \\ &+ k^2 e^{(-2\pi\Delta\upsilon\tau_0)} \frac{1/\pi}{1+\left((\omega-\Omega)/(2\pi\Delta\upsilon)\right)^2}\left[e^{2\pi\Delta\upsilon\tau_0}\right. \\ &\left. - \frac{2\pi\Delta\upsilon\sin\left((\omega-\Omega)\tau_0\right)}{\omega-\Omega} - \cos\left((\omega-\Omega)\tau_0\right)\right] \end{aligned} \tag{3.12}$$

where ω_0 is the electric field frequency, $\varphi(t)$ is the time varying field phase, $\Delta\upsilon$ is the laser linewidth., and ω is the angular frequency variable of the spectrum. In Eq. (3.12), the first term results from the second order self-correlation of each of the optical fields along the interferometer arms, while the second term results from their cross-correlation. The third term represents interference from a partially coherent mixing of the signal and its delayed replica.

The delta peak at 0 Hz in Eq. (3.12) is isolated from the mixing signal of interest centered at Ω and thus does not play a role in the linewidth measurement. In addition, for long path delay times, all the terms that exponentially depend on the delay time rapidly approach zero. Only the pure Lorentzian term survives in the spectrum. Therefore, it is critical to remove the coherence

between the two paths as residual delta peaks and sinusoidal ripples in the spectrum occur for a partially coherent mixing. However, a longer fiber delay length results in a larger 1/f linewidth contribution. The 1/f linewidth will become important later when the linewidth results are discussed. In the partially coherent case, the measured linewidth is lower than expected since power is shifted from the Lorentzian base to the delta function peak. This has the effect of causing the Lorentzian to appear narrower.

With a 50 km fiber delay, the calculated minimum linewidth that can be resolved is 955 Hz. This is the linewidth required to cause the argument of the exponential to become unity so that only the Lorentzian term remains within the photocurrent spectrum. This minimum in linewidth is present since the delayed self-heterodyne technique relies on the mixing of two signals that are incoherent with each other. If the path delay length is not long enough to break the coherence between the original signal and its delayed replica, partially coherent beat noise will be present in the measured photocurrent spectrum. As will be shown later in the linewidth results, the measured Lorentzian linewidths for the 10 % and 20 % FBG SCOWECLs are both within the required range for a 50 km fiber delay length to suppress coherent artifact effects.

Delayed Self-Heterodyne Linewidth Measurement Results

The delayed self-heterodyne technique was performed to measure the linewidth of SCOWECLs employing 10 % and 20 % fiber Bragg gratings. The measurement results are shown in Fig. 3-23. The linewidth of the laser is extracted by fitting Gaussian and Lorentzian functions to the delayed self-heterodyne spectrum. 1/f noise dominates the low frequency portion of the spectrum but quickly loses strength at the tails of the lineshape. The 1/f noise produces a Gaussian function at low frequencies. Gaussian fits to the center (low frequency) portion of the spectrum are performed in order to estimate the 1/f contribution to the laser linewidth. At the tails of the spectrum, the laser white noise becomes the dominant frequency noise component. The white noise lineshape is purely Lorentzian. Its contribution to the laser linewidth can be determined by a Lorentzian fit to the tails of the self-heterodyne measurement. The combination of the Gaussian center and Lorentzian tails produces a Voight lineshape function. The results of the Gaussian and Lorenzian fits are summarized in Table 3-3.

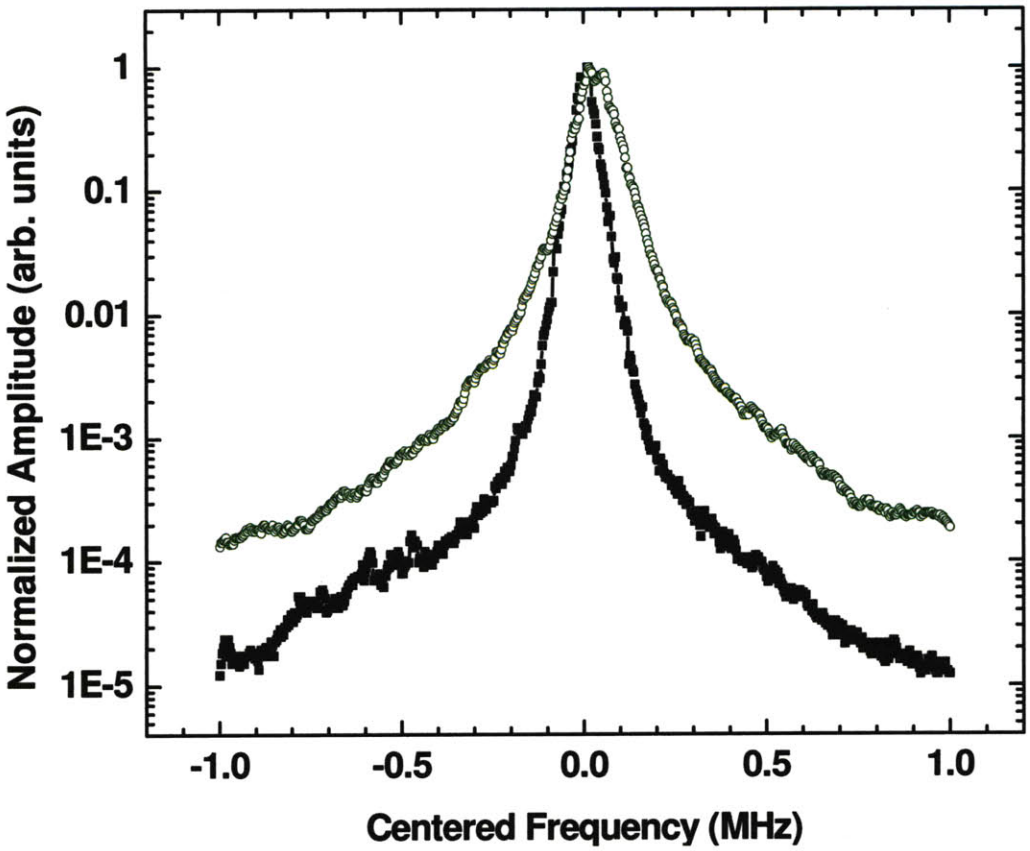

Figure 3-23: Delayed self-heterodyne spectrum of 10 % (open circles) and 20 % (solid squares) reflectivity SCOWECL. The laser was operated at 4 A bias and maintained at a temperature of 16 °C.

Linewidth Fits	Gaussian	Lorentzian
10 % SCOWECL	51.6 kHz	15.4 kHz
20 % SCOWECL	27.9 kHz	5.75 kHz

Table 3-3: Linewidth fits to 10 % and 20 % grating SCOWECLs for a current bias of 4 A.

The results of the fitting show that the Gaussian and Lorentzian contributions to the linewidth are both larger for the 10 % reflectivity SCOWECL. The use of a lower reflectivity grating decreases the quality factor of the cavity. This results in a decrease in the sharpness of the Fabry-Perot resonances and a corresponding broadening of the linewidth. Despite the larger relative linewidths in the 10 % SCOWECL, both laser configurations tested display excellent bench-top

free running linewidths. It is expected that the use of laser feedback stabilization techniques can further reduce the linewidth to even lower levels.

3.4 Packaged SCOWECL Characterization

Based on the previous comparisons of the L-I, RIN, and linewidth for SCOWECLs employing 10 % and 20 % reflector FBGs, it is clear that a 20 % grating must be used for optimum RIN and linewidth performance. The output power gained using a 10 % grating does not outweigh the corresponding large degradation in laser noise characteristics. One of the tested 20 % FBG SCOWECLs was packaged for the purposes of delivery to several collaborators. The packaging was accomplished using a Newport automated laser welding system. A top-down view of the finalized package is shown in Fig. 3-24. A close-up view of the mounted SCOWA device along with the aligned lensed fiber is provided in Fig. 3-25.

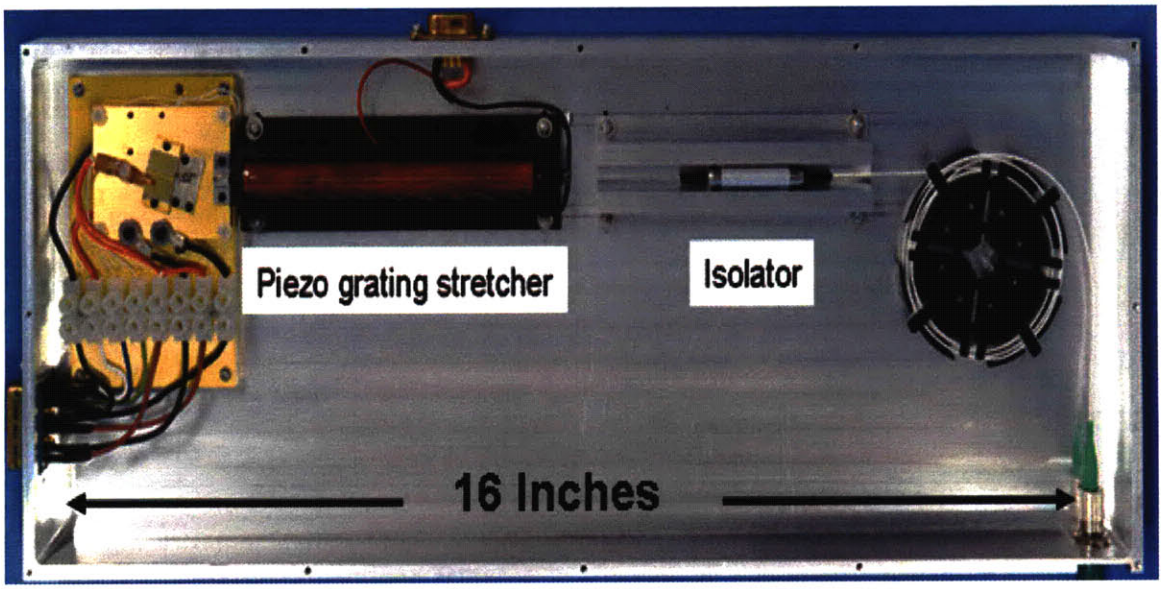

Figure 3-24: Top-down view of packaged SCOWECL.

The performance characteristics of the packaged SCOWECL were measured prior to delivery in order to verify correct functionality. Table 3-4 summarizes the output power, RIN, and linewidth performance of the packaged SCOWECL measured at 4 A bias.

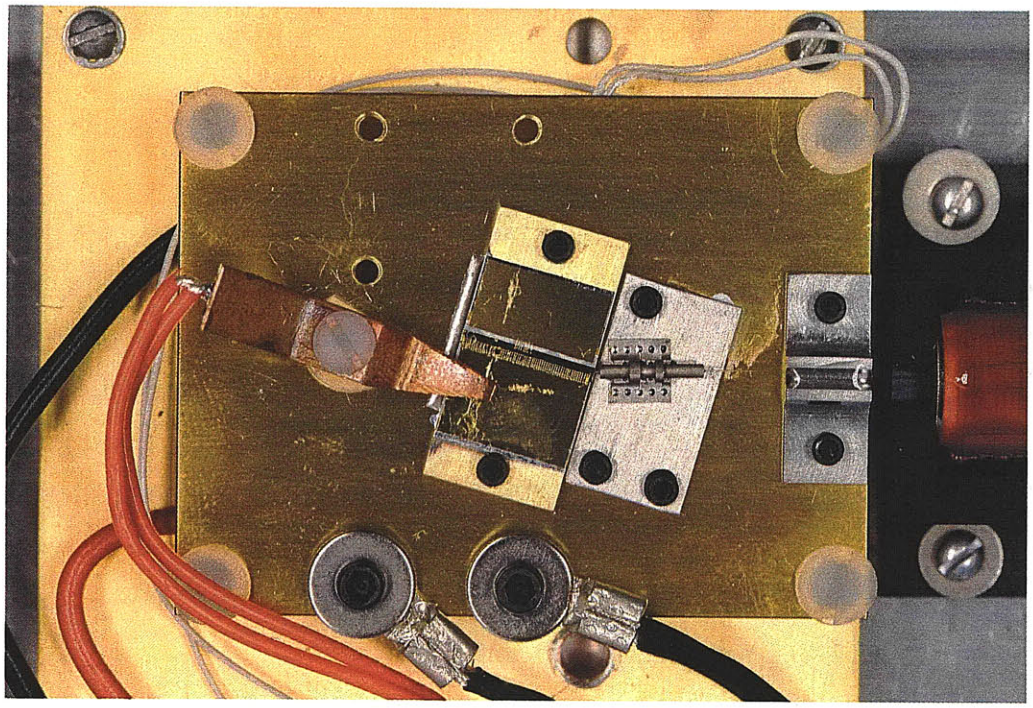

Figure 3-25: Close-up view of mounted SCOWA.

	Output Power at 4 A (mW)	Low Frequency RIN (dB/Hz)	High Frequency RIN (dB/Hz)	Gaussian Linewidth (kHz)	Lorentzian Linewidth (kHz)
Packaged SCOWECL	370 mW	-163 dB/Hz (at ~ 2 MHz)	-162 dB/Hz Shot noise limited	19.4 kHz	2.17 kHz

Table 3-4: Summary of packaged SCOWECL output power, relative intensity noise, and linewidth performance. The laser was operated at 4 A bias and thermo-electrically cooled to 16 °C.

Compared to the bench-top measured performance characteristics (not shown in this thesis), the output power takes a ~ 8 % penalty from the fiber alignment process during the laser

packaging. A coupling penalty is inevitable in a packaging process which requires active alignment of the device and fiber modes down to the micron tolerance level. However, both the Gaussian and Lorentzian linewidth contributions have significantly improved with the Gaussian linewidth decreasing to 19.4 kHz from 46 kHz and the Lorentzian linewidth decreasing to 2.17 kHz from 7.42 kHz (bench-top results of this laser were not reported in this thesis). The Gaussian linewidth improvement is due to an increase in laser stability resulting from mounting the laser in the package. This may also impact the extracted Lorentzian linewidth if the lineshape was constantly moving around during the spectrum analyzer measurement averaging process.

The RIN performance of the laser was similar before and after packaging with the low frequency RIN below -162 dB/Hz and the high frequency RIN performing at the shot noise limit. The absence of mode beating at the shot noise levels suggests that the side mode suppression for the SCOWECL is > 80 dB. In both the bench-top and packaged laser RIN measurements, relaxation oscillation resonance peaks were not observed in any of the measured spectra. This result is contrary to expectation as semiconductor lasers typically exhibit a peak in intensity noise beyond 1 GHz due to the resonance interaction between photons and electrons. To verify the correctness of our RIN measurement system, we measured the relative intensity noise of a commercial Nortel networks distributed feedback (DFB) laser in the same 10 kHz – 10 GHz frequency range. The RIN measurement results are shown in Fig. 3-26.

The relaxation oscillation peak is clearly present in the measured Nortel Networks DFB laser RIN spectrum and appears to reach a maximum near 9 GHz. This gives us confidence in our previously measured results of relative intensity noise for the bench-top and packaged SCOWECL. The absence of a relaxation oscillation peak in the SCOWECL can be due to damping of the electron-photon resonance. The low losses in SCOWECL lasers produce long photon lifetimes which can effectively decouple the electron dynamics from the photon dynamics. It is currently unclear what the large oscillations below 1 GHz in the Nortel Networks RIN is due to. However, the oscillations are repeatable between all measurement trials and is consistently absent in all RIN measurements of the SCOWECL.

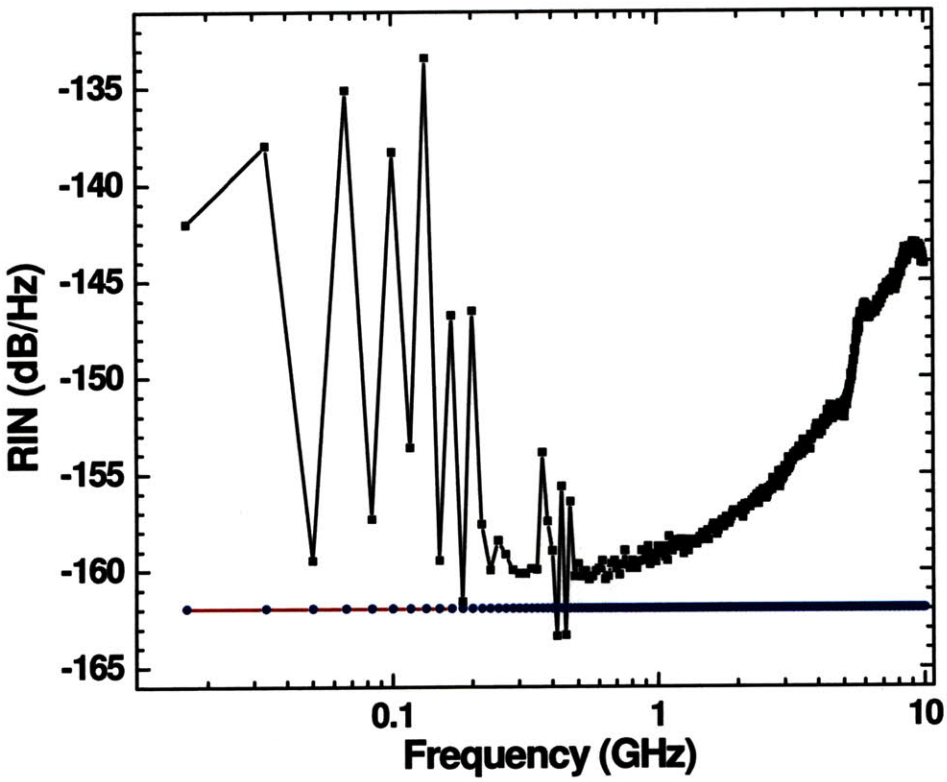

Figure 3-26: High frequency RIN spectrum of Nortel Networks laser. The horizontal line is the shot noise RIN. The laser was operated at 220 mA bias and maintained at a temperature of 16 °C. The photodiode current was approximately 5 mA.

The fiber Bragg grating tuning characteristics were also measured in order to verify proper stretching of the grating when mounted in the package. Fig. 3-27 illustrates the results of the stretch measurements for applied piezo biases of 0 – 1000 V in 200 V increments. From the figure, it is seen that the laser operates at a wavelength of 1550.4 nm when the grating is unstretched. This confirms that the wavelength selective FBG is correctly establishing lasing for the 1550 nm longitudinal mode. The total tuning range is 1.35 nm after the application of 1000 V to the piezo actuator. This result is consistent with our previous tuning range measurement of 1.47 nm performed on a 5 % grating. No significant decrease in laser power could be observed over the piezo bias range tested. Furthermore, the wavelength shift is also relatively uniform with the applied voltage. These results indicate that the FBG was tautly and uniformly epoxied to the piezo stretcher during the laser packaging process.

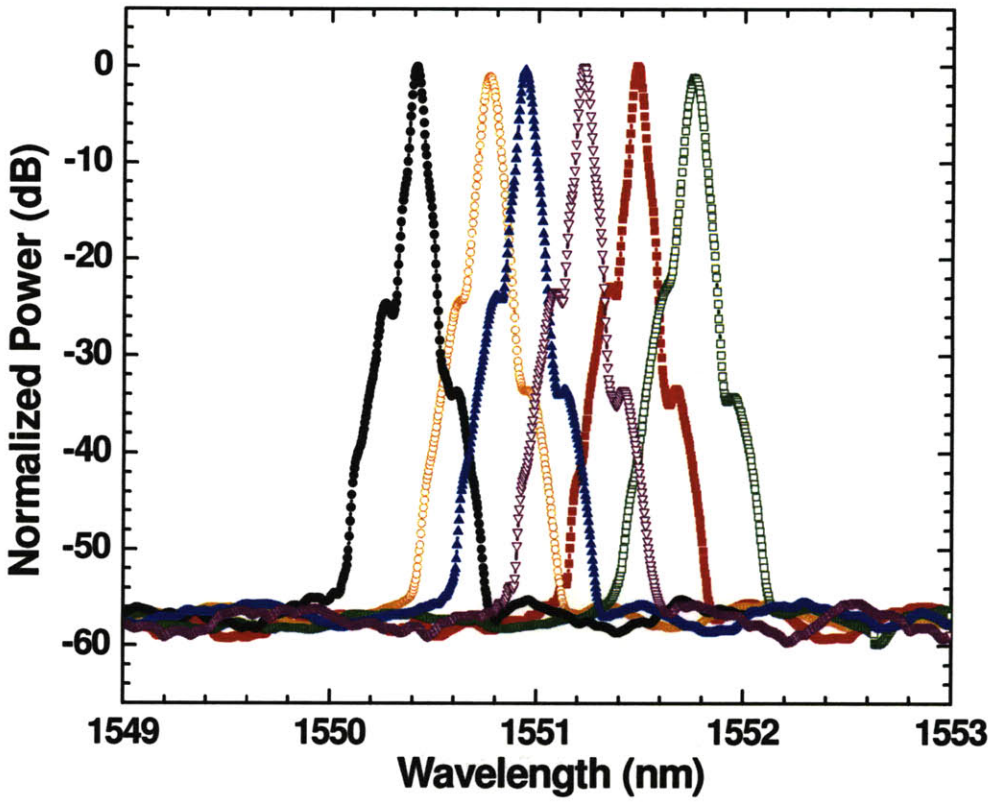

Figure 3-27: Fiber Bragg grating tuning characteristics for piezo biases of 0 V (solid circles), 200 V (open circles), 400 V (solid triangles), 600 V (open triangles), 800 V (solid squares), and 1000 V (open squares). The laser was operated at 4 A bias and maintained at 16 °C during the measurement.

3.5 SCOWECL Modeling

The SCOWECL characteristics were modeled in order to verify experimental results with theory developed for semiconductor external cavity lasers. Instead of using a rate equation approach, the theory presented in this section begins directly at the L-I relations of the laser. Comparisons of the simulated output power with the measured output power can be performed for the purposes of gaining deeper insight into the behavior of the SCOWECL. The linewidth is simulated afterwards, once the L-I model has been developed. This section describes the results of the L-I and linewidth simulations for the 20 % reflectivity SCOWECL measured in Section 3.3.

3.5.1 SCOWECL L-I Modeling

The SCOWECL L-I model begins with representing the linear characteristics between output power and current by

$$P = \eta_d (I - I_{th}) \tag{3.13}$$

where η_d is the differential quantum efficiency, I is the current bias, and I_{th} is the threshold current. Below threshold, the output power is approximately zero. For an external cavity laser, η_d consists of contributions from four distinct physical processes in the laser. This can be written as [37]

$$\eta_d = \eta_i \eta_{da} \eta_{dp} \eta_{ext} F \,. \tag{3.14}$$

η_i is the injection efficiency, and was previously measured in the SCOWL cutback measurements. η_{da} is the active cavity differential efficiency and is given by

$$\eta_{da} = \frac{\ln \sqrt{1/R_1 R_2}}{\langle \alpha_i \rangle_{xy}^{a} L_a + \ln \sqrt{1/R_1 R_2}} \tag{3.15}$$

R_1 and R_2 are the effective facet reflectivities of the SCOWA device with the R_2 facet closest to the lensed fiber. $\langle \alpha_i \rangle_{xy}^{a}$ is the active medium internal loss, which was also measured in the SCOWL cutback measurements, and L_a is the active cavity length. η_{da} represents the ratio of the power coupled out of the active cavity facets to the power dissipated through internal loss. η_{dp} is the passive cavity differential efficiency and takes on the form

$$\eta_{dp} = \frac{(1-R_1)/\sqrt{R_1} + (1-R_3)/\sqrt{R_3}}{(1-R_1)/\sqrt{R_1} + \left(1-R_3 e^{-2\alpha_{ip} L_p}\right)/\sqrt{R_3} e^{-\alpha_{ip} L_p}} \tag{3.16}$$

where α_{ip} is the passive cavity internal loss and L_p is the passive cavity length. η_{dp} represents the ratio of the power leaving the laser to the power entering the passive cavity. η_{ext} is the external

efficiency due to the isolator and any other sources of power loss before the light is detected. Finally, F is the fractional power leaving the passive cavity as useful output and is given by

$$F = \frac{(1-R_3)/\sqrt{R_3}}{(1-R_1)/\sqrt{R_1}+(1-R_3)/\sqrt{R_3}} \tag{3.17}$$

R_3 is the reflectivity of the passive cavity output coupler. The SCOWA effective facet reflectivity R_2 is related to R_3 by

$$R_2 = R_3 e^{-2\alpha_{ip}L_p}. \tag{3.18}$$

Two photon absorption (TPA) effects were also accounted for by introducing an intensity dependent absorption coefficient to the active cavity. Furthermore, the free carrier absorption resulting from the TPA generated carriers were also modeled. The resulting active cavity internal loss is represented by [10]

$$\langle \alpha \rangle_{xy}^{a} = \alpha_{ia} + \beta_{TPA} I_S + \sigma_{2FCA}\left(\frac{\beta_{TPA} I_S^2 \tau_2}{h\upsilon}\right) \tag{3.19}$$

Where α_{ia} is the internal loss of the active material excluding TPA effects, β_{TPA} is the TPA coefficient, I_S is the signal intensity, σ_{2FCA} is the free carrier absorption (FCA) capture cross section, τ_2 is the TPA carrier lifetime, h is Planck's constant, and υ is the optical transition frequency. The laser output power can be simulated using Eqs. 3.13 – 3.19 along with the cavity threshold condition

$$\langle g \rangle_{xy} L_a = \langle \alpha_i \rangle_{xy}^{a} L_a + \alpha_{ip} L_a + \ln\frac{1}{\sqrt{R_1 R_3}}. \tag{3.20}$$

Here, $\langle g \rangle_{xy}$ is the modal gain of the SCOWA, which can be found from a logarithmic fit to the experimental amplifier gain curves measured in Fig. 3-4. Fig. 3-28 shows the results of fitting the expression

$$\langle g \rangle_{xy} = \langle g \rangle_0 \ln\left(\frac{I+I_s}{I_{tr}+I_s}\right) \tag{3.21}$$

to the SCOWA modal gain. An offset parameter α_0 was also added to Eq. (3.21) to account for the internal loss present in the gain measurement and also to account for differences in the expected coupling efficiency.

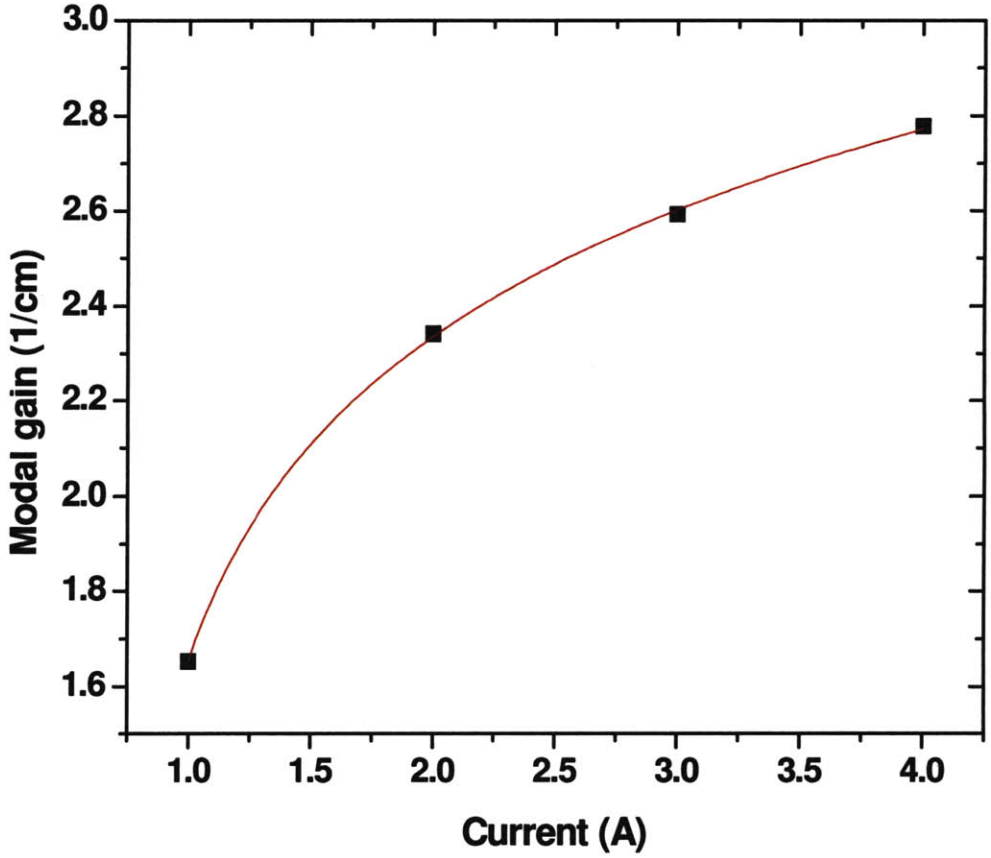

Figure 3-28: Theoretical fit to measured SCOWA gain. The determined best fit parameters are $\langle g \rangle_0 = 0.469$ cm^{-1}, $I_s = -0.696$ A, and $I_{tr} = 0.713$ A, and $\alpha_0 = -0.237$ cm^{-1}.

From Fig. 3-28, the modal gain fit is seen to coincide very well with the modal gain extracted from measurement over the entire range of bias currents tested. Using Eq. (3.21), the laser threshold gain can then be readily expressed in terms of the input current to the amplifier. The results of the self-consistent solution to the laser equations are illustrated in Fig. 3-29 for the 20 % FBG SCOWECL.

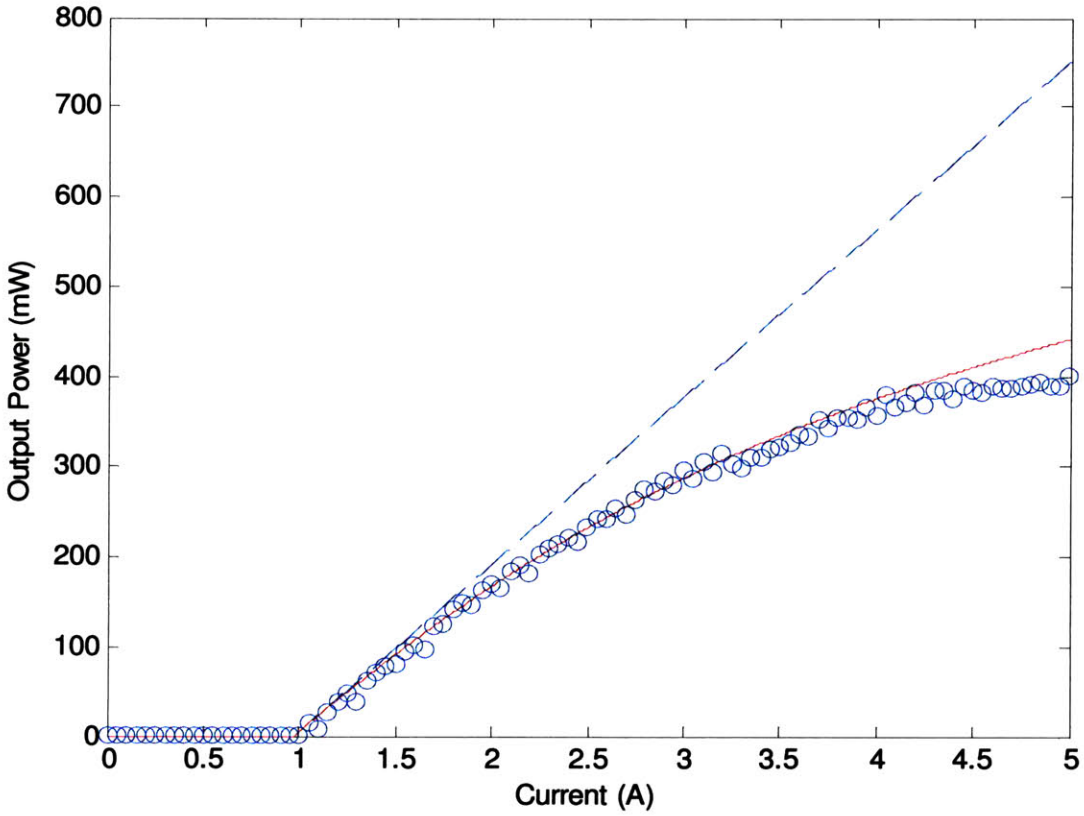

Figure 3-29: Plot of measured (open circles) and simulated (solid line) L-I characteristics for a 20 % reflectivity grating SCOWECL. The dashed line represents the theoretical L-I without two photon absorption effects.

The measured and simulated L-I results show excellent agreement at low currents. However, after 3 A bias, the measured results begins to experience a strong rollover in output power that cannot be completely accounted for by two photon absorption. This rollover is likely due to the presence of thermal effects such as thermal leakage of carriers out of the quantum wells or thermal lensing. From Fig. 3-29, it is clear that two photon absorption strongly limits the available output power of the tested external cavity lasers. The output power is predicted to reach 750 mW at 5 A bias when TPA and thermal effects are removed from the system. Therefore, almost half of the total power is lost to nonlinearities during laser operation.

It is interesting to point out that a 53 % single pass loss was required in the simulations in order to match the theoretical and experimental threshold currents. This loss is needed in addition to the already present internal losses and TPA losses in the cavity. It is unclear at this point as to what additional loss mechanisms are present in the SCOWECL design. However, one

possibility is loss due to polarization rotation of light into the TM mode. The SCOWA itself intrinsically emits spontaneous emission in the TE polarization and only actively amplifies TE light. However, passage through the passive cavity lensed fiber may cause a slight rotation in the light so that any TM converted light will now not be amplified. This effect can contribute to significant losses in the cavity. Further tests are needed to verify this hypothesis.

3.5.2 SCOWECL Linewidth Modeling

The linewidth of the SCOWECL can be simulated with the help of the L-I model developed in Section 3.5.1. Eq. (1.33) is used to calculate the Schawlow-Townes limited linewidth approximating the effects of the external cavity as a square law in the fractional passive cavity length. The results of the simulation are shown in Fig. 3-30.

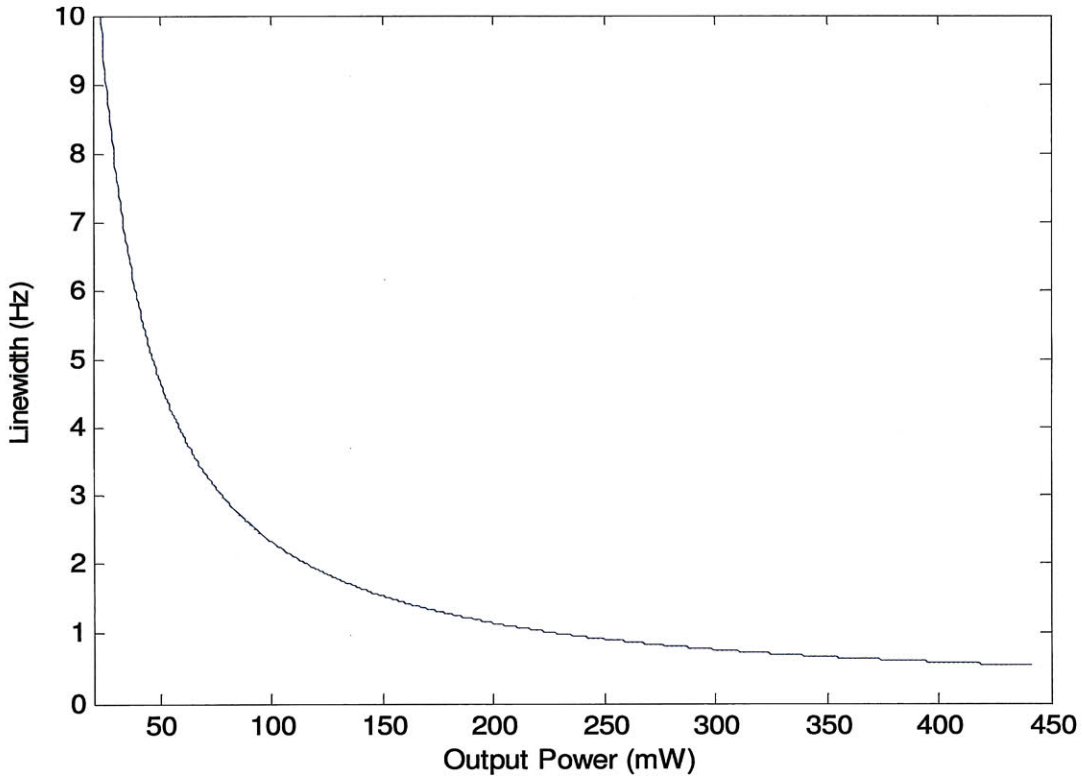

Figure 3-30: Schawlow-Townes Linewidth as a function of output power for 20 % FBG SCOWECL.

The plotted linewidth is seen to decrease with increasing output power. At 375 mW (4 A bias), the linewidth is seen to be less than 1 Hz! However, the previous measurements of the SCOWECL linewidth have all yielded Lorentzian linewidths on the order of kHz. This large discrepancy may be due to movements of the linewidth spectrum during the averaging of the lineshape or to the oversimplified approximations used in our Schawlow-Townes theoretical model. The reduction of the SCOWECL Lorentzian linewidth from 7.42 kHz to 2.17 kHz after packaging suggests that movement during lineshape averaging may at least partially contribute to the large errors seen between theory and experiment.

3.6 Summary

This chapter presented measurement results of slab-coupled optical waveguide external cavity lasers operating at wavelengths of 1550 nm and current biases ranging up to 5 A. The double-pass SCOWA, lensed fiber, fiber Bragg grating, and isolator components used in the SCOWECL design were also measured, and their characterization results were discussed in Section 3.2. Comparisons were performed between external cavity lasers constructed with 10 % and 20 % reflectivity FBGs in order to determine the effect of grating reflectivity on laser output power, RIN, and linewidth performance. The results indicated that the 20 % SCOWECL yielded the best characteristics with output powers at ~ 400 mW, RIN < -162 dB/Hz, and linewidth < 30 KHz. One of the tested 20 % SCOWECLs was packaged, and measurements conducted on the packaged SCOWECL yielded similar high performance levels. Modeling of the SCOWECL L-I and linewidth provided insight into the factors which may be currently limiting laser operation. It was found that the presence of an additional 53 % single pass loss may be responsible for the difference in output power between experimental observations and theoretical predictions.

Chapter 4

Conclusions and Future Work

4.1 Summary

Throughout this thesis, we have attempted to present a comprehensive overview of the measurements performed on amplifiers and external-cavity lasers employing the novel slab-coupled optical waveguide gain medium. These devices exploit the low confinement and low optical loss properties intrinsic to the SCOW design in order to simultaneously achieve high output powers and low intensity noise.

Slab-coupled optical waveguide amplifiers were characterized in terms of their output power, gain, and noise properties across the telecommunications 1550 nm wavelength range for currents ranging between 0.25 A and 5 A. The theory and calibration for the techniques used in these measurements were presented in great detail. From the SCOWA noise figure results, the population inversion factor of the gain medium can be extracted as a function of wavelength and current bias. These determined n_{sp} values were compared with theoretical predictions of the population inversion factor calculated using measured I-V results.

Slab-coupled optical waveguide external-cavity lasers were constructed by interfacing a double-pass SCOWA with a lensed-fiber-coupled fiber Bragg grating. An isolator was used at the output to prevent back reflection effects from disturbing laser operation. The measurements performed on each of the SCOWECL components were described in detail. Tests conducted on the assembled external cavity laser resulted in excellent power, RIN, and linewidth performance at 1550 nm for bias currents up to 5 A. These experimental findings were compared with theoretical predictions to gain insight into the operation of the SCOWECL.

In closing, we present a summary of the future work that can be explored based off the directions and goals of the current research discussed in this thesis.

4.2 Future Work

4.2.1 SCOWA Population Inversion Factor

The SCOWA population inversion factor can be determined across multiple wavelength and current operation regimes from accurate amplifier noise figure measurements. When the predicted n_{sp} values were compared with those derived from experimental I-V characteristics, the agreement was only found to be good up to 1 A bias current. This agreement was particularly bad on the short wavelength side with the noise figure predictions severely overestimating the value of n_{sp} compared to the I-V predictions. It was mentioned in Chapter 2 that these differences could be explained by increased effects of thermally induced carrier leakage, free carrier absorption, and intervalence band absorption. Measurement of these effects can yield additional insight into the operation of slab-coupled optical waveguide devices. As these devices are designed for high powers, a full characterization of these processes allows for the determination of important device limitations under high bias conditions.

4.2.2 Double-Pass SCOWA Gain Spectra

The measurement of the double-pass SCOWA gain spectra during the characterization of the SCOWECL yielded curves that exhibited interference effects at the high gain operation regime. This was not attributed to the SCOWA, but to the presence of two resonant cavities due to optical feedback of the amplified signal back into port 1 of the circulator. To correct for these effects, an optical isolator should be inserted into port 1 of the test configuration. The isolator allows for signal propagation of the tunable laser to port 2 but presents further attenuation for all signals coupled back to port 1 from port 2. This prevents any return signal from interacting with the laser cavity, and thus eliminates the occurrence of the observed Fabry-Perot interference fringes.

4.2.3 Double-Pass SCOWA Noise Figure

In Chapter 3, the L-I, gain spectra, internal loss, and injection efficiency measurements of the double-pass SCOWA were discussed. However, the noise figures of these amplifiers were never measured during the initial SCOWA characterization tests. Noise figure results of the double-pass devices can serve as useful comparisons to the noise figures of previously measured single-pass amplifiers for analyzing the effects of multiple reflections on SOA intensity noise and population inversion. Furthermore, measured results of SCOWA noise figures can even be used for estimating overall RIN performance when the amplifiers are used as the active component of external cavity lasers. However, the measurement setup for the noise figure characterization requires a circulator for optical signal routing around the double-pass configuration. The losses for all the circulator ports must be determined accurately in order to obtain reasonable results. Furthermore, isolators need to be used to prevent feedback effects into the laser, and the losses of the isolators must also be precisely calibrated out of the measurement. These complications make measuring the noise figure slightly more challenging for double-pass amplifier configurations.

4.2.4 SCOWECL Intra-Cavity Loss

An intra-cavity loss of 2.8 dB (53 %) was predicted in the 20 % grating SCOWECL case based on matching simulation data with experimental results of the laser L-I characteristics. It was hypothesized that this loss may be due to a polarization rotation of the optical field within the SCOWECL cavity. After many round trips, all the power in the TM component of the signal is effectively lost as only the TE signal is amplified by the SCOWA. To verify this, a variable amount of stress needs to be applied to the passive cavity in order to correct for any polarization rotation effects that may occur on a single pass. The stress itself creates a birefringence that can be used to rotate the net field arriving at the SCOWA input into a TE state. If by tuning the stress a noticeable change in output power occurs, it can be concluded that polarization effects are significant in the SCOWECL design. A passive cavity employing polarization maintaining (PM) fiber may be one possible solution for maintaining a purely TE intra-cavity signal.

4.2.5 SCOWLs with Monolithic Gratings

One possible future direction to explore with the SCOWA gain medium is the integration of grating-based structures within the SCOW laser design. This allows for the realization of distributed feedback (DFB) and distributed Bragg reflector (DBR) lasers with the potential benefits of high output power and low relative intensity noise. Proper design of the lasing wavelength relative to the gain peak can also allow for single mode operation at narrow linewidths to be achieved. Pulsed high power DFB/DBR lasers find application in free space communication systems where high signal levels are required to counteract attenuation resulting from atmospheric absorption.

Possible design challenges can be foreseen with regards to the integration of the grating within the SCOW structure. Corrugations etched along the active material in DFB designs may cause excessive pulling of the mode towards the p-junction. This counteracts the advantages of employing the SCOW gain medium, since the mode pulling effect leads to an increase in the optical confinement and a larger intervalence band absorption loss in the p-cladding region. In DBR structures, other problems arise since a large grating length may be needed to ensure single mode stability in the long resonance cavity. This may introduce unwanted signal absorption in the passive cavity, thereby reducing the total output power. DFB and DBR SCOWLs are expected to enable larger system integration by introducing wavelength selective grating elements on chip with the active components.

4.2.6 Polarization Insensitive SCOWAs

One of the primary reasons why SCOWAs cannot be used as in-line amplifiers is because they are intrinsically polarization sensitive. The fibers used in modern optical communication systems are non-polarization maintaining so that the signal polarization is unknown at any point along the fiber. A polarization independent implementation would allow compatibility with in-line signal amplification providing the advantages of high saturation output power, low noise figure, high coupling efficiency, and wide gain-bandwidth. All four attributes are particularly favorable for

use in modern high performance WDM systems. Wide gain-bandwidth specifically is one advantage semiconductor based amplifiers have over their fiber based counterparts.

A polarization insensitive SCOWA design requires the removal of the polarization dependence from both the active and the waveguide sections of the device. The TE and TM mode amplification can be balanced by introducing tensile strain within the quantum wells of the active layer. The waveguide polarization selectivity, however, is much more difficult to remove as any changes in the waveguide design may alter the mode supported by the guide. Because the TE confinement factor is in general different from its TM counterpart, changes to the device structure may ultimately be required. It may be challenging to balance the TE and TM modes while maintaining a low confinement waveguide design.

Appendix A

Erbium Doped Fiber External Cavity Laser

Before converging on our final SCOWECL design, we first experimented with a hybrid Erbium-doped fiber external cavity laser design. This laser structure utilizes a section of Erbium-doped fiber within the passive cavity and uses a SCOWA gain medium as the active cavity. In this implementation, the Erbium-doped fiber passive section is spliced to the fiber Bragg grating, and the entire passive cavity is butt-coupled to the SCOWA device. The schematic for this SCOWECL design is illustrated in Fig. A-1.

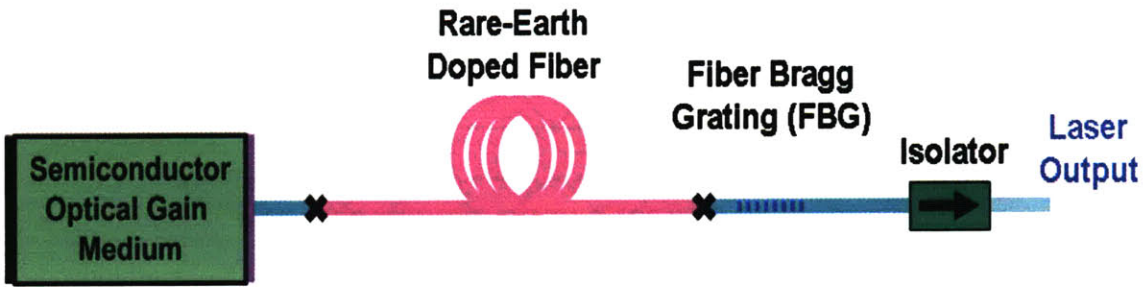

Figure A-1: Schematic of Erbium-doped fiber SCOWECL design.

In this section, we will explain the operational principles of the Erbium-doped SCOWECL concept. We will also describe the measurement results of absorption tests performed on the Erbium-doped fiber along with L-I results of the assembled laser. The laser was tested on a bench-top environment and was stabilized with a 16 °C thermoelectric cooler (TEC). The results gathered from these tests will show the problems associated with the hybrid Er-doped fiber FBG SCOWECL implementation. This section concludes with a discussion of the possible explanations for the poor performance demonstrated from this earlier SCOWECL design.

A.1 Erbium Doped Fiber External Cavity Laser Operation

The operation of the SCOWECL is different when the Erbium-doped fiber passive section is inserted within the laser cavity. Normally, the Er-doped fiber is excited by a pump laser to provide optical gain. In the hybrid SCOWECL, the Er-doped fiber is not pumped so it serves as a saturable absorber instead of as an amplifier. The absorption of the Erbium fiber is high for low optical intensities but decreases significantly under high intensity operation. This saturable absorber effect is interesting in a laser cavity because the forward and backward propagating fields create standing waves in the resonator. The standing waves cause periodic variations of the optical intensity spatially within the laser. The spatially varying intensity produces a spatially varying absorption profile that is exactly the inverse of the intensity distribution. Finally, because of the Kramers-Krönig relations, the spatial hole burning in absorption induces a spatial variation in the refractive index profile of the Erbium fiber. These processes are pictorially illustrated in Fig. A-2.

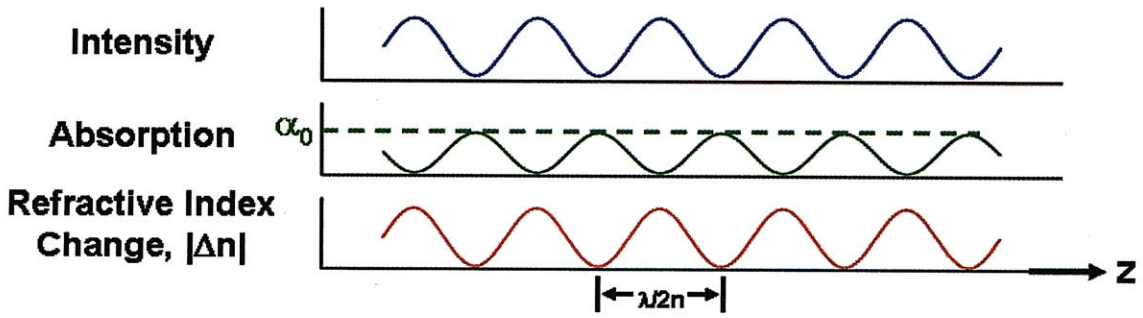

Figure A-2: Illustration of the intensity, absorption, and refractive index profiles created by the saturable absorber effect in the Erbium-doped fiber. λ is the lasing wavelength, and n is the fiber refractive index.

From Fig. A-2, we see that the saturable absorber effect has passively introduced a periodic refractive index pattern directly into the Erbium fiber. This refractive index structure creates a dynamical grating structure in series with the already present fiber Bragg grating [59-61]. The Bragg reflection wavelength (λ_B) of the dynamical grating is given by

$$\lambda_B = 2n\Lambda \tag{A.1}$$

and is automatically tuned to the cavity resonance wavelength. In Eq. (A.1), n is the refractive index of the grating medium, and Λ is the spatial period of the grating. The grating period will always be $\lambda/2n$ as determined solely from the standing wave created by the resonant optical field. Thus, a cascade of a self-aligned dynamical grating with a fiber Bragg grating is formed in the passive cavity. The dynamical grating enhances the wavelength selectivity of the FBG resulting in a narrowing of the reflectivity spectrum bandwidth.

The use of Erbium-doped fiber in the passive cavity offers the advantage of potentially improved single mode operation in lasers. However, there are a few drawbacks with this approach. The length of the added Erbium fiber, for example, extends the length of the passive cavity reducing the free spectral range between modes. Furthermore, the Erbium-doped fiber adds loss to the cavity resulting in an increase of the laser threshold current. This increase in threshold can quickly become intolerable for longer Erbium fiber lengths. Once the threshold is reached, the losses reduce significantly due to the saturation of the Erbium fiber. This creates a hysteresis effect in the L-I characteristics near the lasing threshold. Finally, even though the losses of the Erbium-doped fiber are greatly reduced once the laser reaches threshold, they never actually become zero. These losses can reduce the total power achievable from the laser output.

A.2 Erbium Doped Fiber SCOWECL Test Results

The losses of the Erbium fiber were characterized by sending the output of a tunable CW laser into the fiber and measuring the resulting attenuated output with a power meter. The Erbium fiber was spliced to connectors to facilitate optical coupling. Care must be taken in order to separate the effects of splice losses resulting from the mode mismatch between the Erbium and SMF fibers from the intrinsic losses of the Erbium fiber. In order to separate these effects, a series of cutback loss measurements on the fiber were performed. The slope of the loss measurements yielded the loss per unit length of the Erbium fiber. The intercept at zero length yielded the splice loss to within the uncertainty of the connector losses. The results of the measurements are shown in Fig. A-3.

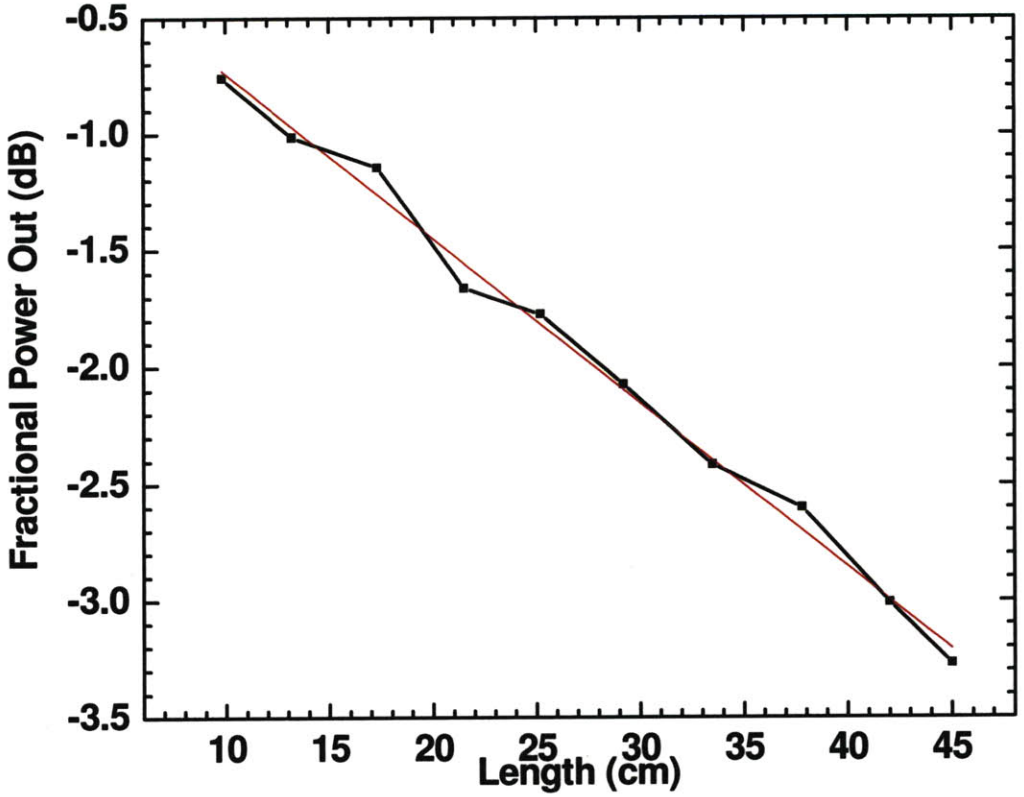

Figure A-3: Loss measurements of Erbium-doped fiber at 1550 nm as a function of length. The best fit line to the data results in a slope of 7.021 dB/m and a zero length intercept of 0.045 dB.

The slope of the loss measurements indicates an Erbium fiber loss per unit length of 7.021 dB/m. This agrees well with the manufacturer fiber loss specification of 6-8 dB/m. The splice loss was measured via the zero length intercept point to be 0.045 dB. The low splice loss we obtained gives us confidence that the splice between the Erbium-doped fiber and the FBG within the passive cavity will not significantly degrade laser performance.

An erbium-doped fiber external cavity laser was assembled and tested based on the configuration shown in Fig. A-1. The FBG used had a center wavelength of 1550 nm, a bandwidth of ~ 20 pm, and a reflectivity of 20 %. The passive and active cavities were interfaced through butt-coupling of an angle-cleaved erbium fiber to the SCOWA device. Previously reported results of hybrid semiconductor/rare-earth external cavity lasers have demonstrated single mode operation with fiber lengths in excess of 60 cm [60, 61]. Some lasers have even employed rare-earth doped fibers up to ~3 m in length [59]. Our SCOWECL design was tested

with 46 cm of erbium-doped fiber for an initial assessment of the dynamic grating behavior. The SCOWECL L-I and single mode behavior were measured in order to characterize the operation of the laser. The L-I measurement results for forward and backward current sweeps are shown in Fig. A-4.

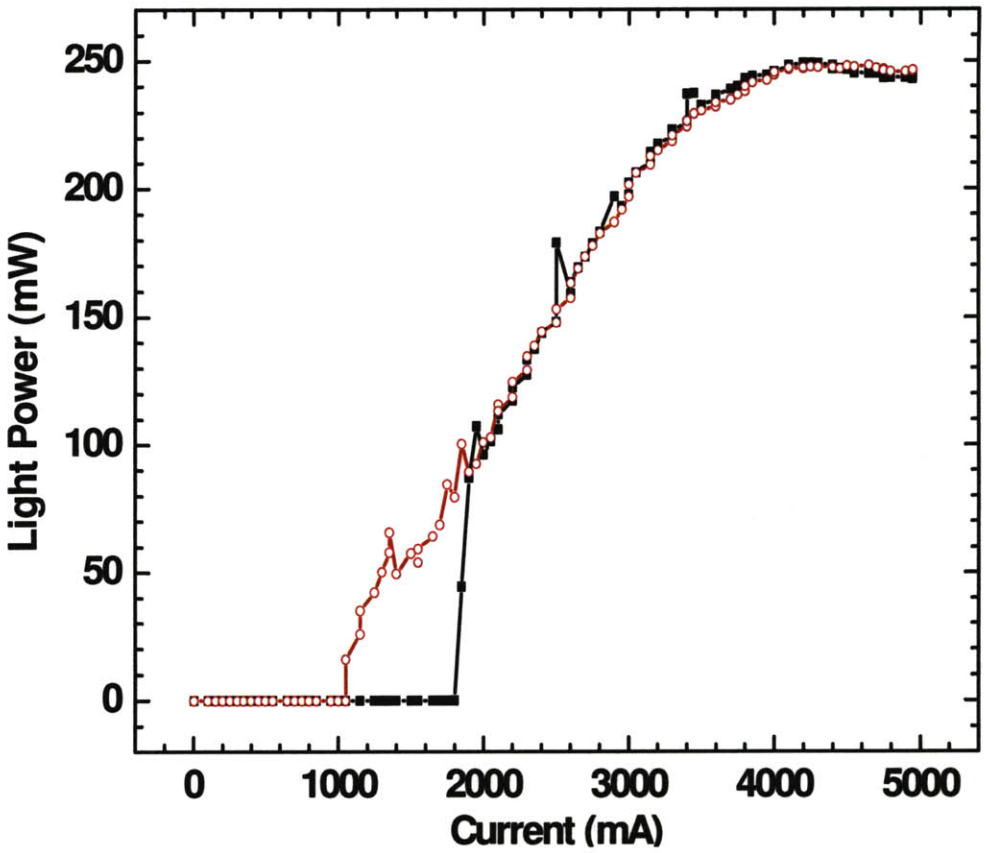

Figure A-4: L-I characteristics of erbium-doped fiber external cavity laser measured during a forward current sweep (solid squares) and backward current sweep (open circles). The TEC temperature was maintained at 16 °C.

The L-I characteristics exhibit a hysteresis effect due to the saturable absorption properties of the erbium doped fiber. The threshold current in the forward direction is ~1.8 A but decreases to ~1 A in the reverse direction. The slope efficiency, as extracted from the linear region of the L-I curve, is determined to be 10.4 %. From Fig. A-4, the SCOWECL is seen to reach a peak power of ~250 mW at ~4.2 A. However, the laser output power begins decreasing with further increase in bias past this point. The roll-off of the laser power at the higher currents is attributed to

thermal effects. Thermal lensing, in particular, can lead to significant decreases in coupling efficiency between the SCOWA and angled-cleaved fiber mode.

A Fabry-Perot interferometer measurement was performed in order to determine whether or not the SCOWECL operated on a single longitudinal mode. The measurement showed the presence of multiple side modes indicating that the Er-doped fiber dynamic grating was insufficient to narrow the cavity bandwidth.

A.3 Erbium Doped Fiber SCOWECL Performance Analysis

In our current SCOWECL design, the Erbium doped fiber is directly butt-coupled to the SCOWA device. Because of mode mismatch between the SCOWA and fiber mode, this design is not optimal. In our future designs, we use lensed fibers that have spot sizes which match the field diameter of the SCOWA mode. The lensed fibers are fusion spliced onto the fiber Bragg gratings to ensure low losses. The use of matched lensed fibers is expected to directly increase the coupling efficiency as a result of the improvement in mode field overlap.

The multimode operation of the SCOWECL indicates that the dynamic grating was not enough to compensate for the decreased FSR of the cavity longitudinal modes. This is unexpected based on previously demonstrated results of single mode hybrid semiconductor/rare-earth external cavity lasers [59-61]. One important distinction between the SCOWECL design and that of other dynamic grating lasers is the output fiber Bragg grating reflectivity. Typical hybrid external cavity lasers reported in literature have reflectivities in excess of 80%. As a result, the forward and backward propagating waves have nearly the same amplitude spatially along the cavity. The interference of the waves creates a standing wave that exhibits a near full intensity modulation depth. Regions with high intensity burn spatial holes in the doped fiber absorption, and regions with low intensity operate normally with high loss. In the hybrid SCOWECL, however, the FBG reflectivity was reduced to 20%. The reduction in output coupler reflectivity increases the total power output from the laser. However, the forward and backward intra-cavity waves are no longer closely matched in amplitude, and the modulation depth of the generated standing wave becomes weak. In this case, the absorption profile along the entire length of the Er-doped fiber is saturated with only a slight variation in absorption between regions of high and low intensity. As a result, the refractive index modulation is weak, and the

established dynamic grating becomes weak. Thus, the 46 cm length of Erbium-doped fiber behaves similar to bare fiber in the SCOWECL cavity only reducing the free spectral range of the longitudinal modes. In our next generation SCOWECL implementation, we remove the Erbium fiber altogether from the laser cavity and rely solely on the FBG for establishing single mode operation.

References

[1] M. A. Mahdi, F. R. M. Adikan, P. Poopalan, S. Selvakennedy, and H. Ahmad, "High-gain bidirectional Er3+-doped fiber amplifier for conventional- and long-wavelength bands," *Photonics Technology Letters, IEEE,* vol. 12, pp. 1468-1470, 2000.

[2] A. Galvanauskas, M. E. Fermann, and D. Harter, "High-power amplification of femtosecond optical pulses in a diode-pumped fiber system," *Opt. Lett.,* vol. 19, pp. 1201-1203, 1994.

[3] C. Simonneau, P. Bousselet, G. Melin, L. Provost, and C. Moreau, "High-power air-clad photonic crystal fiber cladding-pumped EDFA for WDM applications in the C-band," *European Conference on Optical Communication,* 2003.

[4] A. Sano and Y. Miyamoto, "Technologies for Ultrahigh Bit-Rate WDM Transmission," in *Lasers and Electro-Optics Society, 2007. LEOS 2007. The 20th Annual Meeting of the IEEE*, 2007, pp. 290-291.

[5] A. Tomoyuki, E. Mitsuru, S. Mitsuru, S. Hisao, K. Kenichi, K. Akito, E. Hiroji, M. Ken, I. Hajime, and A. Yasuhiko, "An ultrawide-band (120 nm) semiconductor optical amplifier having an extremely-high penalty-free output power of 23 dBm realized with quantum-dot active layers," in *Optical Fiber Communication Conference*, 2004, p. PD12.

[6] T. Suemune and Y. Takahashi, "SOA-fiber ring laser and its application to electric field sensing in frequency domain," *Optics and Lasers in Engineering,* vol. 45, pp. 789-794, 2007.

[7] T. L. Koch and U. Koren, "Semiconductor photonic integrated circuits," *Quantum Electronics, IEEE Journal of,* vol. 27, pp. 641-653, 1991.

[8] J. H. Marsh, "III-V Photonic Integration Outside Telecommunications - Does InP Have A Role?," in *Indium Phosphide and Related Materials Conference Proceedings, 2006 International Conference on*, 2006, pp. 10-13.

[9] S. U. Alam, P. W. Turner, A. B. Grudinin, J. Nilsson, and J. A. Alvarez-Chavez, "High-power cladding pumped erbium-ytterbium co-doped fiber laser," in *Optical Fiber Communication Conference and Exhibit, 2001. OFC 2001*, 2001, pp. TuI4-1-TuI4-3 vol.2-TuI4-1-TuI4-3 vol.2.

[10] P. W. Juodawlkis, J. J. Plant, J. P. Donnelly, A. Motamedi, and E. P. Ippen, "Continuous-wave two-photon absorption in a Watt-class semiconductor optical amplifier," *Opt. Express,* vol. 16, pp. 12387-12396, 2008.

[11] C. Henry, "Theory of the linewidth of semiconductor lasers," *Quantum Electronics, IEEE Journal of,* vol. 18, pp. 259-264, 1982.

[12] P. W. Juodawlkis, J. J. Plant, R. K. Huang, L. J. Missaggia, and J. P. Donnelly, "High-power 1.5-μm InGaAsP-InP slab-coupled optical waveguide amplifier," *Photonics Technology Letters, IEEE,* vol. 17, pp. 279-281, 2005.

[13] T. G. Juliet, J. P. Jason, C. Bien, K. H. Robin, H. Christopher, M. Leo, P. D. Joseph, W. J. Paul, and J. R. Daniel, "High Power Monolithic Passively Mode-Locked Slab-Coupled Optical Waveguide Lasers," in *Conference on Lasers and Electro-Optics/Quantum Electronics and Laser Science Conference and Photonic Applications Systems Technologies*, 2006, p. CThH5.

[14] P. W. Juodawlkis, J. J. Plant, L. J. Missaggia, K. E. Jensen, and F. J. O'Donnell, "Advances in 1.5-μm InGaAsP/InP Slab-Coupled Optical Waveguide Amplifiers (SCOWAs)," in *Lasers and Electro-Optics Society, 2007. LEOS 2007. The 20th Annual Meeting of the IEEE*, 2007, pp. 309-310.

[15] J. J. Plant, J. T. Gopinath, B. Chann, D. J. Ripin, R. K. Huang, and P. W. Juodawlkis, "250 mW, 1.5μm monolithic passively mode-locked slab-coupled optical waveguide laser," *Opt. Lett.*, vol. 31, pp. 223-225, 2006.

[16] E. A. J. Marcatilli, "Slab-coupled waveguides," *BELL SYSTEM TECH JOUR*, vol. 53, pp. 645-672, 1974.

[17] J. N. Walpole, J. P. Donnelly, P. J. Taylor, L. J. Missaggia, C. T. Harris, R. J. Bailey, A. Napoleone, S. H. Groves, S. R. Chinn, R. Huang, and J. Plant, "Slab-coupled 1.3-μm semiconductor laser with single-spatial large-diameter mode," *Photonics Technology Letters, IEEE*, vol. 14, pp. 756-758, 2002.

[18] Y. Xiong, S. Murphy, J. L. Carlsten, and K. Repasky, "Design and characteristics of a tapered amplifier diode system by seeding with continuous-wave and mode-locked external cavity diode laser," *Optical Engineering*, vol. 45, pp. 124205-5, 2006.

[19] S. H. Oh, J.-M. Lee, K. S. Kim, H. Ko, C.-W. Lee, S. Park, and M.-H. Park, "Fabrication of Tunable Sampled Grating DBR Laser Integrated Monolithically with Optical Semiconductor Amplifier Using Planar Buried Heterostructure," *Japanese Journal of Applied Physics*, vol. 43, p. L1343.

[20] I. Brener, B. Mikkelsen, G. Raybon, R. Harel, K. Parameswaran, J. R. Kurz, and M. M. Fejer, "160 Gbit/s wavelength shifting and phase conjugation using periodically poled LiNbO3 waveguide parametric converter," *Electronics Letters*, vol. 36, pp. 1788-1790, 2000.

[21] D. X. Zhu, S. Dubovitsky, W. H. Steier, K. Uppal, D. Tishinin, J. Burger, and P. D. Dapkus, "Noncollinear four-wave mixing in a broad area semiconductor optical amplifier," *Applied Physics Letters*, vol. 70, pp. 2082-2084, 1997.

[22] L. F. Tiemeijer, P. J. A. Thijs, T. van Dongen, J. J. M. Binsma, and E. J. Jansen, "Polarization resolved, complete characterization of 1310 nm fiber pigtailed multiple-quantum-well optical amplifiers," *Lightwave Technology, Journal of*, vol. 14, pp. 1524-1533, 1996.

[23] K. K. Qureshi, H. Y. Tarn, C. Lu, and P. K. A. Wai, "Gain Control of Semiconductor Optical Amplifier Using a Bandpass Filter in a Feedback Loop," *Photonics Technology Letters, IEEE*, vol. 19, pp. 1401-1403, 2007.

[24] C. Holtmann, P. A. Besse, T. Brenner, and H. Melchior, "Polarization independent bulk active region semiconductor optical amplifiers for 1.3 μm wavelengths," *Photonics Technology Letters, IEEE*, vol. 8, pp. 343-345, 1996.

[25] M. J. Connelly, *Semiconductor Optical Amplifiers*, 1 ed. New York: Springer-Verlag New York, 2002.

[26] K. Morito, S. Tanaka, S. Tomabechi, and A. Kuramata, "A broad-band MQW semiconductor optical amplifier with high saturation output power and low noise figure," *Photonics Technology Letters, IEEE*, vol. 17, pp. 974-976, 2005.

[27] W. Loh, J. J. Plant, F. J. O'Donnell, and P. W. Juodawlkis, "Noise figure of a packaged, high-power slab-coupled optical waveguide amplifier (SCOWA)," in *IEEE Lasers and Electro-Optics Society, 2008. LEOS 2008. 21st Annual Meeting of the*, 2008, pp. 852-853.

[28] S. Dubovitsky, A. Mathur, W. H. Steier, and P. D. Dapkus, "Gain saturation properties of a polarization insensitive semiconductor amplifier implemented with tensile and compressive strain quantum wells," *Photonics Technology Letters, IEEE,* vol. 6, pp. 176-178, 1994.

[29] D. M. Baney, P. Gallion, and R. S. Tucker, "Theory and Measurement Techniques for the Noise Figure of Optical Amplifiers," *Optical Fiber Technology,* vol. 6, pp. 122-154, 2000.

[30] T. Briant, P. Grangier, R. Tualle-Brouri, A. Bellemain, R. Brenot, and B. Thedrez, "Accurate determination of the noise figure of polarization-dependent optical amplifiers: theory and experiment," *Lightwave Technology, Journal of,* vol. 24, pp. 1499-1503, 2006.

[31] C. Henry, "Theory of spontaneous emission noise in open resonators and its application to lasers and optical amplifiers," *Lightwave Technology, Journal of,* vol. 4, pp. 288-297, 1986.

[32] E. Staffan Bjorlin and J. E. Bowers, "Noise figure of vertical-cavity semiconductor optical amplifiers," *Quantum Electronics, IEEE Journal of,* vol. 38, pp. 61-66, 2002.

[33] D. Tauber, R. Nagar, A. Livne, G. Eisenstein, U. Koren, and G. Raybon, "A low-noise-figure 1.5 μm multiple-quantum-well optical amplifier," *Photonics Technology Letters, IEEE,* vol. 4, pp. 238-240, 1992.

[34] D. Derickson, *Fiber Optic Test and Measurement.* Upper Saddle River: Prentice Hall PTR, 1998.

[35] C. C. Harb, T. C. Ralph, E. H. Huntington, D. E. McClelland, H.-A. Bachor, and I. Freitag, "Intensity-noise dependence of Nd:YAG lasers on their diode-laser pump source," *J. Opt. Soc. Am. B,* vol. 14, pp. 2936-2945, 1997.

[36] G. A. Kerr, N. A. Robertson, J. Hough, and C. N. Man, "The fast frequency stabilisation of an argon laser to an optical resonator using an extra-cavity electro-optic modulator," *Applied Physics B: Lasers and Optics,* vol. 37, pp. 11-16, 1985.

[37] L. A. Coldren and S. W. Corzine, *Diode Lasers and Photonic Integrated Circuits.* New York: John Wiley & Sons, Inc., 1995.

[38] J. J. Plant and P. W. Juodawlkis, "High power 1.5-um InGaAsP/InP Colliding-Pulse Mode-Locked Slab-Coupled Optical Waveguide Laser," in *Lasers and Electro-Optics Society, 2006. LEOS 2006. 19th Annual Meeting of the IEEE,* 2006, pp. 794-795.

[39] P. W. Juodawlkis, J. J. Plant, W. Loh, L. J. Missaggia, K. E. Jensen, and F. J. O'Donnell, "Packaged 1.5-μm Quantum-Well SOA With 0.8-W Output Power and 5.5-dB Noise Figure," *Photonics Technology Letters, IEEE,* vol. 21, pp. 1208-1210, 2009.

[40] B. Arnaudov, D. S. Domanevskii, S. Evtimova, C. Ivanov, and R. Kakanakov, "Band-filling effect on the light emission spectra of InGaN/GaN quantum wells with highly doped barriers," *Microelectronics Journal,* vol. 40, pp. 346-348, 2009.

[41] R. O. Miles, M. A. Dupertuis, F. K. Reinhart, and P. M. Brosson, "Gain measurements in InGaAs/InGaAsP multiquantum-well broad-area lasers," *Optoelectronics, IEE Proceedings J,* vol. 139, pp. 33-38, 1992.

[42] J. J. Plant, A. K. Goyal, D. C. Oakley, D. C. Chapman, A. Napoleone, and P. W. Juodawlkis, "Improving the Efficiency of High-Power Semiconductor Optical Amplifiers," in *Conference on Lasers and Electro-Optics/Quantum Electronics and Laser Science Conference and Photonic Applications Systems Technologies,* 2008, p. CMN7.

[43] Alphion, "QLight C-Amp Product Brief."

[44] J. P. Jason, K. G. Anish, C. O. Douglas, C. C. David, N. Antonio, and W. J. Paul, "Improving the Efficiency of High-Power Semiconductor Optical Amplifiers," in *Conference on Lasers and Electro-Optics/Quantum Electronics and Laser Science Conference and Photonic Applications Systems Technologies*, 2008, p. CMN7.

[45] E. Jaunart, B. Heens, and J.-C. Froidure, "Optical and electrical methods comparison for accurate measurement of erbium-doped fiber amplifiers (EDFA) gain and noise figure," in *Fiber Optic Network Components*, Amsterdam, Netherlands, 1995, pp. 245-256.

[46] M. Movassaghi, M. K. Jackson, V. M. Smith, and W. J. Hallam, "Noise Figure of Erbium-Doped Fiber Amplifiers in Saturated Operation," *J. Lightwave Technol.,* vol. 16, p. 812, 1998.

[47] N. E. Jolley, F. Davis, and J. Mun, "A Bragg grating optically gain-clamped EDFA with adjustable gain, low noise figure and low multipath interference," in *Optical Fiber Communication Conference and Exhibit, 1998. OFC '98., Technical Digest*, 1998, pp. 139-140.

[48] G. Keiser, *Optical Communications Essentials*: McGraw-Hill Professional, 2003.

[49] M. Movassaghi, "Characterization and Modeling of Erbium-Doped Fiber Amplifiers and Impact of Fiber Dispersion on Semiconductor Laser Noise," in *Department of Electrical Engineering and Computer Science*. vol. Doctor of Philosophy Vancouver: University of British Columbia, 1999, p. 124.

[50] G. E. Obarski and J. D. Splett, "Transfer standard for the spectral density of relative intensity noise of optical fiber sources near 1550 nm," *J. Opt. Soc. Am. B,* vol. 18, pp. 750-761, 2001.

[51] F. Pommereau, R. Brenot, J. Landreau, L. L. Gouezigou, O. L. Gouezigou, O. L. Lelarge, F. Martin, F. Poingt, B. Rousseau, G. H. Duan, and B. Thedrez, "Realisation of semiconductor optical amplifiers with homogeneous carrier density and low noise factor," in *Indium Phosphide and Related Materials, 2005. International Conference on*, 2005, pp. 102-105.

[52] C. H. Cox, *Analog Optical links*. Cambridge: Cambridge University Press, 2004.

[53] L. Yifei and P. Herczfeld, "Coherent PM Optical Link Employing ACP-PPLL," *Lightwave Technology, Journal of,* vol. 27, pp. 1086-1094, 2009.

[54] H. D. Summers, P. Dowd, I. H. White, and M. R. T. Tan, "Calculation of differential gain and linewidth enhancement factor in 980-nm InGaAs vertical cavity surface-emitting lasers," *Photonics Technology Letters, IEEE,* vol. 7, pp. 736-738, 1995.

[55] D. C. Heo, I. K. Han, J. I. Lee, J. C. Jeong, and S. H. Cho, "Effects of the linewidth enhancement factor on filamentation in 1.55 μm broad-area laser diodes," *Semiconductor Science and Technology,* vol. 18, pp. 486-490, 2003.

[56] R. F. Kazarinov, C. H. Henry, and R. A. Logan, "Longitudinal mode self-stabilization in semiconductor lasers," *Journal of Applied Physics,* vol. 53, pp. 4631-4644, 1982.

[57] J. L. Gimlett and N. K. Cheung, "Effects of phase-to-intensity noise conversion by multiple reflections on gigabit-per-second DFB laser transmission systems," *Lightwave Technology, Journal of,* vol. 7, pp. 888-895, 1989.

[58] P. Gallion and G. Debarge, "Quantum phase noise and field correlation in single frequency semiconductor laser systems," *Quantum Electronics, IEEE Journal of,* vol. 20, pp. 343-349, 1984.

[59] W. H. Loh, R. I. Laming, M. N. Zervas, M. C. Farries, and U. Koren, "Single frequency erbium fiber external cavity semiconductor laser," *Applied Physics Letters,* vol. 66, pp. 3422-3424, 1995.

[60] F. Timofeev and R. Kashyap, "High-power, ultra-stable, single-frequency operation of a long, doped-fiber external-cavity, grating-semiconductor laser," *Opt. Express,* vol. 11, pp. 515-520, 2003.

[61] R. Liu, I. A. Kostko, K. Wu, and R. Kashyap, "Side mode suppression using a doped fiber in a long external-cavity semiconductor laser operating at 1490 nm," *Opt. Express,* vol. 14, pp. 9042-9050, 2006.